

© 2021 by Yu Yao. All rights reserved.

QUANTIFYING CLOUD CHEMICAL PROCESSES AND AEROSOL OPTICAL
PROPERTIES USING A PARTICLE-RESOLVED AEROSOL MODEL

BY

YU YAO

DISSERTATION

Submitted in partial fulfillment of the requirements
for the degree of Doctor of Philosophy in Atmospheric Sciences
with a concentration in Computational Science and Engineering
in the Graduate College of the
University of Illinois at Urbana-Champaign, 2021

Urbana, Illinois

Doctoral Committee:

Professor Nicole Riemer, Chair and Director of Research
Professor Sonia Lasher-Trapp
Associate Professor Matthew West
Dr. Matt Dawson

Abstract

Aerosol particles exert substantial radiative effects on the Earth's climate directly by scattering and absorbing incoming solar radiation, and indirectly by interacting with clouds. These climate effects depend on particle size distributions and chemical composition, and these properties evolve as particles are transported in the atmosphere. As an important aging process, cloud processing changes particle size and composition through cloud chemistry and in-cloud coagulation. These processes are highly affected by per-particle properties, by determining which particles can be activated and which reactions occur within each droplet. It is challenging for global or regional models with simplified aerosol representations to accurately capture these processes.

The aim of the first part of this thesis was to (1) quantify the changes of aerosol mixing state and microphysical properties after cloud processing (2) quantify the role of coagulation between the interstitial particles and cloud droplets for mixing state of the aerosol. By coupling an aqueous chemistry mechanism to the particle-resolved model PartMC-MOSAIC, the new model was able to track the evolution of compositions and sizes of individual aerosol particles in the cloud without averaging their composition within size bins or modes. Aqueous-phase chemistry processes caused aerosol populations to be more internally mixed, and cloud condensation nuclei concentrations increased substantially after cloud processing for supersaturation levels lower than the maximum cloud supersaturation. Coagulation within clouds had a negligible impact on aerosol mixing state.

The aim of the second part of the thesis was to systematically quantify the impact of aerosol mixing state on aerosol optical properties. To this end, I created a reference scenario library with aerosol populations of a wide range of mixing states using the particle-resolved model PartMC-MOSAIC. The impact of aerosol mixing state on optical properties was quantified by comparing the reference populations to populations with the same number and mass size distributions but with averaged aerosol composition in prescribed size bins. Particle absorption coefficients were universally overestimated after using internal mixture assumptions, with the overestimation reaching up to 70% for externally-mixed populations. In contrast, scattering coefficients were underestimated, with a maximum error of -32% . Overall, this led to an underestimation in single scattering albedo of up to -22% . The environmental relative humidity and associated aerosol water uptake only had a small impact on the magnitude of these errors.

To my family

Acknowledgments

I would like to express my sincere gratitude to my advisor, Prof. Nicole Riemer, for her patience and continuous support during my Ph.D journey. She has been encouraging and has allowed me the flexibility to finish the tasks at my own pace. I learned a lot from her insightful discussion about the research during our weekly individual meeting in the past five years. She is energetic about the research, i.e. the tiny aerosol particles, and I hope one day I could be as enthusiastic as her. I am also thankful to my doctoral committee members, Prof. Sonia Lasher-Trapp, Prof. Matthew West, and Dr. Matt Dawson for their instructions on cloud physics, numerical computing, and cloud chemistry.

I am lucky to join the department of atmospheric science family in UIUC. I met lots of friends and I will miss the spring picnic, fall picnic and Christmas party hold by DASSO. I would also like to thank my current and previous PartMC group members. Special thanks to Jeff Curtis for his coding helps and Joseph Ching for his thoughtful ideas.

I am also thankful to my friends for providing the friendship, especially my roommates Chuan-chieh Chang, Tsu-shun Lin, and Chun-yu Yao. I will miss the joyful times we spent together in different trips. I also thank Saturday Bookclub members for reading and sharing some wonderful books together. I want to express my special thanks to Shiya Liu, Beixi Jia, Shan Huang, and Qing Zhang for lots of interesting and meaningful discussions about social issues.

Lastly, I especially thank my mom, dad and brother. Thanks for their understanding and unconditional love, especially during the unusual past two years.

I acknowledge the funding from National Science Foundation under CAREER grant AGS-1254428.

Contents

Chapter 1 Introduction and motivation	1
1.1 Aerosol properties	2
1.2 Aerosol climate forcing	4
1.3 Aerosol mixing state	5
1.4 Aerosol mixing state evolution	8
1.5 Aerosol modeling approaches	10
1.6 Models for aqueous chemistry simulation	13
1.7 Research questions and thesis organization	14
Chapter 2 Particle-resolved modeling of aqueous-phase chemistry	16
2.1 Introduction	16
2.2 Model description and simulation setup	17
2.3 Sulfate mechanism verification	21
2.4 Contribution of different aqueous sulfate formation pathways	23
2.5 Contribution of TMI pathways to sulfate formation	28
2.6 Conclusion	29
Chapter 3 Evaluating the impacts of cloud processing on resuspended aerosol particles after cloud evaporation using a particle-resolved model	31
3.1 Introduction	31
3.2 Model description and metrics	33
3.3 Simulation results	39
3.4 Conclusions	60
Chapter 4 Quantifying the effects of mixing state on aerosol optical properties	63
4.1 Introduction	63
4.2 Model description, scenario libraries and metrics	66
4.3 Errors in aerosol absorptivity and scattering for dry particles	73
4.4 The effects of water uptake on aerosol optical properties	80
4.5 Errors in single scattering albedo and implications for directive radiative forcing	81
4.6 Conclusion and discussion	83
Chapter 5 Conclusions	85
5.1 Work summary	85
5.2 Contributions	85
5.3 Future work suggestions	87
Appendix A Appendix to Chapter 2	89
A.1 List of aqueous reactions coupled to PartMC-MOSAIC	89
Appendix B Appendix to Chapter 3	94
References	96

Chapter 1

Introduction and motivation

Aerosols are solid or liquid particles suspended in air. They recently received tremendous attention by the public because of the ongoing Covid-19 pandemic caused by the SARS-CoV-2 virus, which is airborne and transmitted by aerosols (Prather et al., 2020; Zhang et al., 2020; Miller et al., 2021; Greenhalgh et al., 2021). However, aerosol particles have been recognized as an important component of air pollutants long before the Covid-19 pandemic. The health effects of aerosol particles, especially those with diameters less than $2.5\text{ }\mu\text{m}$ ($\text{PM}_{2.5}$), have been investigated for several decades (Dockery et al., 1993; Bell et al., 2007; Fann et al., 2012). Around 141 000 premature deaths in North America due to cardiopulmonary and lung cancer are associated with $\text{PM}_{2.5}$ (Anenberg et al., 2010). According to a recent WHO report (WHO et al., 2018), ambient air pollution caused around 4.2 million premature deaths worldwide, including 300,000 children under the age of 5. The majority of these children died as a result of aerosol particle exposure, mainly in low- and middle-income nations.

Besides its crucial impacts on health, aerosol particles also impact weather and climate through interacting with solar radiation and clouds. Large uncertainties still exist regarding quantifying these impacts (Boucher et al., 2013; Seinfeld et al., 2016b; Fan et al., 2016; Bellouin et al., 2020). The interaction between aerosols and climate manifests itself in two ways. On the one hand, aerosol particles directly alter the Earth's radiative balance by scattering and absorbing incoming solar radiation, known as aerosol-radiation interactions (ari). On the other hand, aerosol indirectly affect climate by influencing cloud properties, such as droplets number concentration and cloud life, and this effect is known as aerosol-cloud interactions (aci). Unlike greenhouse gases, aerosols typically have a short lifetime of only several days, and their concentrations and properties vary strongly in space and time, causing the interactions to have the large uncertainties in our predictions of the future climate.

This dissertation focuses on two specific aspects within the large topic of aerosol climate effects. The first is to quantify the changes that aerosol particles experience as a result of aqueous phase chemistry within clouds. The second is to quantify the error in aerosol optical properties that is incurred by simplified aerosol representations, common in current chemical transport models. We approach both topics from a particle-resolved modeling perspective. This chapter provides background about aerosol properties, aerosol climate forcing, aerosol mixing state, mixing state evolution, model representation for aerosol and aqueous processes, and formulates the research questions of this

work.

1.1 Aerosol properties

Aerosol particles can be directly emitted from a variety of sources (primary aerosol), or formed in the atmosphere from gas precursors (secondary aerosol). The major components of particles are sulfate, nitrate, ammonium, carbonaceous species, sea salt and mineral dust. These species can originate from natural or anthropogenic sources, and the formation pathways also depend on the aerosol type. Sea salt particles are generated over ocean regions through wave breaking and bubble bursting. Dust is another primary particle type originating mainly from desert regions and can impact regions at great distances from the source regions through long-range transport (Van Der Does et al., 2018; Yu et al., 2021). The flux of sea salt and of mineral dust particles into the atmosphere strongly depends on wind speed (Monahan et al., 1986; Shao, 2001; Jaeglé et al., 2011).

Several inorganic aerosol species are secondary in nature, and formed through either nucleation or gas-to-particle partitioning. For example, sulfate can form through nucleation of sulfuric acid in the presence of water vapor (Sipilä et al., 2010), and it can also be produced through oxidation of SO_2 by OH in gas phase or H_2O_2 and O_3 in the aqueous phase (Shao et al., 2019b; Zheng et al., 2020). Nitrate is mainly formed through oxidation of NO_2 by OH at daytime and hydrolysis of N_2O_5 at night (Alexander et al., 2009a). Ammonium forms when ammonia partitions to the aerosol phase (Zhuang et al., 1999). Black carbon (BC) and primary organic aerosol (POA) are usually co-emitted from combustion of fossil fuel and biofuel (Bond et al., 2007). The formation of secondary organic aerosol (SOA) involves partitioning of semivolatile species, oligomerization and aqueous chemistry (Zhu et al., 2017; Lim et al., 2010; Griffin, 2013; McNeill, 2015b). Oligomerization is a process that combines monomers into macromolecular compounds, and the oligomerization of primary monomers and its decomposition products are proved to be an important pathway for SOA formation (Tolocka et al., 2004).

It is important to note that particles in the atmosphere are commonly mixture of different species (Laskin et al., 2019; O'Brien et al., 2015). As an example, Figure 1.1 shows transmission electron microscopy (TEM) images of particles collected in urban Shanghai in 2010. Many particles are mixture of at least two species (a, b, c), while others are mixture of more than three species (f, g, h, i).

In addition to exhibiting great diversity with respect to composition, aerosol particle diameters vary from small molecule clusters of several nanometers to large particles of several micrometers (McMurtry, 2003). It is common to represent the aerosol size distribution by three size ranges, called “modes”: The nuclei mode ($0.01\text{--}0.1 \mu\text{m}$), the accumulation mode ($0.1\text{--}2 \mu\text{m}$) and the coarse mode ($2\text{--}10 \mu\text{m}$). Nuclei-mode particles are commonly observed near combustion sources, especially the roadside atmosphere, and characterized by high number concentration, which

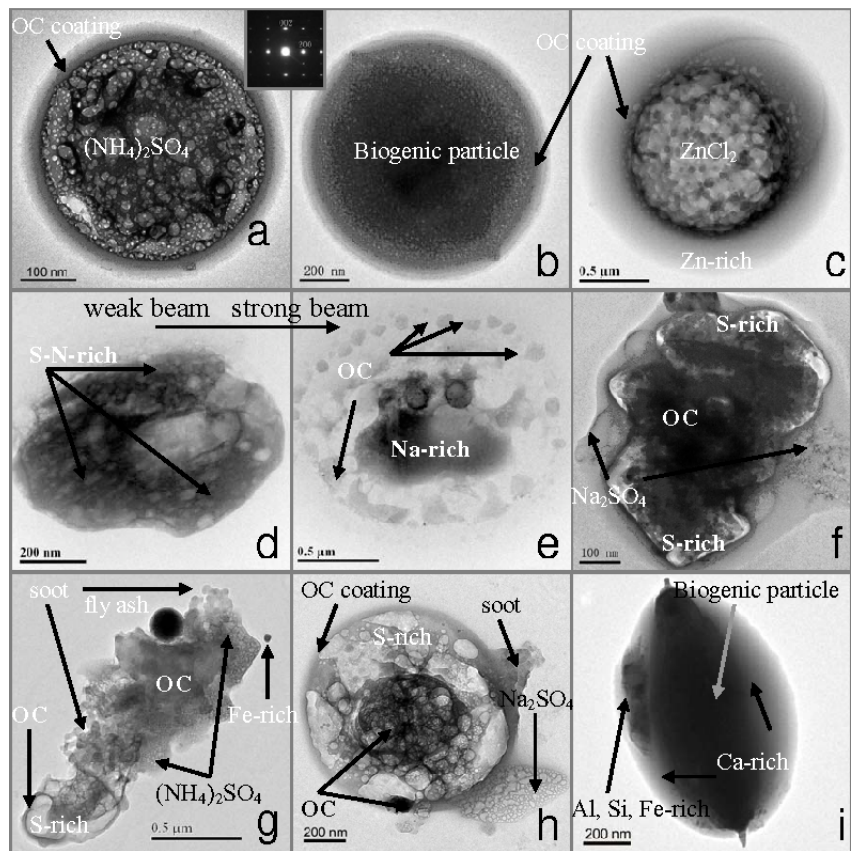


Figure 1.1: TEM images of carbonaceous particles collected from urban Shanghai, adapted from Fu et al. (2012).

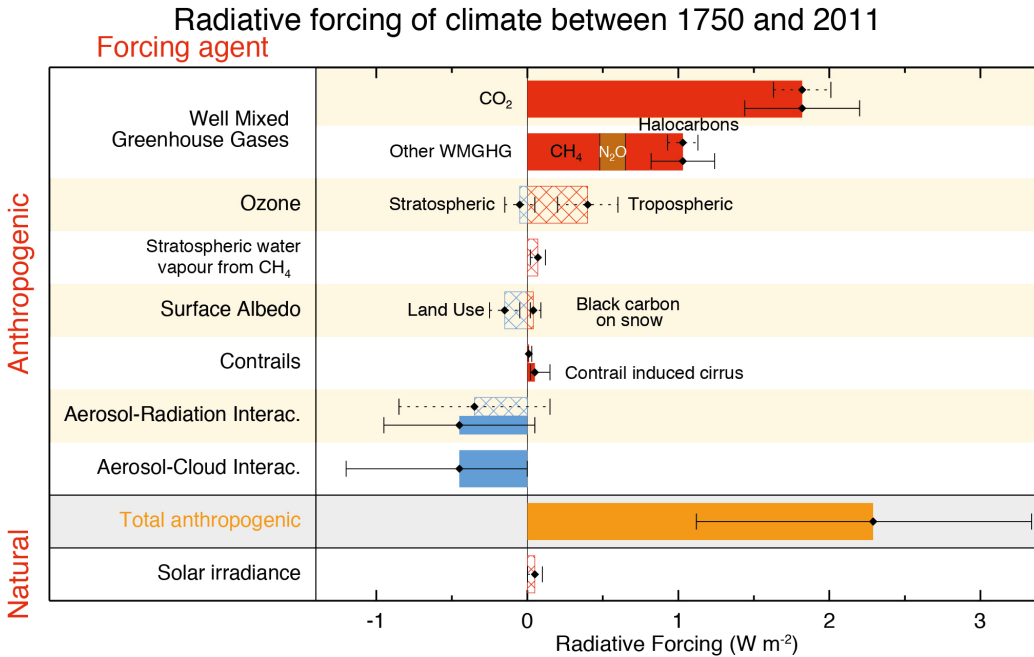


Figure 1.2: Radiative forcing estimation of different agents between 1750 and 2011, adapted from Myhre et al. (2013).

causes efficient coagulation and results in short lifetime of these particles (Fushimi et al., 2008). Accumulation-mode particles contain most of the secondary species, such as sulfate, nitrate and organics (Zhang et al., 2005), and they can be produced from the growth of nuclei-mode particles by coagulation and condensation. These particles stay longer in the air because the removal processes of coagulation and dry deposition are not efficient in this size range. The lifetime of these particles can be up to one week (Feichter and Leisner, 2009), with wet deposition being the most efficient removal process. As for coarse-mode particles, it is hard to grow such large particles directly from the accumulation mode (Friedlander et al., 1991; Lee and Wu, 2005). They mostly originate from natural sources and produced through mechanical processes. Rapid gravitational settling results in a short lifetime for these particles.

1.2 Aerosol climate forcing

Aerosol impact the radiation balance of Earth system through direct interactions with shortwave and longwave radiation. The globally averaged direct aerosol effective radiative forcing between 1750 and 2011 is estimated to be -0.45 W m^{-2} , as shown in Fig. 1.2. Estimation of radiative forcing relies on the properties of aerosol population, such as size and chemical components. The large variation of aerosols in different regions leads to spatial variation of this effect. For example, while the direct radiative forcing at the top of atmosphere over Africa is around -12 W m^{-2} , it can reach $+30 \text{ W m}^{-2}$ over the polluted Indo-Gangetic Plains (Subba et al., 2020).

By serving as cloud condensation nuclei, aerosol particles also indirectly affect climate through interactions with cloud, and the estimated effective radiative forcing from this interaction is -0.45 W m^{-2} , similar to the effective direct radiative forcing (Fig. 1.2). There are many processes involved in the interactions, which can be summarized by two main effects: the cloud albedo and the lifetime effects. However, large uncertainties still exist in quantifying the cloud lifetime effects, and they are not included in calculating aerosol-cloud interaction forcings in Fig. 1.2.

Cloud albedo effects, first proposed by Twomey (1977), describe the changes of cloud droplet number concentration and surface area as the number concentration of aerosol particles changes, which was supported by ambient observations. Kaufman et al. (2005), by analyzing satellite observations in four regions over Atlantic ocean where clouds are affected by four different types of aerosols, proved that polluted clouds contain more smaller droplets. In-situ field observations also confirm that more cloud condensation nuclei (CCN) generate more cloud droplets with smaller sizes in liquid clouds (Jia et al., 2019; Kleinman et al., 2012).

The cloud lifetime effect describes the mechanism that the increase of aerosol number concentration not only results in smaller cloud droplets but also inhibits the precipitation development. This effect is plausible if only the initiation of precipitation is considered. However, several observation and modeling studies suggested that it is hard to find clear evidence for this effect due to the complex microphysical and macrophysical buffer responses after altering the aerosol loading in the environment (Stevens and Feingold, 2009).

As we can see from Fig. 1.2, large differences still exist among different models in the magnitude of the aerosol-related radiative forcing. For the radiative forcing from aerosol radiation interaction, the estimated 5 to 95% confidence interval ranges from -0.95 to $+0.05 \text{ W m}^{-2}$, while the range is from -1.2 to 0.0 W m^{-2} for the radiative forcing due to aerosol-cloud interaction. The sources of the uncertainty lie in the fact that the processes involved cover a large range of scales, from particles as small as 10 nm to 1000 km stratocumulus clouds. Many processes are still not well-understood on a fundamental level, such as aerosol interaction with mixed-phase and ice clouds, and simple parameterization schemes are applied to describe these processes in the models. But even for the processes that are well-understood on a microscale level, it is challenging to incorporate all them in a large-scale model (Seinfeld et al., 2016b; Bellouin et al., 2020). By interacting with electromagnetic radiation, and acting as an nuclei for cloud formation, particles are fundamental for determining radiative forcing and an accurate description of aerosols can help reduce the model uncertainty or at least help quantify the uncertainty that is currently present.

1.3 Aerosol mixing state

The aerosol mixing state refers to the distribution of chemical species among a particle population and is a helpful framework to describe aerosols (Winkler, 1973b). We distinguish between two mixing state extremes: the fully

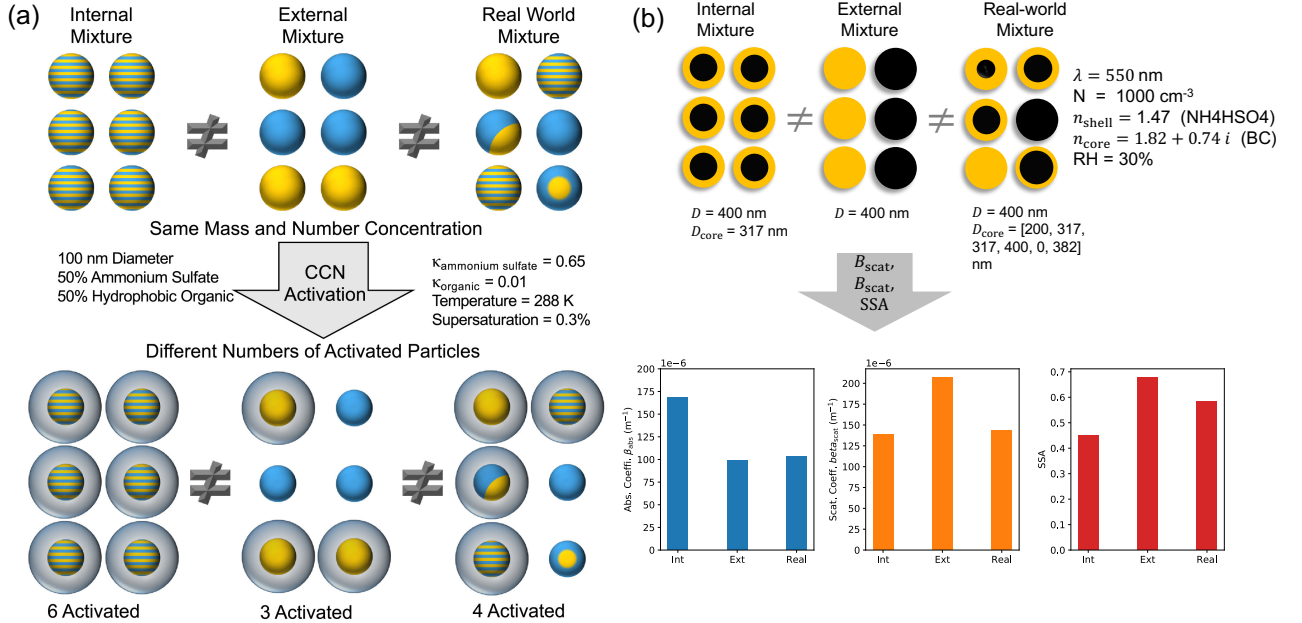


Figure 1.3: Aerosol mixing state effects on (a) activation ability and (b) optical values. (a) is adapted from Riemer et al. (2019).

internal mixture and the fully external mixture. As Fig. 1.3(a) schematically shows, a population is considered to be completely internally mixed if each particle is made up of the same species mixtures, which equals the bulk composition. For a population with fully external mixture, each particle only contains one single species. However, in the real ambient atmosphere, particles rarely fall into any of these two categories but most likely assume one of many possible intermediate mixing states. In other words, the number of species and their mass fractions can differ between particles.

Hygroscopicity and optical properties, which are important factors for droplets formation and the interaction with radiation, are both strongly dependent on the chemical species that the particle consists of. Thus, aerosol population with different mixing states may have different climate-related properties, as illustrated in Fig. 1.3. Figure 1.3(a) explains this for the example of cloud condensation nuclei activity. All three populations contain the same amount of ammonium sulfate and organic matter, but the two species are distributed differently among the particles. For the internally-mixed population, each particle has the same amount of ammonium sulfate and organic. For the externally-mixed population, each particle only contains one single species. In the real environment, these two species can be randomly distributed among the particles. If these three populations are exposed at the same supersaturation (e.g., a supersaturation of 0.3%), the number of activated particles will be different. All the particles are activated in the population with internal mixture, while only 50% are activated in the externally mixed population. The activated particles number in real world case are between these two extremes.

The effects of mixing state on aerosol activation potential has been investigated through closure studies. An

aerosol/CCN closure study is conducted by comparing the observed and predicted CCN concentrations at a given supersaturation level. The prediction is usually made by applying Köhler theory, using the measured dry particle size distributions and chemical composition information as input, with assumptions in mixing state to examine its effects. Broekhuizen et al. (2006a) performed such a closure study for aerosol samples from downtown Toronto at 0.58% supersaturation, and they found the internal mixture assumptions overpredicted CCN concentrations by 7–17%. Using the CCN sampled from 2010 CalNex field campaign, Moore et al. (2012) also found that internal mixture resulted in 30–75% overprediction of CCN concentration. Ervens et al. (2010) conducted a comprehensive closure study by using aerosol data collected from six different locations. They found, for regions that are affected by fresh emission, detailed size-resolved aerosol information are required to make a reasonable CCN prediction, while for regions are with aged aerosols, CCN can be well-predicted with simple (internally-mixed) aerosol representations.

As for the effects on aerosol optical properties, we can apply the same strategy as in Fig 1.3(a) to explain the relevance of mixing state. Figure 1.3(b) shows the populations with the same amount of absorbing species (BC) and non-absorbing species (NH_4HSO_4), but with different mixing states. As a result, the optical properties, including single scattering albedo (SSA), volume scattering coefficients (β_{abs}) and volume absorption coefficients (β_{abs}) are different and can lead to different radiative forcing.

The effects of aerosol mixing state on its optical properties can be more complicated if considering aerosol water uptake and particle shapes. In a humidified environment, water upda  a particle depends strongly on its composition because of the dependence of hygroscopicity on the chemical species, which is important for scattering (Michel Flores et al., 2012; Zieger et al., 2013; Titos et al., 2014, 2016). Studies showed, compared with a dry environment, the scattering ability can be enhanced by a factor of 1.6 at the environment with RH of 85% (Burgos et al., 2020). As for particle shapes, the distribution of the diverse species within a particle is important in determining optical values. For particles without strong absorber, i.e. BC, a volume-mixing rule can be used to calculate the overall refractive index of the particle. When the particle contains BC, assuming a core-shell configuration has been shown to be more accurate (Bond et al., 2006) than assuming a well-mixed particle. The absorption enhancement of BC-containing particles due to its coatings have been widely investigated (Moffet and Prather, 2009; Liu et al., 2017; Wu et al., 2020). The distribution of the non-absorbing species over the population were found to be the main sources for the discrepancies between the simulated and observed optical values (Fierce et al., 2016, 2020). That is, in order to simulate absorption enhancement correctly, it is important to know the coating thinkness for a given population of BC cores. In particular, assuming an internal mixture (where larger BC cores receive thicker coatings) leads to a systematic overestimation of the absorption enhancement. Considering the non-spherical shapes of BC-containing particles complicates the calculation of optical properties considerably. By using the Discrete Dipole Approximation (DDA) model, Scarnato et al. (2013) found that for mixed particles containing BC and NaCl, the absorption coefficients enhancement is higher

for internally mixed compact BC than lacy BC. However, the computational cost for DDA calculations is much higher than for Mie calculations.

1.4 Aerosol mixing state evolution

Aerosol mixing evolution in the atmosphere involves several processes. It is important to recognize that, at the time of emission, particles can already be a mixture of different species. For example, particles emitted from diesel engines are mixture of BC, primary organics and sulfate, and sea-spray aerosols are a mixture of sodium chloride and organics (Cheung et al., 2010; Kirpes et al., 2018). Once emitted, the mixing state can be further modified by condensation of organic or inorganic low-volatility compounds. Coagulation between particles is an efficient process for changing particle number concentration, and Brownian coagulation was shown to be the main reason for the rapid evolution of soot particle size distribution near a highway (Jacobson and Seinfeld, 2004). The coagulation process alone will make the particle composition more similar, and particle population undergoing coagulation will become more internally mixed (Riemer and West, 2013).

The processes of condensation and coagulation outlined above are relevant for a cloud-free environment  however, since the global cloud coverage is on average more than 70% (Stubenrauch et al., 2013), the aerosol evolution in clouds is also an important contributor during the lifetime of aerosol populations, and motivates the work presented in Chapter 2 and Chapter 3 of this thesis. Figure 1.4 shows the chemical and physical processes particles experience in fogs and clouds. When the atmosphere reaches supersaturation, particles with critical supersaturation lower than the environment supersaturation are activated as cloud droplets and undergo nucleation scavenging. For these activated particles, the absorbed water facilitates aqueous chemical reactions. Gas species dissolve in the cloud droplet, and if both liquid and ice phases exist in the cloud, species partition between the two phases and the retention coefficients in the liquid phase are varied. When cloud droplets grow to rain droplets, they precipitate. During precipitation, small interstitial aerosol particles can be collected by these large droplets and impaction scavenging occurs. For clouds with strong convection, gas and particle species are vertically redistributed by convective transport.

The aqueous phase in clouds provides an efficient medium for sulfate formation. Globally, more than 50% of sulfate forms through in-cloud oxidation and the formation rates of aqueous reactions, SO₂ oxidation by H₂O₂ and O₃, are more effective than through OH oxidation in gas phase (Kreidenweis et al., 2003b; Rasch et al., 2000). Other aqueous sulfate formation mechanisms, such as the reactions catalyzed by Transition Metal Ions (TMI), can also be important. For example, reaction cycles involving TMI have been shown to be the dominant pathway for sulfate formation in the samples collected during HCCT-2010 field campaign (Harris et al., 2012, 2013b).

In addition to sulfate, aqueous reactions can also form SOA. Globally, SOA produced from aqueous pathway

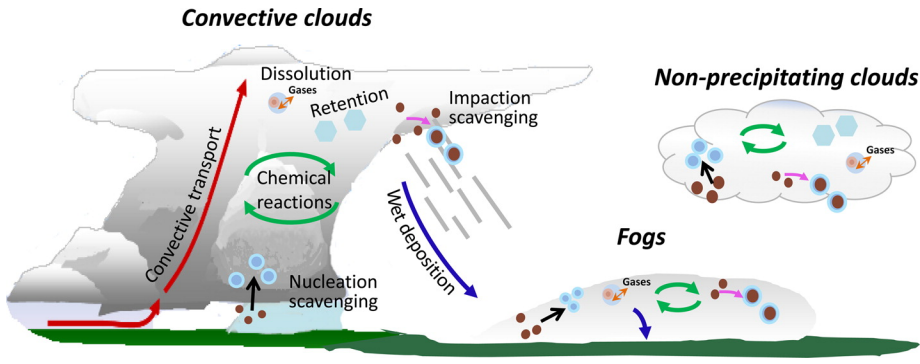


Figure 1.4: Chemical and physical processes involved in fogs and clouds, adapted from Ervens (2015b).

can reach to 20–30 Tg·yr⁻¹. Glyoxal, methylglyoxal, glycolaldehyde and acetic acid can act as the precursors for aqueous SOA (Liu et al., 2012a). As for the oxidants, besides hydroxyl radical, which is the dominant oxidant for SOA formation at gas phase, aqueous environment can provide several other efficient oxidants, such as peroxy radicals, peroxides and triplet excited states of organic compounds (³C*) (McNeill, 2015b; Ervens et al., 2011). Using simulated sunlight UV, Smith et al. (2014b) found phenols can be rapidly oxidized by ³C* to produce low-volatility SOA .

The aerosol size distribution evolves after the formation of aqueous inorganic and organic species. The characteristic “Hoppel minimum” describes the gap between two particle distribution modes at approximately 0.02–0.03 and 0.08–0.15 μm (Hoppel et al., 1986), evident in particle populations processed by non-precipitating clouds. After being described for the first time by Hoppel et al. (1986), this phenomena has further been observed for aerosol populations in different regions, such as during the VOCALS campaign over west Chilean coast (Kleinman et al., 2012) and the MASE campaign at the central California coast (Hudson et al., 2015). Besides the formation of secondary aerosol through aqueous phase reactions, particle size distributions also changes due to coagulation between interstitial particles and cloud droplets. Pierce et al. (2015a) found that this process can reduce total particle number concentration by 10–15% globally.

The evolution of mixing state in turn affects the aerosols’ climate-related properties. Ching et al. (2016a) found that for polluted environments where BC-containing particles age quickly, increased BC emissions result in larger cloud droplet number concentrations (even though fresh BC particles are poor CCN). Aerosol optical properties are altered as mixing state evolves, especially for BC-contained particles. As mentioned above, the absorption enhancement of BC-containing particles due to coatings of non-absorbing species are widely confirmed by models, laboratory studies and field observations (Moffet and Prather, 2009; Liu et al., 2017; Wu et al., 2020; Fierce et al., 2020).

Considering the importance of mixing state for describing an aerosol population, a qualitative description using the terms, such as internal or external mixture, are limited in quantifying the effects of mixing state. Riemer and West (2013), based on the theory of information-theoretic entropy, developed the index χ to quantify aerosol population

mixing state. The index χ is the ratio between average particle diversity D_{part} and bulk diversity D_{bulk} by using particle mass measurement data, these metrics were successfully proved to be capable of explaining the aerosol aging processes (Healy et al., 2014). They are also an important framework for our analyses presented in Chapter 3 and Chapter 4.

1.5 Aerosol modeling approaches

The application of a variety of aerosol measurement techniques helps advance our understanding of aerosol particles, and we know that the observed particles are the consequence of multiple chemical and physical processes. By using numerical models, we can isolate the underlying individual processes, and predict what will happen if certain processes change. Considering the wide range of chemical species and particle sizes in an aerosol population, it is hard for a single model to represent all possible processes the population can experience during its lifetime, from emission to deposition, and balance need to be reached between model accuracy and computational efficiency. This section summarizes the current aerosol modeling approaches from simplistic bulk methods used in some global models to comprehensive particle-resolved models used in box model. We will focus on how these models deal with aerosol mixing state and its implication for aerosol-related climate properties.

1.5.1 Bulk models

The simplest aerosol modeling approach is the so-called bulk method, as shown in Fig. 1.5(a). Aerosol populations are represented by the mass concentrations of several common aerosol species, such as sulfate, BC, organic aerosol, dust and sea salt, and these species are treated as external mixtures in the bulk without detailed information about how the species may be mixed with each other. Rather than tracking the aerosol evolution through microphysical processes, this approach prescribes the aerosol size distribution from climatological data. This approach is computationally very efficient and applied by several global models, such as GOCART (Chin et al., 2000) and TM5 (Vignati et al., 2010).

1.5.2 Modal models

A more advanced approach is representing the aerosol populations by several overlapping distributions, also called modes, as shown in Fig. 1.5(b). A modal model tracks the size distribution evolution of the modes. Each mode can contain a variety of aerosol species. Within each mode, all species are assumed to be internally mixed. Since the modes can overlap in certain size ranges, mixing state can be represented at least in a simplified way, especially when many modes are used (Bauer et al., 2008). Lognormal functions are typically used to represent the number distribution

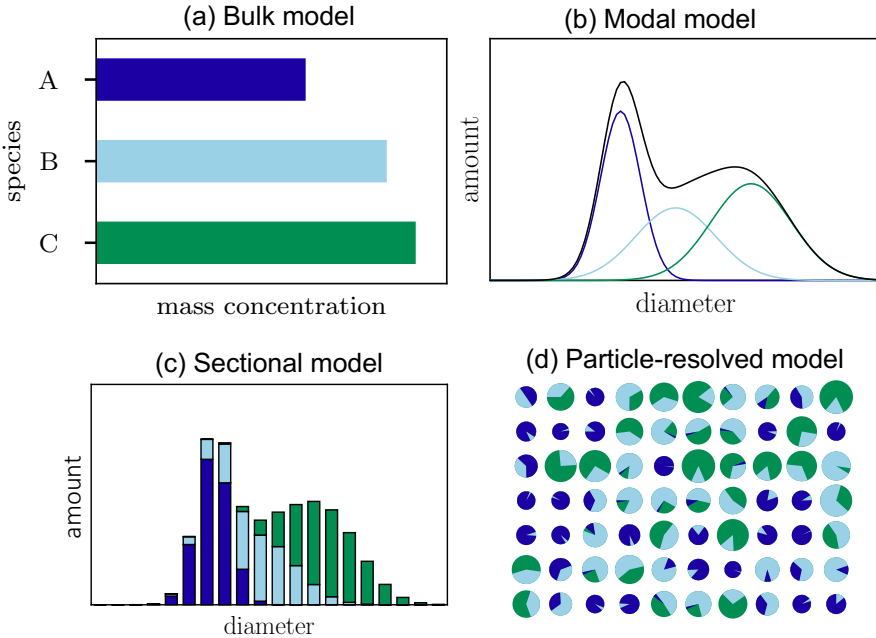


Figure 1.5: Aerosol numerical approaches:(a) Bulk model, (b) Modal model, (c) Sectional model, and (d) Particle-resolved model.

of each mode as follows:

$$n(\log D_p) = \sum_{i=1}^m \frac{N_i}{\sqrt{2\pi}\log\sigma_i} \exp\left(-\frac{(\log D - \log \bar{D}_i)^2}{2\log^2\sigma_i}\right), \quad (1.1)$$

where m is the number of modes, N_i is the total number concentration of mode i , \bar{D}_i and σ_i are the geometric mean diameter and geometric standard deviation of mode i , respectively.

The number of modes can vary among different models. Aitken, accumulation and coarse modes are the essential three modes, and this configuration is for example used in the ECHAM4 global climate model (Lauer et al., 2005) and in the regional chemistry transport model (Binkowski and Roselle, 2003). Other models introduce additional modes to better represent hydrophilic and hydrophobic species. For example, MAM7 used in the CAM5 global model applies an additional primary carbonaceous mode that represents primary organic matter and BC, which has lower hygroscopicity than the accumulation mode (Liu et al., 2012c) that also contains sulfate and SOA. For the three parameters used to describe the lognormal distribution, standard deviation of each mode is typically prescribed, and total number concentration and geometric mean diameter change as the aerosol evolves.

1.5.3 Sectional models

Similar to modal methods, sectional aerosol models are also distribution-based. Instead of tracking the population by different modes, this approach discretizes the distribution into a certain number of size bins and then track the changes in each bin, as illustrated in Fig. 1.5(b). Particles are internally mixed within each bins and the composition can vary between bins. The sectional approach is widely applied to large-scale models. For example, the sectional model MOSAIC is extensively used in WRF-Chem with 4-bin and 8-bin versions available, and proved to capture the summer particulate matter distribution well over the Houston region (Zaveri et al., 2008b; Fast et al., 2006). The TOMAS sectional model is applied to several global chemistry models, such as GEOS-Chem, and improved its ability in simulating aerosol optical properties recently through more detail mixing state representation of particles (Adams and Seinfeld, 2002; Pierce et al., 2013; Kodros et al., 2018). TOMAS uses 30 bins and covers the diameter range between 0.01 and $10 \mu\text{m}$.

Most sectional models apply univariate distributions and use assumptions for the aerosol mixing state in each bin. Some more advanced schemes have been developed to incorporate more information within each size bin, especially for representing a variable BC mass fraction within each size bin. Based on the Model of Aerosol Dynamics, Reaction, Ionization, and Dissolution (MADRID) module, Oshima et al. (2009) developed a two-dimensional sectional scheme MADRID-BC by adding another dimension for BC mass fraction and tracking the fraction changes due to condensation/evaporation processes. Through developing MOSAIC-MIX, Ching et al. (2016b) further extended the sectional model representation by incorporating another dimension for hygroscopicity, and coagulation process had been added to evaluate its effects on BC mixing state.

1.5.4 Particle-resolved models

Even though modal and sectional models provide better representation of particle size distributions than bulk models, aerosol mixing state still needs to be represented in a simplified way by using internal or external assumptions. A more advanced representation of aerosol mixing state is the particle-resolved method, as illustrated in Fig. 1.5(c). Rather than using distributions to represent the population, a particle-resolved model samples the population with discrete computational particles. Specifically, each particle is represented by an A -dimensional vector, where A is the total species number. The first particle-resolved aerosol model for the ambient atmosphere was developed by Riemer et al. (2009) and it was coupled with the MOSAIC module to include gas-particle partitioning and gas chemistry processes. The model was applied to investigate the aging process of BC-containing particles in a urban plume environment and the evolution of ship plume particles (Tian et al., 2014; Ching et al., 2016a). Recently, PartMC-MOSAIC had been further coupled with WRF-chem to track the particle evolution for a large-scale domain (Curtis et al., 2017). However, MOSAIC only considered aerosol aging process for subsaturated environments ($\text{RH} < 100\%$). It can not be used to

investigate the chemical processes in a cloud environment. Extending and applying the PartMC modeling framework to include aqueous phase chemistry is one of the goal for this thesis. More details about PartMC will be presented in Chapter 2.

In summary, the bulk model approach is the most simplified method with mixing state being represented by an external mixture of different particle types. Modal and sectional models represent aerosol populations by distributions. Their ability to describe aerosol mixing state is limited by the number of modes or bins included in the models and they still rely on assumptions for mixing state within modes or bins. With the particle-resolved approach, each computational particle is explicitly tracked and the mixing state of aerosol population is accurately represented.

1.6 Models for aqueous chemistry simulation

One of the topics for the thesis is to investigate the impact of aqueous phase chemistry on aerosol mixing state. The previous section discussed different approaches to simulate aerosol composition and represent mixing state. This section summarizes how aqueous phase chemistry mechanisms are incorporated into models. From particle activation at nanometer scale to stratocumulus structures over thousand kilometers, cloud processes cover around 10^{14} orders of magnitude, and it is infeasible for a single model to incorporate all the related processes. Models with aqueous processes can be divided into two groups: process model with explicit aerosol microphysics and complex aqueous chemical mechanisms, and large-scale model with simplified representation of cloud properties and processes.

For process models, often used as box/parcel models, aerosol microphysics is usually well-resolved. Droplet activation is explicitly described by using Köhler theory. Specifically, particles with critical supersaturation lower than maximum supersaturation reached in the environment are activated as droplets (Rothenberg and Wang, 2016; Ching et al., 2012). Detailed aqueous chemistry processes can be incorporated into these cloud parcel models. An example is the cloud parcel model SPACCIM coupled with the detailed aqueous scheme CAPRAM (492 species and 1087 reactions in version 3.0). It has been successfully compared to measurements during the FEBUKO campaign (Wolke et al., 2005a). Since particle size distributions are commonly described in process models, the modification of the size distribution after cloud processes can also be captured. The limitation of these models is the lack of the interactions with the cloud dynamics.

It is hard to include such detailed process information in global models where computational efficiency is very important. Rather than resolving cloud microphysics explicitly, cloud properties are described in a highly parameterized way, by using cloud fraction, with other diagnosed meteorological parameters, for each grid box. Cloud droplet sizes distributions are usually assumed. For example, ECHAM5-HAM assumed two bins for the cloud droplets: one bin for particles with lower ion concentration and the other bin for high ion concentration. As for the effects of cloud droplets

representation on cloud chemistry, Barth (2006b), by comparing sectional and single-size droplet parcel model, found simplified cloud droplet size representation will lead to biases in simulated formic acid and formaldehyde concentration. Simplified aqueous mechanisms are also used and the acidity, which is an important factor for aqueous chemistry, are fixed at constant value. For example, GEOS-Chem used a pH of 4.5 for SO₂ oxidation reaction by O₃(Park et al., 2004). Furthermore, assumptions need to be made to consider the distribution of species produced from aqueous reactions. For example, in CMAQ, all the non-volatile aqueous-formed species are added to accumulation mode after cloud dissipates (Binkowski and Roselle, 2003; Fahey et al., 2017a).

1.7 Research questions and thesis organization

Aerosol particles affect climate forcing through directly altering radiation and indirectly interactions with clouds. These effects are dependent on the particles' chemical composition, in other words, the chemical species mixing state of the aerosol population. The objective of this dissertation includes two parts: quantifying cloud chemical processes and their impact on mixing state, and quantifying the effects of aerosol mixing state on aerosol optical properties.

For the first part, I will focus on the following scientific questions: (1.1) To what extent does cloud processing change the aerosol mixing state of the population that entered the cloud? (1.2) How does this change the cloud condensation number concentration and optical properties? (1.3) What is the implication of coagulation between the interstitial particles and cloud droplets for mixing state of aerosol population?

For the second part, the following two questions will be addressed: (2.1) What are the errors in aerosol optical properties introduced by internal mixture assumptions used in sectional models? (2.2) How does this error depend on relative humidity and associated water uptake of the aerosol?

Both objectives are addressed with a particle-resolved modeling approach. Chapter 2 describes the coupling of the particle-resolved model PartMC-MOSAIC with the aqueous mechanism CAPRAM. Chapter 2 also presents the results from idealized model simulations to confirm expected sensitivities of sulfate formation to model input parameters.

Chapter 3 investigates the cloud processing effects on aerosol properties. In this work, I used a typical urban plume particle population to experience several idealized cloud cycles to determine the changes of aerosol mixing state and quantify the changes of aerosol microphysical and optical properties after the cloud evaporates. Another simulation is conducted to identify the role of coagulation between cloud droplets and interstitial particles. This chapter will answer questions 1.2–1.4. A paper entitled “The impacts of cloud processing on resuspended aerosol particles after cloud evaporation”, which is in review for *Journal of Geophysical Research-Atmosphere*, summarizes the results on the changes of aerosol microphysical properties after cloud processing. Another paper, which is entitled with “Quantifying the Effects of Cloud Processing on Aerosol Optical Properties Using a Particle-Resolved Model”

about the changes of optical properties after cloud processing, is in preparation for *Aerosol Science and Technology*.

Chapter 4 evaluates the error in aerosol absorption and scattering, introduced by the internal mixture assumptions used in sectional aerosol models. The error is quantified by comparing the aerosol optical value differences between reference populations created by running particle-resolved model and sensitivity populations with reduced representation of mixing state created by composition-averaging methods. This chapter will answer the two questions pertaining to the second part and a publication is in preparation for *Atmospheric Chemistry and Physics*, entitled “Quantifying the effects of mixing state on aerosol optical properties”.

Chapter 5 summarizes the main findings of this thesis and discusses implications for resolving aerosol mixing state in the future for global models.

Chapter 2

Particle-resolved modeling of aqueous-phase chemistry

This chapter presents the application of PartMC as a particle-resolved cloud parcel model that includes aqueous-phase chemistry. I first describe the PartMC model framework, and the coupled cloud parcel and aqueous chemistry module as it was used in both this chapter and Chapter 3. Then, I present a comparison to other size-resolved and bulk cloud chemistry models. Furthermore, I show results from an ensemble of idealized scenarios that were designed to confirm the sensitivity of aqueous sulfate formation to the concentrations of oxidants and to transition metal ions.

2.1 Introduction

Clouds cover around 70% of the earth (Stubenrauch et al., 2013) and create an environment for multiphase reactions to occur (Deguillaume et al., 2005). Gas phase species are taken up by cloud droplets and undergo aqueous-phase chemistry. Oxidation of dissolved gases in the aqueous phase can contribute to a large fraction of secondary inorganic and organic aerosol. Globally, over 50% of sulfate is produced through aqueous reactions in clouds (Philip et al., 2014; Roth et al., 2016). If the cloud evaporates, an aerosol population is released that has different cloud condensation nuclei properties and optical properties compared to the aerosol that formed the cloud (Farmer et al., 2015; Henning et al., 2014).

Particles with different composition and size experience different effects from aqueous-phase chemical processing. First, particle size and composition determine which particles can be activated and form cloud droplets. Second, some aqueous-phase sulfate formation reactions are highly pH-dependent, and the reaction rates for particles with different acidity can vary by several orders in magnitude. For example, transition metal ions (TMI), including Fe and Mn ions, which mostly originate from mineral dust (Alexander et al., 2009c), catalyze aqueous sulfate oxidation reactions. The related pathways become dominant when the pH is larger than 6.0 (Seinfeld and Pandis, 2006). It had been shown that at some cloud events, the SO_2 oxidation reaction catalyzed by coarse mineral dust TMI can be more efficient than the oxidation by H_2O_2 (Harris et al., 2013a, 2014).

Despite the potential importance of particle heterogeneity in aqueous-phase chemistry, most regional or global models use simplified assumptions to simulate aqueous processes. The global chemistry transport model GEOS-

Chem uses less than 10 dissolved species calculate acidity (Alexander et al., 2012). The regional chemical transport model CMAQ tracks cloud chemistry processes for three lognormal modes, neglecting the heterogeneity within each mode (Fahey et al., 2017a). In this work, I applied the particle-resolved model PartMC-MOSAIC (Riemer et al., 2009; Zaveri et al., 2010), which tracks individual computational particles. The model has been widely used to study aerosol aging processes in a cloud-free environment (Zaveri et al., 2010; Fierce et al., 2015). It has also been used as a cloud parcel model to investigate the impact of aerosol mixing state on cloud droplet formation (Ching et al., 2012, 2016a). However, the model did not have the capability to simulate aerosol aging due to aqueous-phase chemistry within clouds. This is the focus of this chapter.

The remainder of this chapter is structured as follows. Chapter 2.2 describes the PartMC modeling framework used for this thesis. Chapter 2.3 compares results from the particle-resolved aqueous-phase chemistry model with results from existing literature. Chapter 2.4 explores the sensitivity of sulfate formation to input parameters using an ensemble of idealized simulations. The role of TMI pathway is further explored in Chapter 2.5. Findings are summarized in Chapter 2.6.

2.2 Model description and simulation setup

The model simulations presented in Chapter 2 and 3 follow the two-step strategy described in Ching et al. (2012) and illustrated in Figure 2.1. For the first step, I simulated urban plume scenarios in a cloud-free environment using PartMC-MOSAIC. The purpose of these simulations was to produce many aerosol populations with a wide variety of aerosol mixing states. These simulated aerosol populations were then used as the input for cloud parcel simulations, including aqueous-phase chemistry, in Step 2. Details about PartMC-MOSAIC, the cloud parcel model and the aqueous-phase chemistry are described in the following sections.

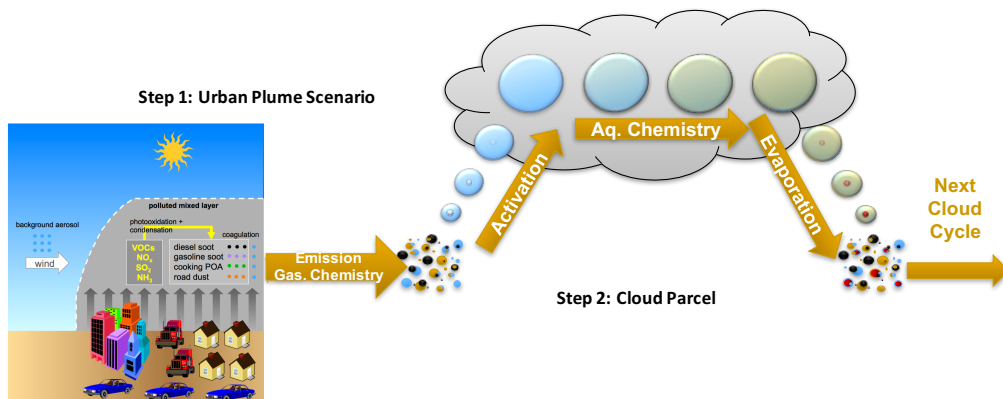


Figure 2.1: Two-step particle-resolved modeling framework. Step 1 is the simulation of an urban plume scenario in a cloud-free environment. Step 2 is the cloud parcel simulation using output from the Step-1 urban plume simulations as input.

2.2.1 The particle-resolved aerosol model PartMC-MOSAIC

PartMC-MOSAIC (Particle Monte Carlo-Model for Simulating Aerosol Interactions and Chemistry) is a Lagrangian box model which simulates the evolution of individual computational particles in the ambient atmosphere. The evolution is simulated assuming a well-mixed computational volume and the particles' spatial positions are not stored. The composition of each particle is tracked by representing the particle as an A -dimension vector $\vec{\mu}^i \in \mathbb{R}^A$ with components $(\vec{\mu}_1^i, \vec{\mu}_2^i, \dots, \vec{\mu}_A^i)$, where $\vec{\mu}_a^i$ is the mass of species a in particle i , with $a = 1, \dots, A$ and $i = 1, \dots, N$. The evolution for aerosol number concentration with species mass μ at time t , $n(\vec{\mu}, t)$, is described by:

$$\begin{aligned} \frac{\partial n(\vec{\mu}, t)}{\partial t} = & \underbrace{\frac{1}{2} \int_0^{\mu_1} \int_0^{\mu_2} \dots \int_0^{\mu_A} K(\vec{\mu}', \vec{\mu} - \vec{\mu}') n(\vec{\mu}', t) n(\vec{\mu} - \vec{\mu}', t) d\mu_1' d\mu_2' \dots d\mu_A'}_{\text{coagulation gain}} \\ & - \underbrace{\int_0^\infty \int_0^\infty \dots \int_0^\infty K(\vec{\mu}, \vec{\mu}') n(\vec{\mu}, t) n(\vec{\mu}', t) d\mu_1' d\mu_2' \dots d\mu_A'}_{\text{coagulation loss}} + \underbrace{\dot{n}_{\text{emit}}(\vec{\mu}, t)}_{\text{emission}} + \underbrace{\lambda_{\text{dil}}(t)(n_{\text{back}}(\vec{\mu}, t)) - n(\vec{\mu}, t)}_{\text{dilution}} \\ & - \underbrace{\sum_{i=1}^C \frac{\partial}{\partial \mu_i} (c_i I_i(\vec{\mu}, \vec{g}, t)) n(\vec{\mu}, t)}_{\text{gas-particle transfer}} - \underbrace{\frac{\partial}{\partial \mu_{C+1}} (c_w I_w(\vec{\mu}, \vec{g}, t)) n(\vec{\mu}, t)}_{\text{water transfer}} + \underbrace{\frac{1}{\rho_{\text{dry}}(t)} \frac{d\rho_{\text{dry}}(t)}{dt} n(\vec{\mu}, t)}_{\text{air density change}}, \end{aligned} \quad (2.1)$$

where K is the coagulation rate between the particles, $\dot{n}_{\text{emit}}(\vec{\mu}, t)$ is the emitting distribution of species $\vec{\mu}$, λ_{dil} is the dilution rate with background species concentration n_{back} , c_i is the gas to particle conversion rate, I_i is the gas species condensation flux, c_w is the gas to water conversion rate and I_w is the water condensation flux.

The evolution of gas species g_i at time t is given by:

$$\begin{aligned} \frac{dg_i(t)}{dt} = & \underbrace{\dot{g}_{\text{emit},i}(t)}_{\text{emission}} + \underbrace{\lambda_{\text{dil}}(t)(g_{\text{back},i}(t) - g_i(t))}_{\text{dilution}} + \underbrace{R_i(\vec{g})}_{\text{chemical reactions}} + \underbrace{\frac{1}{\rho_{\text{dry}}(t)} \frac{d\rho_{\text{dry}}(t)}{dt} g_i(t)}_{\text{air density change}} \\ & - \underbrace{\int_0^\infty \int_0^\infty \dots \int_0^\infty I_i(\vec{\mu}, \vec{g}, t) n(\vec{\mu}, t) d\mu_1 d\mu_2 \dots d\mu_A}_{\text{gas-particle transfer}}, \end{aligned} \quad (2.2)$$

where $\dot{g}_{\text{emit},i}(t)$ represents gas species i emitting rate, $g_{\text{back},i}$ is for gas species i background concentration, and $R_i(\vec{g})$ is the gas species i production rate from chemical reactions.

The evolution processes represented in equation 2.1 alter the aerosol population by two mechanisms. By adding or removing particles from the population, emission, dilution and coagulation processes modify the number concentration of the population and these processes are accomplished by PartMC with a stochastic Monte Carlo approach. In addition, the composition of each particle can be altered by species condensation and evaporation, which are simulated

by the state-of-art aerosol chemistry module MOSAIC. In MOSAIC, gas phase reactions are represented by the arbon bond mechanism CBM-Z, with 77 species and 142 reactions included (Zaveri, 1999). Key aerosol species are treated, including SO_4^{2-} , NO_3^- , NH_4^+ , BC, primary organic aerosol (POA) and secondary organic aerosol (SOA). The SOA treatment is based on the SORGAM scheme (Schell et al., 2001b). In the current version, the model includes four SOA species (ARO1, ARO2, ALK1, OLE1) formed from anthropogenic volatile organic compounds (VOCs) precursors, and four other SOA species (LIM1, LIM2, API1, API2) formed from biogenic VOCs (Ching et al., 2012). Activity coefficients of electrolytes and ions in aqueous solutions are estimated by the multicomponent Taylor expansion method (MTEM), and intraparticle solid-liquid partitioning is treated by the Multicomponent Equilibrium Solver for Aerosols (MESA) (Zaveri et al., 2005b). However, MOSAIC only considers the reactions occurring in an environment that is subsaturated with respect to water vapor ($\text{RH} < 100\%$) and therefore we were not able to address the changes to aerosol composition during a cloud exists. This is the contribution of this work.

PartMC-MOSAIC was applied to analyze the particle evolution at different environments. For example, Zaveri et al. (2010) found that aerosol absorption of sunlight increased by 40% during a 48-hour idealized urban plume condition due to the aging of BC-containing particles. Tian et al. (2014) used the model to investigate the processes responsible for the particle number concentration change in a ship plume and evaluated the effects of different aging processes on particle CCN properties. PartMC-MOSAIC was also used as a benchmark model to quantify the errors in aerosol optical and microphysical properties introduced by simplified mixing state assumptions commonly used in other aerosol models (Zaveri et al., 2010; Ching et al., 2012; Fierce et al., 2017). PartMC-MOSAIC was further coupled with a cloud parcel model to investigate the effects of mixing state on cloud droplet properties (Ching et al., 2012, 2016a). The cloud parcel model will be discussed in more detail in section 2.2.2 because this model was applied for the research both in this chapter and chapter 3.

2.2.2 Cloud parcel model

PartMC can be used as a zero-dimensional adiabatic cloud parcel model (Ching et al., 2012). It simulates particle activation and condensational growth in a cooling air parcel and tracks the changes of environmental saturation due to the growth of particles and the temperature change. Specifically, for a population with N particles of diameter D_i , both the growth rate of D_i and the change of environment saturation S_v are predicted, which sums to $N + 1$ state variables to be numerically solved by the model. In the current version of the model, entrainment and surface tension effects on droplets growth are not included. This section briefly introduces the main equations solved by the parcel model. See Ching et al. (2012) for a more detailed description of the model.

In Ching et al. (2012), the chemical composition of the particles particle is assumed to be constant and only the water content of the particle changes during the condensational growth process. The growth rate of particle i is

calculated as

$$\frac{dD_i}{dt} = \frac{G}{D_i}(S_v - S_{\text{eq}}), \quad (2.3)$$

where the growth coefficient G and droplet equilibrium supersaturation S_{eq} are

$$G = \frac{4D'_{v,i}M_wP^0}{\rho_wRT}, \quad (2.4)$$

$$S_{\text{eq}} = \frac{a_{w,i}}{1 + \delta_i} \exp\left(\frac{4M_w\sigma_w}{\rho_wRTD_i} \frac{1}{1 + \delta_i} + \frac{\Delta H_v M_w}{RT} \frac{\delta_i}{1 + \delta_i}\right),$$

and $D'_{v,i}$ is the modified particle diffusivity, M_w and ρ_w are the water molecular weight and density, P^0 is the saturation vapor pressure, R is the gas constant, T is the environment temperature, $a_{w,i}$ is the water activity of the particle, σ_w is the water surface tension, ΔH_v is latent heat of vaporization, and δ_i is defined as

$$\delta_i = \frac{\Delta H \rho_w}{4k'_{a,i} T} D_i \frac{dD_i}{dt}, \quad (2.5)$$

where $k'_{a,i}$ is the corrected air thermal conductivity.

The water activity is calculated by using the parameter κ derived by Petters and Kreidenweis (2007) and can be expressed as

$$a_{w,i} = \frac{v_i^w}{v_i^w + \kappa_i v_i^{\text{dry}}}, \quad (2.6)$$

where v_i^w and v_i^{dry} are the volume of water and all the other dry components in particle i , respectively. κ_i is volume-weighted κ of the non-water species. We used κ of 0.65 for ammonium-sulfate-nitrate system, SOA with $\kappa = 0.1$ and POA with $\kappa = 0.001$. BC is assumed to be hydrophobic and has κ of 0.

Rather than describing the rising parcel using a constant updraft velocity (Seinfeld et al., 2016a; Rothenberg and Wang, 2016), this parcel model prescribes a constant temperature lapse rate, following the strategy used in Majeed and Wexler (2001) to avoid dealing with radiative heating effects and the latent heat budget. Pressure is also assumed to be constant. In light of these considerations, the change of environment saturation can be given by

$$\frac{dS_v}{dt} = - \sum_{i=1}^N \frac{\pi \rho_w R T}{2M_w P^0 V_{\text{comp}}} D_i^2 \frac{dD_i}{dt} - \frac{1}{P^0} \frac{\partial P^0}{\partial T} S_v \frac{dT}{dt}, \quad (2.7)$$

where the first term describes the effects due to the diameter change of all N particles and the second term represents the temperature change. V_{comp} is the computational volume.

PartMC was applied as cloud parcel model to investigate the importance of aerosol mixing state for predicting cloud droplets number concentration (CDNC). Ching et al. (2012) found that neglecting particle species heterogeneity in size bins resulted in errors in CDNC of up to 34% with a cooling rate of 0.5 K/min. By conducting ensemble cloud parcel simulations, Ching et al. (2016a) further demonstrated that ignoring BC mixing state can lead to CNDC errors of -12% to $+45\%$.

2.2.3 Aqueous chemistry model

PartMC was further enhanced with an aqueous chemistry module based on the reduced Chemical Aqueous Phase Radical Mechanism (CAPRAM) version 2.4. The full mechanism in CAPRAM 2.4 includes 439 reactions and 147 species, and the reduced version is also provided to be more computationally efficient, which includes 183 reactions and 113 species (Ervens, 2003). The reduced version also contains a comprehensive aqueous mechanism, and deals with the reactions between OH, HO₂, NO₃, SO₄, Cl₂, Br₂ and CO₃ with inorganic (TMI, NO₃⁻, Cl⁻, Br⁻) and organic reactants with less than two atoms. The constants for thermodynamic and kinetic reactions are listed in Table A in the appendix.

When coupling CAPRAM with PartMC, the original gas phase chemistry mechanism, regional atmospheric chemistry modeling (RACM), used in CAPRAM 2.4 was replaced with CBM-Z in PartMC-MOSAIC. It is worth noting that MOSAIC is not running when we have aqueous chemistry. In the current setting, aqueous chemistry, and the evaporation and condensation of gases (other than water vapor) to aqueous particles are enabled for particles with liquid water mass larger than 5×10^{-16} kg, which corresponds to solution droplets of 1 μm in diameter.

We used the CVODE Cohen et al. (1996) solver of the SUNDIALS Hindmarsh et al. (2005) package to solve the mass transfer and aqueous chemistry of the CAPRAM 2.4 reduced mechanism with the Backward Differentiation Formulas (BDF) and Newton Iteration, which is suitable for mathematically stiff systems, such as those treating multi-phase chemistry. To reduce the stiffness of the system, the Henry's Law partitioning of the strong acids H₂SO₄, HCl, and HNO₃ were combined with their first acid dissociation step. The coupling work was accomplished by Dr. Matt Dawson and the codes are available online (<https://github.com/compdyn/partmc/tree/aqchem>).

2.3 Sulfate mechanism verification

Before applying the comprehensive particle-resolved aqueous chemistry model to study the role of different aqueous sulfate pathways, I first evaluated it by comparing with the results in Kreidenweis et al. (2003b) (hereafter, KS2003). In KS2003, several bulk and size-resolved aqueous chemistry models were used to simulate aqueous sulfate formation in an adiabatic cloud parcel. They found significant differences in SO₂ oxidation rates between size-resolved and

bulk models. This model comparison work provides a benchmark for checking aqueous sulfate mechanisms, and I used the same simulation setting in that work to verify our particle-resolved aqueous chemistry approach. Physical and chemical parameters, including initial temperature, species concentration and chemical reactions are all set to the same with values used in KS2003, as listed in table 2.1. An important structural difference between the models used in KS2003 and the PartMC cloud parcel model is that in KS2003, a constant updraft velocity was prescribed. In contrast, in PartMC, as mentioned before, we predefined the temperature lapse rate. In order to simulate effectively the same updraft velocity, we obtained the temperature and pressure values of constant updraft velocity at 0.5 m/s from the pyrcel model, a zero-dimensional adiabatic cloud parcel model (Rothenberg and Wang, 2016), with the timestep of every 60s.

Table 2.1: Cloud chemical and physical conditions

Physical parameters	Value (Units)	Chemical parameters ($t = 0$)	Values Units
Temperature at $t = 0$	285.2 (K)	SO_2	200 (pptv)
Pressure at $t = 0$	950 (mbar)	NH_3	100 (pptv)
Updraft velocity	0.5 (m s $^{-1}$)	H_2O_2	500 (pptv)
Cloud water mixing ratio after 2400 s	2.17 (g kg $^{-1}$)	HNO_3	100 (pptv)
Air density at the cloud base	1.15 (kg m $^{-3}$)	O_3	50 (ppbv)
Cloud base temperature	284.2 K	CO_2	360 (ppmv)
Cloud base pressure	939 (mbar)	SO_4^{2-}	2 ($\mu\text{g m}^{-3}$)
Relative humidity at $t = 0$	95%	NH_4^+	0.375 ($\mu\text{g m}^{-3}$)

Figure 2.2(a) shows the simulated cloud liquid water content (LWC). PartMC simulated a somewhat larger increase in LWC, which is a result from the different cloud parcel model setups. As mentioned before, we prescribed a constant temperature lapse rate whereas for models used in KS2003, a constant updraft velocity was described. In the simulation shown here, the input temperature profile produced updraft velocity close to 0.5 m/s, but still with some fluctuations, which is the main reason for the LWC differences.

Another possible factor is the treatment of droplet surface temperature T , which is used to calculate the droplet growth rate. In the models used in KS2003 it was assumed that T equals the environment temperature T_∞ , whereas in our model this assumption was not used. However, upon further investigation, it turned out that this assumption did not cause the differences in LWC.

The simulated decrease in $\text{SO}_2(\text{g})$ mixing ratio is very similar between PartMC and KS2003 (Fig. 2.2(b)), with $\text{SO}_2(\text{g})$ mixing ratio decreasing from 0.2 to 0.025 ppb after 40 minutes, indicating PartMC is capable of simulating of aqueous sulfate formation processes. The bulk acidity calculated by PartMC also shows similar profile with the models in KS2003 but with higher values (Fig. 2.2(c)). Considering the different simulation approaches, we expect some differences between bulk or size-binned based pH and our particle-resolved pH.

Since the sulfate aqueous formation rate by O_3 increases exponentially with increasing pH, any differences in

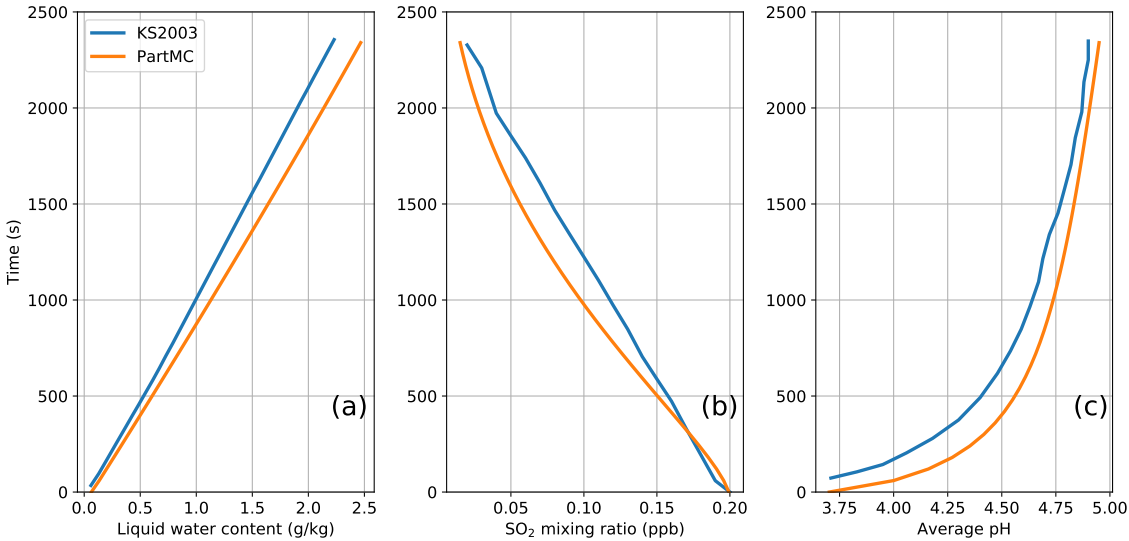


Figure 2.2: Vertical profile differences of (a) liquid water content and (b) Gas SO₂ concentration (c) Bulk pH between KS2003 and PartMC.

acidity differences will propagate into sulfate production. At the end of the simulation, PartMC simulated a sulfate mixing ratio of 207 ppb, higher than the ~ 175 in size-resolved models and ~ 145 in bulk models. As explained in KS2003, the excess produced sulfate in the size-resolved models are found to be associated with higher simulated pH and more sulfate formed from O₃ oxidation pathway. This explanation applies to our simulation results as well.

In summary, this comparison simulation proved our particle-resolved aqueous model is capable of capturing the sulfate aqueous chemical processes. With more detailed particle information, our particle-resolved approach may also provide more comprehensive understanding of different sulfate formation pathways, and this is explored in our next section.

2.4 Contribution of different aqueous sulfate formation pathways

2.4.1 Setup of idealized simulations using monodisperse aerosol

To explore sensitivities of sulfate formation to the input parameters (initial mixing ratios of selected gases and the cooling rate), I used an idealized setup with monodisperse distributions for the initial aerosol population. The purpose of these simulations is to confirm the expected dependence of sulfate formation rates on pH and on the presence of TMI.

The reference scenario ensemble exposed the monodisperse aerosol populations to different initial conditions, denoted as P_{ref} . The initial particle size was 100 nm, composed of ammonium sulfate. Emission of particle and

gases and dilution with background air were not included. The initial mixing ratios of O₃, H₂O₂, NH₃ and SO₂, were perturbed at low, medium and high polluted levels, as listed in table 2.2. Gas phase SO₂ was selected because it provides the source of S(IV). The gas species O₃ and H₂O₂ were selected because they are the important oxidants for sulfate formation. Ammonia also plays an important role in aqueous sulfate formation by changing the droplet pH. The range of mixing ratios for the different gas phase species are consistent with observations in the ambient atmosphere. The O₃ and SO₂ values were based on the national-wide urban measurements in China (Wang et al., 2014), and NH₃ levels were determined from the observations of Houston, U.S. (Nowak et al., 2010) and Seoul, Korea (Phan et al., 2013). The values for H₂O₂ were based on the measurements in Guangzhou, China (Hua et al., 2008). The three different cooling rates provided conditions with different liquid water content. The corresponded cloud updraft velocity were 1.1, 1.5 and 1.8 m s⁻¹ respectively, which represented the conditions of strong convective stratus (Peng et al., 2005). It is worth mentioned that updraft velocities can change during the simulation period due to droplets formation. A total of 3⁵ = 243 cases were run using all possible combinations of input values to create this ensemble of scenarios.

Table 2.2: Settings for the initial conditions of the ensemble of scenarios denoted by P_{ref}

Parameters	Low	Medium	High
O ₃	25	50	75
H ₂ O ₂	0.25	0.5	1
NH ₃	2	4	6
SO ₂	2	5	10
$\frac{dT}{dt}$	-0.3	-0.4	-0.5

The initial RH was 99% and each simulation time was 20 minutes. As shown in Fig. 2.3, cases with larger cooling rate experienced more rapid increase of liquid water content, while the maximum supersaturation was similar for all cases. Cloud droplets formed in the first minute and the maximum supersaturation was 0.2%.

To explore the sensitivity of sulfate formation to the presence of TMI, another scenario ensemble was created, denoted as P_{TMI} , by adding Fe(II) and Fe(III) in the initial aerosol population, with mass fractions of Fe(II) and Fe(III) to be 0.05 and 0.01. We selected these two Fe mass fraction values to produce Fe molar concentration consistent with previous studies (Deguillaume et al., 2005). Otherwise the setup was the same as for P_{ref} , which resulted in another 243 cases for P_{TMI} . An important lesson of the P_{TMI} simulations was that aqueous hydroxide needed to be present for TMI oxidation pathways to proceed, with typical concentrations on the order of 10⁻¹³ M (Deguillaume et al., 2004). Since OH was quickly depleted in our initial setup, additional OH was supplied as emissions at the rate of 2×10^{-8} mole/m²/s to maintain the level of OH in the aqueous phase.

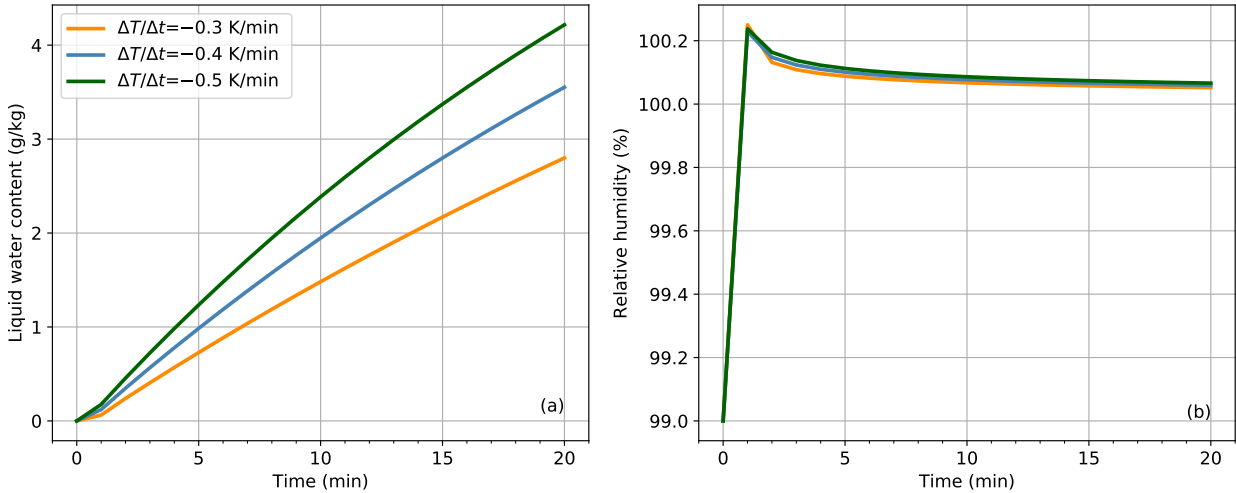


Figure 2.3: Time series of (a) liquid water content and (b) relative humidity in the ensemble of scenarios in P_{ref} .

2.4.2 Monodisperse aerosol simulation results

This section explores the sensitivity of sulfate formation to selected input parameters by analyzing the 243 aerosol populations in P_{ref} . Figure 2.4 shows the sulfate mixing ratio for all scenarios, stratified by the five different input parameters, including NH_3 , H_2O_2 , O_3 , SO_2 , and the temperature lapse rate.

A clear separation exists between the cases with different initial ammonia gas mixing ratio, where higher sulfate production is associated with higher initial ammonia mixing ratio. However, this separation is not as clear for the other four parameters. This reflects the fact that the sulfate production rates change over time within the cloud droplets as the concentrations of aqueous-phase species involved in sulfate production also change. While the initial conditions of H_2O_2 and O_3 play some role, they do not entirely determine the outcome. Cases with higher sulfate formation (the blue curves in Figure 2.4a) are seen with all levels of temperature lapse rate, $\text{H}_2\text{O}_2(\text{g})$ and $\text{O}_3(\text{g})$ mixing ratio. However, the highest sulfate mixing ratios are associated with high initial O_3 and SO_2 mixing ratios. This phenomenon indicates that the ammonia gas phase mixing ratio is a determining factor for aqueous sulfate formation in the simulated scenarios under consideration. Next, we will look into the underlying mechanism.

Gas SO_2 is highly soluble to water and it dissolves rapidly. The dissolved SO_2 in the cloud droplets can appear in three S(IV) forms: $\text{SO}_2 \cdot \text{H}_2\text{O}$, HSO_3^- and SO_3^{2-} . S(IV) is then oxidized to S(VI) (sulfate). Here, I analyzed four key

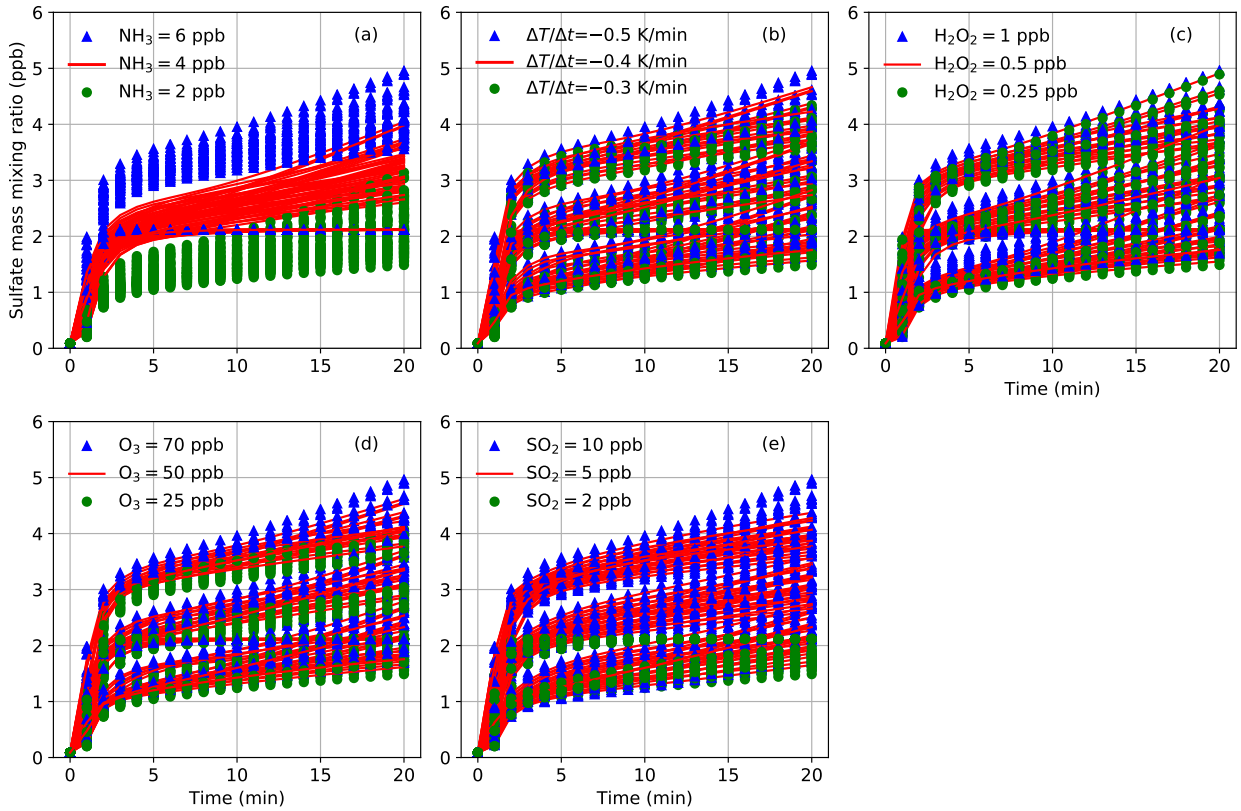
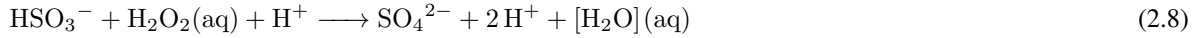


Figure 2.4: Sulfate time series categorized by five different settings in P_{ref} : (a) initial $\text{NH}_3(\text{g})$ mixing ratio, (b) temperature lapse rate, (c) initial $\text{H}_2\text{O}_2(\text{g})$ mixing ratio, (d) initial $\text{O}_3(\text{g})$ mixing ratio, and (e) initial $\text{SO}_2(\text{g})$ mixing ratio. The three colors and symbols are for the low, medium and high levels of each parameter.

oxidation pathways which transfer the S(IV) species to S(VI):



This section will focus on the discussion of the first three oxidation pathways and transition pathway reaction 2.11 will be discussed in next section.

Figure 2.5 shows the relationship between sulfate mixing ratio and particle acidity at 3 min. For the cases with the same initial $\text{SO}_2(\text{g})$, the sulfate mixing ratio is higher for higher initial $\text{NH}_3(\text{g})$. Considering the cases with $\text{SO}_2(\text{g})$ of 5 ppb and $\text{O}_3(\text{g})$ of 50 ppb (the cases in the red boxes of Fig 2.5), the only differences for these cases are the initial $\text{NH}_3(\text{g})$ values. For all three cooling rates, when $\text{NH}_3(\text{g})$ increased from 2 to 6 ppb, pH increased from 5.0

to over 5.5 and sulfate mixing ratio increased from 1 ppb to more than 2.5 ppb. This is because the reaction rates of the O_3 pathways increase for higher pH (Fig. 2.6). Fig. 2.6 also shows that for cases with 10 ppb SO_2 , H_2O_2 reaction rates are almost constant at all NH_3 levels. The different responses of O_3 and H_2O_2 pathways are consistent with the descriptions in Seinfeld et al. (2016a). For O_3 pathways, high pH leads to high S(IV) solubility and reaction rates increased (the cases in the red boxes of Fig 2.6). The reactions are self-limiting because the produced sulfate will increase acidity and decrease pH. In contrast, the H_2O_2 pathway is insensitive to pH because of the canceling effects between increased S(IV) concentration and reduced reaction constants. For the cases with 2 ppb initial SO_2 , the reaction rates are smaller for the cases with higher NH_3 and pH. These are $SO_2(g)$ -limited cases and less dissolved SO_2 is responsible for this.

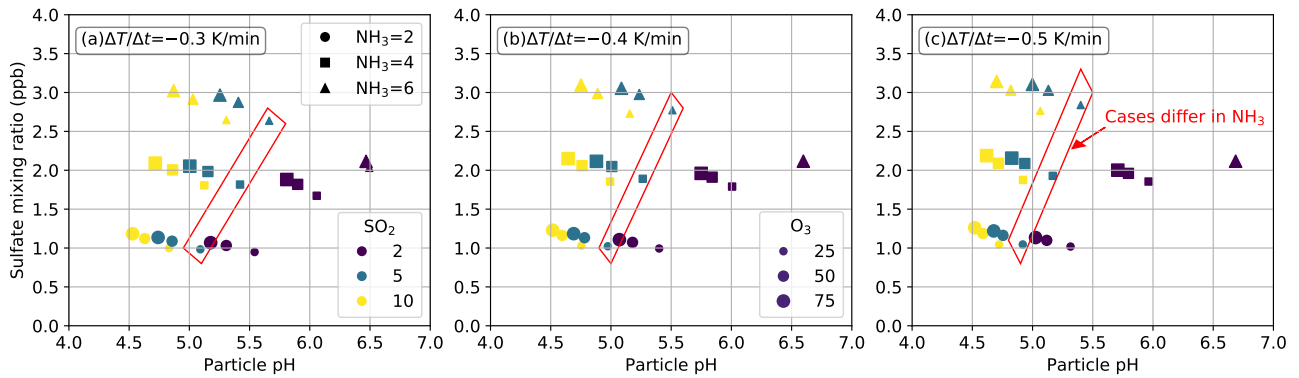


Figure 2.5: Correlation between sulfate mixing ratio and acidity at 3 min. (a) is for cases with temperature lapse rate of -0.3 K/min . (b) is for cases with temperature lapse rate of -0.4 K/min . (c) is for cases with temperature lapse rate of -0.5 K/min . Symbols in the plots are colored by $SO_2(g)$ levels and symbol types are for $NH_3(g)$ levels. All the cases in the figure are with $H_2O_2(g) = 0.5 \text{ ppb}$. Red boxes are for the aerosol populations with only differences in $NH_3(g)$ and are analyzed for detail in the text.

As for the sensitivity to temperature, there is no significant differences for cases with different cooling rates (Fig 2.6). As Seinfeld et al. (2016a) described, the effects of temperature on reaction rates are the balancing effects between two factors. On the hand, lower temperature leads to higher solubility and higher reactions rates. On the other hand, reaction constants decrease with lower temperature. Thus, when temperature changes, the behaviour of reactions rates are determined by which factor is dominant.

Based on analysis for the cases in P_{ref} , we can conclude that the aqueous sulfate formation is most sensitive to the initial $SO_2(g)$ and initial $NH_3(g)$ mixing ratios. Cases with most sulfate formation were for the cases with high $NH_3(g)$ values and this can be explained by the higher oxidation rates of SO_3^{2-} by $O_3(aq)$. Cases with higher $NH_3(g)$ but lower sulfate production were because of a lower supply of $SO_2(g)$, making sulfate formation was $SO_2(g)$ -limited. Overall, our particle-resolved aqueous chemistry model is capable of simulating the expected response of O_3 and H_2O_2 pathways to temperature and acidity changes.

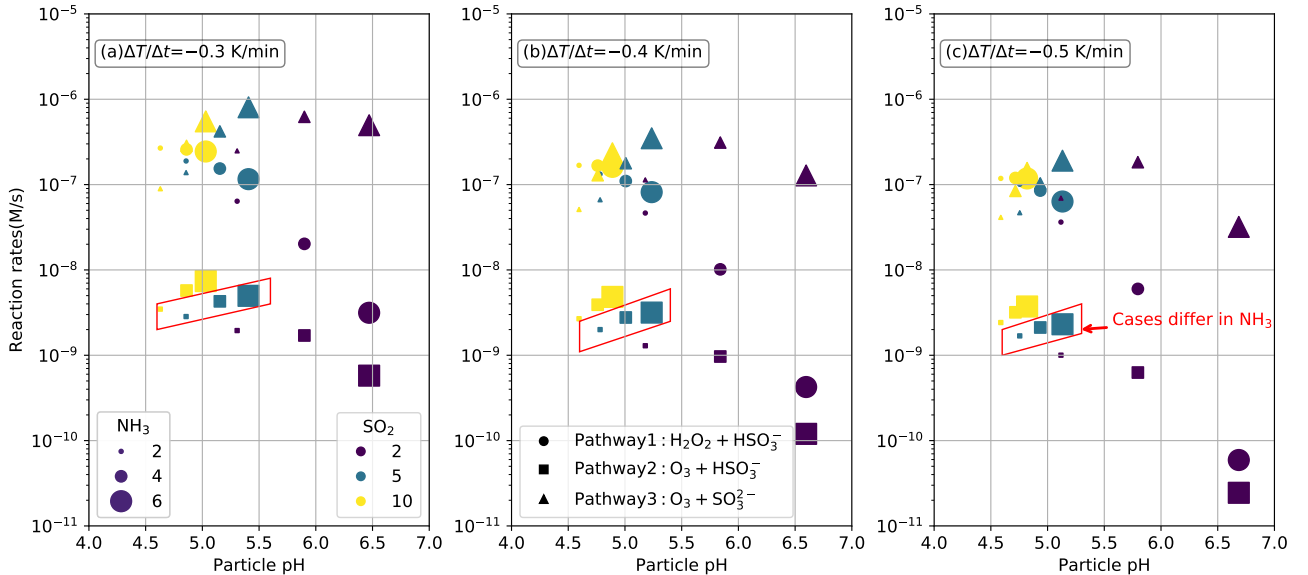


Figure 2.6: Relationship between aqueous sulfate formation rates and particle acidity at $t = 3$ min. (a) temperature lapse rate of -0.3 K/min. (b) temperature lapse rate of -0.4 K/min. (c) temperature lapse rate of -0.5 K/min. Symbol types are for different oxidation pathways: circle is for $\text{H}_2\text{O}_2 + \text{HSO}_3^-$, square is for $\text{O}_3 + \text{HSO}_3^-$ and triangle is for $\text{O}_3 + \text{SO}_3^{2-}$. Color is for $\text{SO}_2(\text{g})$ level and symbol size represents $\text{NH}_3(\text{g})$ level. All the cases in the figure are with $\text{O}_3(\text{g}) = 50$ ppb and $\text{H}_2\text{O}_2(\text{g}) = 0.5$ ppb. Red boxes are for the aerosol populations with only differences in $\text{NH}_3(\text{g})$ and are analyzed in more detail in the text.

2.5 Contribution of TMI pathways to sulfate formation

This section presents the 243 cases containing iron components in P_{TMI} and explore the contributions of TMI catalyzed reactions. Figure 2.7(a) shows the time series of Fe^{2+} , Fe^{3+} and $\text{OH}(\text{aq})$ median molar concentration.

Fe^{2+} varies between 10^{-11} and 10^{-7} and Fe^{3+} ranges between 10^{-7} and 10^{-6} M, both are in the same order with the values in Deguillaume et al. (2005). By adding TMI, the median sulfate mixing ratio in P_{TMI} significantly increased from 2 ppb to 5 ppb. Figure 2.8 further explores the contribution ratio changes of different aqueous sulfate pathways after adding TMI to the population.

Oxidation of HSO_3^- by O_3 and H_2O_2 are the dominant pathways for aqueous sulfate formation in P_{ref} (Fig. 2.8(a)). These two pathways in total contributed to more than 90% of sulfate formation over the simulation period, and there is no contribution of TMI pathways. But in P_{TMI} , these two pathways are dominant at the first 2 minutes and sulfate formation through the reaction between SO_4^- and water is dominant afterwards (Fig. 2.8(b)). I also noticed a remarkable contribution from TMI pathway after 4 min, and the contribution ratio can be more than 20% at the end of simulation.

It is worth a reminder that $\text{OH}(\text{g})$ was emitted at a constant rate for the cases P_{TMI} , while there was no emission of $\text{OH}(\text{g})$ in P_{ref} . Based on current simulation settings, we can not distinguish the role of OH and TMI for the increased sulfate production rates in P_{TMI} . However, we can still learn from the current result if conditions exist where sulfate

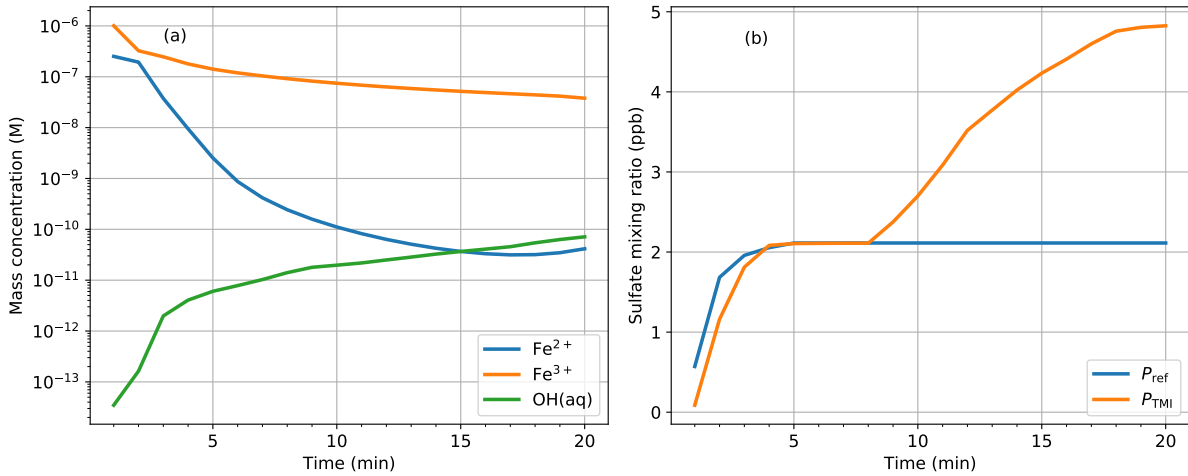


Figure 2.7: Time series of (a) Fe^{2+} , Fe^{3+} and $\text{OH}(\text{aq})$ (b) Sulfate mixing ratio in P_{ref} and P_{TMI} . Values are the median of all the cases in the ensemble P_{TMI} .

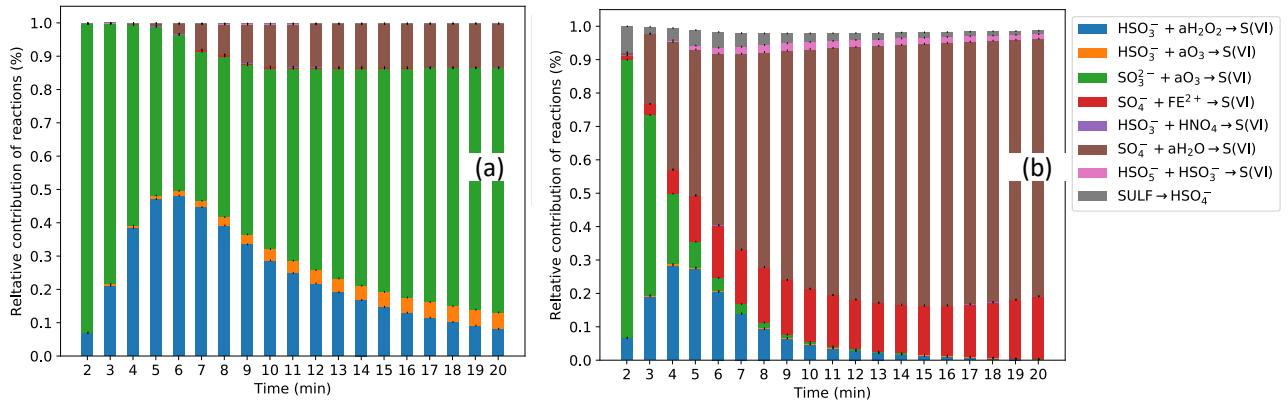


Figure 2.8: Mean contribution fraction of different sulfate formation pathways in (a) P_{ref} and (b) P_{TMI}

formation through TMI pathways can be important, and PartMC is able to capture this.

2.6 Conclusion

For the work presented in this chapter, we used the particle-resolved model PartMC as cloud parcel model with a comprehensive aqueous chemistry module CAPRAM2.4 to investigate the role of different aqueous sulfate formation pathways. The model was evaluated using results from size-resolved and bulk aqueous models from the literature, and our model reproduced similar $\text{SO}_2(\text{g})$ and acidity profiles.

We designed an ensemble of scenarios to investigate the response of sulfate formation to varying input parameters. As expected, cases with high $\text{NH}_3(\text{g})$ and $\text{SO}_2(\text{g})$ produced the most sulfate. This can be explained by efficient

oxidizing reactions between SO_3^{2-} and $\text{O}_3(\text{aq})$ because of the higher pH that exists when $\text{NH}_3(\text{g})$ is supplied. Our particle-resolved aqueous chemistry model reproduces the expected responses of O_3 and H_2O_2 pathways to pH. Analysis of another ensemble scenario with TMI present shows S(IV) reactions catalyzed by TMI can contribute up to 20% of the sulfate production, and the fraction was consistent with the values found by Alexander et al. (2009c).

The representation of TMI oxidation processes is rather simple in this current setup. Iron from different sources has different solubility (Desboeufs et al., 2005). It would be therefore better to connect the soluble fraction of iron to its sources to investigate the conditions most favorable for TMI-catalyzed reactions more realistically. Further, the need for “OH emissions” is an artefact of not having entrainment or gas-phase chemistry occurring when aqueous phase chemistry is simulated. If we had entrainment, then fresh OH may be supplied from outside the cloud, and similarly, if we had gas-phase chemistry enabled, OH may be produced in the gas phase and could partition with the aqueous phase. In future model development, both processes should be considered to be included.

Chapter 3

Evaluating the impacts of cloud processing on resuspended aerosol particles after cloud evaporation using a particle-resolved model

This chapter quantifies the changes of aerosol properties after cloud processing using the particle-resolved aqueous chemistry model. First I introduce model details, mixing state metrics and cloud parcel simulation design. Then, I present the changes in number and mass distribution changes after cloud processing. Finally, I discuss the changes in aerosol mixing state, CCN concentration and aerosol optical properties after cloud processing. The first part about cloud processing effects on aerosol mixing state is currently under review with *Journal of Geophysical Research-Atmosphere*, and the second part about the changes in aerosol optical values is in preparation for *Aerosol Science and Technology*.

3.1 Introduction

Atmospheric aerosol particles are complex mixtures of different chemical species reflecting the fact that they originate from different emission sources and experience various aging processes in the atmosphere (Riemer et al., 2009; Li et al., 2011; Bondy et al., 2018; Healy et al., 2014; Rissler et al., 2014). Aging processes include processes in the cloud-free atmosphere such as coagulation, heterogeneous reactions on the particles' surface, and the formation of coatings from organic and inorganic secondary aerosol. They also include processes in clouds (Lance et al., 2017) such as aqueous-phase chemistry within cloud droplets forming inorganic and organic aerosol material, and collision-coalescence of particles and droplets within a cloud. When clouds evaporate, aerosol populations are released into the atmosphere with modified properties compared to the populations that formed the cloud. This, in turn, changes the aerosols' impacts on clouds in the next cloud cycle (Hoose et al., 2008), and therefore this process is important for 3D chemical transport models to include. At the same time it poses challenges to be represented in chemical transport models (Gao et al., 2016).

Specifically, in-cloud processes have been shown to produce a double peaked size distributions since material from the gas phase and from smaller particles is transferred to the accumulation mode size range (Hoppel et al., 1986; Noble and Hudson, 2019). It has also been observed that cloud droplets of different sizes may differ in their acidity (Collett et al., 1994; Pye et al., 2020). This has important implications for the rates of aqueous-phase sulfate formation

(Hoag et al., 1999), which depends strongly on pH, and this needs to be considered when representing these processes in cloud microphysics models (Hegg and Larson, 1990; Barth, 2006a). Because of the non-linearity of aqueous chemistry processes, models predict larger rates of sulfate formation when using a more realistic size-resolved droplet representation compared to using a prescribed single droplet size.

In this study, we not only considered the variation of aerosol (and cloud droplet) composition with size, but also the variation of composition within a narrow size range, commonly referred to as mixing state (Winkler, 1973a; Riemer et al., 2019). Our goal in this study was to quantify the changes in aerosol mixing state due to in-cloud aqueous-phase chemistry and coagulation processes. Aerosol mixing state impacts the aerosols' effects on health (Ching and Kajino, 2018), their absorption and scattering of sunlight (Lesins et al., 2002; Fierce et al., 2020), and their ability to act as cloud condensation and ice nuclei (Broekhuizen et al., 2006b; Bhattu and Tripathi, 2015; Knopf et al., 2018).

Mixing state is, on the one hand, a factor in determining which particles activate and form cloud droplets, thereby determining cloud properties (Ching et al., 2012, 2016a). On the other hand, mixing state can be modified by in-cloud processes. For example, observations using online single-particle mass spectrometry during the HCCT-2010 field campaign showed that cloud residuals contain more sulfate and nitrate compared to the below-cloud aerosol (Roth et al., 2016), resulting in a change of aerosol mixing state.

Model simulations of aerosol mixing state are challenging, and particularly rare when it comes to simulating in-cloud processes due to the need for extensive computing resources. Regional or global models use simplified assumptions about aerosol activation and aerosol mass and size changes due to cloud processing, which are determined by the underlying model representation of aerosol and cloud droplets. For example, in the CMAQ model, which uses a modal aerosol representation, the sulfate mass produced by in-cloud chemistry is added to the entire accumulation mode (Ervens, 2015a; Fahey et al., 2017b). In the global climate model ECHAM5-HAM, activated particles are grouped into two bins, one with low ion concentration and the other with higher ion concentration (Roelofs et al., 2006) to capture the dependence of the sulfate formation pathway on pH.

High-resolution cloud models typically use a size-resolved fixed-bin microphysical model (Flossmann, 1994; Feingold et al., 1996) and resolve aerosol particles and cloud droplets by separate distributions, thus internally mixing all same-sized particles or droplets. Similarly, accurate parcel models most frequently use a size-resolved moving-bin approach (Kreidenweis et al., 2003a; Cooper et al., 1997), again losing aerosol history and composition information within each size bin. To preserve some composition information, 2D aerosol models have been used, resolving cloud droplet size and aerosol dry volume (Bott et al., 1996; Ovchinnikov and Easter, 2010). However, increasing the dimension beyond 2D to treat composition variation of the aerosol in more detail would be computationally prohibitively expensive. Lagrangian cloud microphysics models have also been developed that track information on a droplet level (Shima et al., 2009; Andrejczuk et al., 2008; Grabowski et al., 2019; Sölk and Kärcher, 2010; Unterstrasser and Sölk,

2014; Jaruga and Pawlowska, 2018). However, their focus has been the study of cloud microphysics rather than the modification of aerosol composition. While Jaruga and Pawlowska (2018) consider some aqueous-phase chemistry processes, their representation of the aerosol is comparatively simple and questions about mixing state have not yet been addressed.

For our study, we used the aerosol model PartMC-MOSAIC (Particle Monte Carlo-Model for Simulating Aerosol Interactions and Chemistry) (Riemer et al., 2009; Zaveri et al., 2008a) as aerosol and cloud parcel model. This stochastic particle-resolved model explicitly resolves the composition of individual aerosol particles and cloud droplets in a given population. Since individual particles and droplets are explicitly tracked, there is no need to invoke ad hoc aging criteria that move aerosol mass between bins or modes as is the case with traditional modal or sectional approaches (Riemer et al., 2003; Stier et al., 2005; Bauer et al., 2008; Jacobson, 2001). Tracking droplets explicitly is therefore a well-suited to simulate aerosol mixing state and investigate its impacts on climate-relevant aerosol properties.

The model was described in Ching et al. (2012) and Ching et al. (2016a) and has been used to simulate the mixing state evolution of black-carbon-containing aerosol in the cloud-free atmosphere, followed by a process analysis to what extent the aged aerosol is able to undergo nucleation-scavenging as the particles compete for water vapor in an updraft. However, these studies did not include the effects of aqueous-phase chemistry occurring within the cloud droplets. This is the motivation for this study, where we extended our modeling framework to include aqueous-phase chemistry within the cloud droplets that are forming on a diverse population of particles, common to urban environments. The contribution of this chapter is the first study to document quantitatively the impact of aqueous phase chemistry on mixing state.

We focused on the following questions: (1) To what extent does cloud processing change the aerosol mixing state of the population that entered the cloud? (2) How does this change the cloud condensation number concentration and aerosol optical properties? (3) What is the role of coagulation between the interstitial particles and cloud droplets for mixing state of the aerosol?

Chapter 3.2 describes the model components, the scenario setup, and the mixing state metrics used in this study. Chapter 3.3 presents the analysis of the simulation results. Chapter 3.4 summarizes our results.

3.2 Model description and metrics

3.2.1 Stochastic particle-resolved module PartMC-MOSAIC

Aerosol physical and chemical processes were simulated by the stochastic particle-resolved model PartMC-MOSAIC (Particle Monte Carlo-Model for Simulating Aerosol Interactions and Chemistry-Model for Simulating Aerosol In-

teractions and Chemistry, (Riemer et al., 2009; Zaveri et al., 2008a)). The PartMC model simulates the evolution of per-particle composition of a large ensemble of computational particles in a well-mixed computational volume. In contrast to Lagrangian droplet models that have become popular in the cloud microphysics community (Shima et al., 2009; Grabowski et al., 2019), PartMC-MOSAIC does not track the position of particles and droplets within the computational volume.

The particle number concentration changes due to coagulation, emission and dilution, which are simulated by using a stochastic Monte Carlo sampling method (Riemer et al., 2009). Gas-phase chemistry and gas-particle partitioning are represented by the aerosol chemistry model MOSAIC, which includes CBM-Z for gas-phase photochemical reactions (Zaveri, 1999), MTEM for estimating mean activity coefficient of an electrolyte in a inorganic multicomponent solution (Zaveri et al., 2005c) and MESA for intraparticle solid-liquid partitioning for inorganic aerosols (Zaveri et al., 2005a). The formation mechanism of secondary organic aerosol (SOA) in MOSAIC is based on SORGAM (Schell et al., 2001a) with several parameters adjusted to bring the simulated values closer to observation (Zaveri et al., 2010). The model represents key aerosol species including sulfate, nitrate, ammonium, black carbon (BC), primary organic aerosol (POA) and several surrogate secondary organic aerosol (SOA) species. The coupled model PartMC-MOSAIC was applied in previous studies for simulating aerosol optical and CCN properties, black carbon aging time-scales and the black carbon absorption enhancement due to the coatings (Zaveri et al., 2010; Riemer et al., 2010; Fierce et al., 2017, 2020), focusing on mixing state evolution during cloud-free conditions. The model was also used for evaluating the impact of aerosol mixing state on cloud droplet formation (Ching et al., 2012, 2016a), which will be explained in more detail in the next section.

3.2.2 Cloud parcel model and aqueous-phase chemistry

Ching et al. (2012) described the details of the particle-resolved cloud parcel model, which simulates a population of aerosol particles that experience cooling at a prescribed cooling rate and subsequent growth due to the condensation of water vapor. The condensational growth of the particles is calculated following Seinfeld et al. (2016a). The driving force of the growth is the difference between droplet equilibrium saturation vapor pressure and the ambient vapor pressure of the environment. The equilibrium saturation vapor pressure is calculated by Köhler theory, and the particle hygroscopicity is determined using the parameterization of aerosol hygroscopicity developed by Petters and Kreidenweis (2007). The hygroscopicity κ of each particle is calculated by using the volume-weighted average of the individual κ values of the particles' constituent species. We used κ of 0.65 for ammonium sulfate and ammonium nitrate, κ of 0.1 for SOA and κ of 0.001 for POA. BC is assumed to be hydrophobic and had κ of 0. The hygroscopicity of each particle varied as the chemical composition evolved for each particle. We currently do not represent any entrainment of cloud-free air into the cloud, surface tension effects on droplet growth, or the loss of droplets from the

air parcel owing to sedimentation.

The aim of this chapter is to investigate impacts of in-cloud aqueous-phase chemistry on aerosol mixing state. To this end, we coupled the reduced Chemical Aqueous Phase Radical Mechanism (CAPRAM) 2.4 to PartMC-MOSAIC. The reduced CAPRAM model includes 183 reactions (including Henry's Law partitioning, dissociation reactions, photolysis reactions and other aqueous-phase reactions) and 113 species (Herrmann et al., 1999; Ervens et al., 2003). The mechanism treats the reactions of common radicals and radical anions, transition metal ions and organics with less than two carbon atoms. The CAPRAM mechanism was applied to simulate the cloud processes for the FEBUKO field campaign and reproduced the aqueous sulfate and organic compounds oxidation processes well (Tilgner et al., 2005; Wolke et al., 2005b). While the aqueous-phase chemistry involving transition metal ions and organic species is of great interest (Mayol-Bracero et al., 2002; Harris et al., 2013a; Alexander et al., 2009b; Lian et al., 2019; McNeill, 2015a; Smith et al., 2014a; Wonaschuetz et al., 2012; Wagner et al., 2015), our scope for this initial study is the in-cloud production of sulfate and nitrate and their relationship to changes in aerosol mixing state. We did not consider the co-condensation of nitric acid gas due to vapor pressure difference discussed by Crooks et al. (2018). A subset of the most relevant Henry's law, aqueous equilibria and chemistry reactions are summarized in Table S1.

The original gas-phase chemistry mechanism Regional Atmospheric Chemistry Modeling (RACM) used in CAPRAM 2.4 was replaced with CBM-Z, which is the gas-phase mechanism native to PartMC-MOSAIC. In the current setting, aqueous chemistry, and the evaporation and condensation of gases (other than water vapor) to aqueous particles are enabled for particles with liquid water mass larger than 5×10^{-16} kg, which corresponds to solution droplets of 1 μm in diameter.

We used the CVODE (Cohen et al., 1996) solver of the SUNDIALS (Hindmarsh et al., 2005) package to solve the mass transfer and aqueous chemistry of the CAPRAM 2.4 reduced mechanism with the Backward Differentiation Formulas (BDF) and Newton Iteration, which is suitable for mathematically stiff systems, such as those treating multi-phase chemistry. To reduce the stiffness of the system, the Henry's Law partitioning of the strong acids H_2SO_4 , HCl , and HNO_3 were combined with their first acid dissociation step.

3.2.3 The scenario settings

The scenario setting of this work followed the two-step method used in Ching et al. (2012). Step 1 represented the simulation of an "urban plume scenario" in a subsaturated ($\text{RH} < 100\%$) environment using PartMC-MOSAIC. The purpose of this step was to generate aerosol populations that cover a wide range of mixing states, which can later serve as input populations for our cloud parcel simulations. The urban plume simulation had a simulation time of 24 h, and the state of the aerosol and gas phase were saved hourly. This hourly output was then used as inputs for 25 separate 30-min particle-resolved cloud parcel simulations (Step 2). Each of the 25 cloud parcel simulations was exposed to

the same cooling rate but differed in their initial conditions of aerosol populations and gas-phase concentrations.

The urban plume case environment shown here was adopted from (Zaveri et al., 2010), following a Lagrangian box modeling approach, where we assumed that the air parcel containing background air moved over a polluted urban environment. We refer to this case for the remainder of the chapter as the “high-emission” case. The initial condition of the aerosol consisted of two lognormal modes, with the number concentration, geometric mean diameter, standard deviation and composition for each mode as listed in Table 3.1. We used 10,000 computational particles to resolve the initial aerosol. Note that the number of computational particles changed over the course of the simulation depending on coagulation, particle emissions, and dilution with the background, but was kept between half and double the initial number of computational particles using doubling and halving procedures as described in Riemer et al. (2009).

Table 3.1: Size distributions and compositions of initial, background and emitted aerosols for the high-emission case.

Initial/Background	N (cm^{-3})	D_g (μm)	σ_g	Composition by mass	D_i^{**}
Aitken mode	1800	0.02	1.45	49.6% $(\text{NH}_4)_2\text{SO}_4$ + 49.6% API1* + 0.8% BC	2.08
Accumulation mode	1500	0.116	1.65	49.6% $(\text{NH}_4)_2\text{SO}_4$ + 49.6% API1 + 0.8% BC	2.08
Emission	E ($\text{m}^{-2}\text{s}^{-1}$)	D_g (μm)	σ_g	Composition by mass	D_i
Cooking	9×10^6	0.086	1.91	100% POA	1
Diesel	1.6×10^8	0.05	1.74	70% BC + 30% POA	1.84
Gasoline	5×10^7	0.05	1.74	20% BC + 80% POA	1.65

*: Low volatility secondary aerosol product from the oxidation of α -pinene.

**: Per-particle diversity, refer to Sec. 3.2.4 for a detailed description.

Gas-phase initial conditions were set to 50 pbb ozone and low levels of other trace gases. The plume was diluted with background air at a rate of $1.5 \times 10^{-5} \text{ s}^{-1}$ that contained the same gas mixing ratios and aerosol concentrations as the initial condition. The simulation started at 6 AM local time and lasted for 24 h with gas and aerosol emission entering the simulation during the first 12 h. We use the term “plume time”, t_u , to refer to the elapsed time during this 24-h simulation in cloud-free conditions. The temperature was prescribed as shown in Figure 3.1. For simplicity we assumed that the temperature remained constant after the first 6 h. This is consistent with the air parcel staying in the fully mature mixed layer until sunset and in the residual layer thereafter (Zaveri et al., 2010). The resulting relative humidity varied between 52% and 95%, assuming that the total water content in the air parcel was constant.

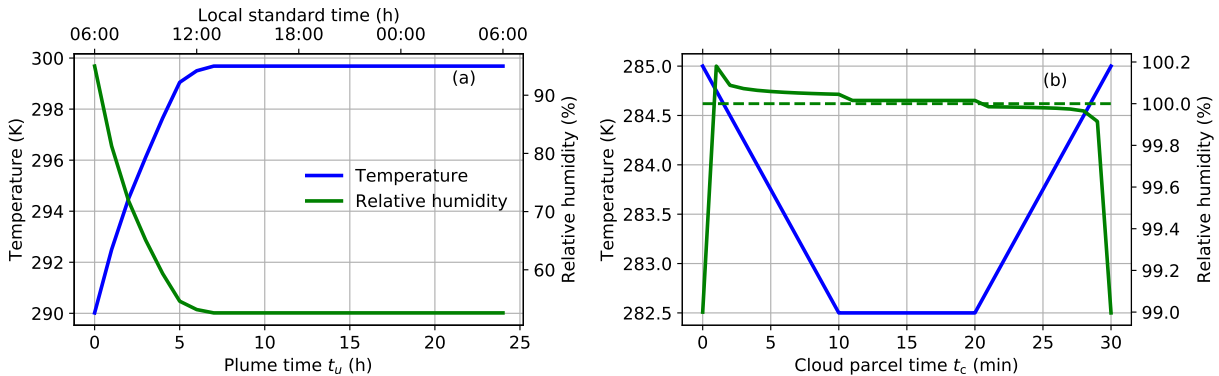


Figure 3.1: Temperature and relativity humidity time series in (a) urban plume environment and (b) cloud parcel environment. The green dashed line in (b) is RH = 100%.

Aerosol emission sources and their compositions are also listed in Table 3.1. Note that the composition of aerosol emissions from gasoline vehicles was based on Somers (2004) and Nam (2008). Current gasoline vehicles produce tailpipe emissions with higher BC content (Liggio et al., 2012). However, since both BC and POA have very low hygroscopicities ($\kappa = 0$ for BC and 0.001 for POA), we do not expect that the exact BC/POA split impacted our results for this chapter (however this will be important for optical properties).

The mixing state of the aerosol in this simulation evolved because primary aerosol emissions aged owing to formation of secondary aerosol and to coagulation processes, while fresh emissions continued to enter during the first 12 hours of simulation. Overall, this scenario mimicked the evolution of an air parcel in a polluted urban area, and we summarized the results, including the mixing state evolution, in Chapter 3.3.1. The full state, including gas-phase mixing ratios and composition of all computational particles, was saved hourly to be used as input for the cloud parcel simulations in step 2.

In addition to the high-emission urban plume case described above, we performed a second simulation with reduced initial aerosol number concentration and aerosol emissions (5% of the high-emission case) and gas emissions (15% of the high-emission case) to represent a less polluted urban environment. We refer to this case as the “low-emission case”. Scale parameters relative to the high-emission case are summarized in Table 3.2.

Table 3.2: Scale parameters of gas emission rates, initial and background particle number concentration and aerosol number fluxes emission rates used for low-emission cases (relative to high-emission case)

Gas emission rates	Initial/background number conc.		Aerosol emission rates		
	Aitken	Accumulation	Cooking	Diesel	Gasoline
Scale parameters	15%	5%	5%	5%	5%

For step 2, the hourly output of the simulated aerosol and gas-phase mixing ratios was used as input for the cloud parcel simulations, using a prescribed cooling rate. The temperature decreased for the first 10 minutes at a rate of 0.25 K min^{-1} , which corresponds to an updraft velocity of approximately 1 m s^{-1} . The value is calculated by using equation (17.56) in Seinfeld and Pandis (2006) without consideration of entrainment. The cooling rate was kept constant for the next 10 minutes, and increased at the rate of 0.25 K min^{-1} for the last 10 minutes. Hence one cloud cycle consisted of a total of 30 minutes, and we referred to the elapsed time within the cloud cycle as “cloud parcel time”, t_c . The initial RH for the cloud parcel was 99 %, and it reached supersaturation within less than 1 min. The parcel became subsaturated when the cloud began to evaporate at 20 min, and returned to RH=99% at the end of the simulation.

Since it is common for air parcels to undergo several cloud cycles (Barth et al., 2003), we conducted a total of four cloud cycles for the high-emission case, which resulted in a total of $25 \times 4 = 100$ cloud parcel simulations. We initialized the aerosol for the second, third and fourth cloud cycles using the particle population from the end of the previous cloud cycle. For the gas-phase mixing ratios we always used the values from the beginning of the first cloud cycle. That is, in choosing this setup, we explored how an already processed aerosol population changes further when it is exposed to a given gas environment and cooling rate (especially focusing on changes in the mixing state) with the only difference between cloud cycles being the input aerosol population. We realize that this is an idealized setup since in reality the gas phase concentrations are likely not the same for subsequent cloud cycles. For the low-emission case, we only present the results for one cloud cycle.

Lastly, to explore the effects of coagulation, we performed another set of cloud parcel simulations that included Brownian coagulation, using the high-emission case as input. For most of our analysis, we focus on the difference between the particles at the start of the cloud parcel simulations and the end of the cloud parcel simulation, after cloud evaporation.

3.2.4 Mixing state metrics

The objective of this chapter is to quantify the change of particle mixing state as a result of cloud processing. The metrics used to quantify mixing state were developed by Riemer and West (2013). The mixing state metric χ is calculated by:

$$\chi = \frac{D_\alpha - 1}{D_\gamma - 1}, \quad (3.1)$$

where D_α is the average particle diversity and D_γ is the bulk particle diversity.

The calculation of these diversity metrics is based on the per-particle mixing entropy H_i . For an aerosol population

of N particles containing A species, the mixing entropy H_i and particle diversity D_i of particle i are calculated as

$$H_i = \sum_{a=1}^A -p_i^a \ln p_i^a \quad D_i = e^{H_i}, \quad (3.2)$$

where p_i^a is the mass fraction of species a in particle i . Expanding D_i to the whole population, D_α and D_γ are defined as

$$H_\alpha = \sum_{i=1}^N p_i H_i \quad D_\alpha = e^{H_\alpha}, \quad (3.3)$$

$$H_\gamma = \sum_{a=1}^A -p_a H_i \quad D_\gamma = e^{H_\gamma}, \quad (3.4)$$

where p_i and p_a are the mass fractions of particle i and species a in the population. For externally mixed populations where particles contain only one species, $D_\alpha = 1$ and $\chi = 0\%$. For internally mixed population where each particle has the same composition as the bulk, $D_\alpha = D_\gamma$ and $\chi = 100\%$. In the ambient atmosphere, aerosols are neither completely internally nor externally mixed and intermediate mixing states are common (Healy et al., 2014; Ye et al., 2018; Ching et al., 2019). For regions close to emission sources, χ is expected to be lower, while χ is larger in air masses dominated by an aged aerosol.

The mixing state metrics χ defined in this chapter used the abundance of model chemical species as the basis for calculating particle mass fractions in Equations (3.2)–(3.4), i.e. sulfate, nitrate, ammonium, POA, etc., excluding aerosol water. Other choices for defining “species” are possible, for example Ching et al. (2017) used two surrogate species, hygroscopic and non-hygroscopic species, as the basis for χ . Furthermore, Zheng et al. (2021a) compared χ based on the mixing of model chemical species, of hygroscopic and non-hygroscopic species, and of absorbing and non-absorbing species.

3.3 Simulation results

3.3.1 Urban plume simulation with PartMC-MOSAIC

This section summarizes the results from the urban plume simulations to provide context for the cloud parcel simulations discussed in the remainder of the chapter. Figure 3.2 shows selected quantities from the high-emission urban plume simulation. The total particle number concentration N_a increased initially due to the emission of primary particles, reached a maximum of $15,295 \text{ cm}^{-3}$ at $t_p = 12 \text{ h}$, then decreased because the emissions ceased, and both dilution and coagulation reduced the particle number concentration. Similarly, BC and POA mass concentrations increased for the first 12 h due to emission, and decreased thereafter due to dilution with the background, just as Figure 3.2b shows.

The time series of the secondary aerosol species sulfate and SOA were determined by the interplay of loss by dilution and photochemical production. The ammonium nitrate mass concentration was determined by the gas concentrations of its precursors, HNO_3 and NH_3 , temperature and RH. Mixing ratios of SO_2 , O_3 and H_2O_2 are shown in Figure 3.2c for reference because they are directly involved in the in-cloud sulfate formation as discussed in Chapter 3.3.2.

Figure 3.2b only displays the bulk composition of the aerosol, while the mixing state information available from the particle-resolved output remains hidden. Figure 3.2d provides insight into the evolution of aerosol mixing state as quantified by the mixing state metrics introduced in Chapter 3.2.4. At $t_u = 0$, the particle population was completely internally mixed, and therefore the mixing state index χ was initially 100%.

From Equation 3.1, we recall that χ is determined by the ratio of D_α and D_γ . Figure 3.2d indicates that both D_α and D_γ started out low, which is consistent with the aerosol initially only containing a small number of species, both on a per-particle level and on a population level, see Table 3.1. Over the course of the simulation, both D_α and D_γ increased, but at different rates, which led to changes in χ that we can interpret as changes in mixing state. The initial decrease in χ to about 50% was caused by the emission of fresh combustion particles, containing BC and POA. These emissions continued for the first 12 h of simulation, but at the same time coagulation and secondary aerosol formation occurred, which (at least initially) efficiently increased the average per-particle diversity D_α . Overall, this led to a more internally mixed population, with χ increasing to 72% at 10 h. After this, dilution became relatively more important, introducing background particles, and ammonium nitrate evaporated almost entirely towards the end of the simulation. These combined processes resulted in a slow decrease in χ to 64% at the end of simulation.

The corresponding figure for the low-emission case is shown as Figure 3.3. As expected, for this case, the aerosol number and mass concentrations and the gas-phase concentrations were reduced compared to the high-emission case. For example, the maximum aerosol number concentration at $t = 12$ h only reached to about 1000 cm^{-3} and the maximum SO_2 mixing ratio was only 1.2 ppb. The mixing state metrics (Figure 3.3d) ranged between 40% and 78%.

3.3.2 Aerosol composition changes during cloud processing

As described in Chapter 3.3.1, for each hourly output from the urban plume simulations, cloud cycles were simulated using the same temperature profile, shown in Figure 3.1b. Each cloud parcel simulation was exposed to the same cooling rate but differed in their initial conditions of aerosol populations and gas-phase concentrations. Figure 3.4 compiles the initial conditions of selected gas-phase species for the cloud parcel simulations using the high-emission case. Each color marks a specific cloud parcel case, which corresponds to a specific plume time t_u . The ranges were consistent with conditions found in polluted urban regions, such as Haikou in southern China, with annual average mixing ratios of 2 ppb SO_2 and 7 ppb NO_2 (Wang et al., 2014), and Kanpur in Northern India, with annual average mixing ratios of 3 ppb SO_2 and 5.7 ppb NO_2 (Gaur et al., 2014). In this section, we first illustrate the compositional

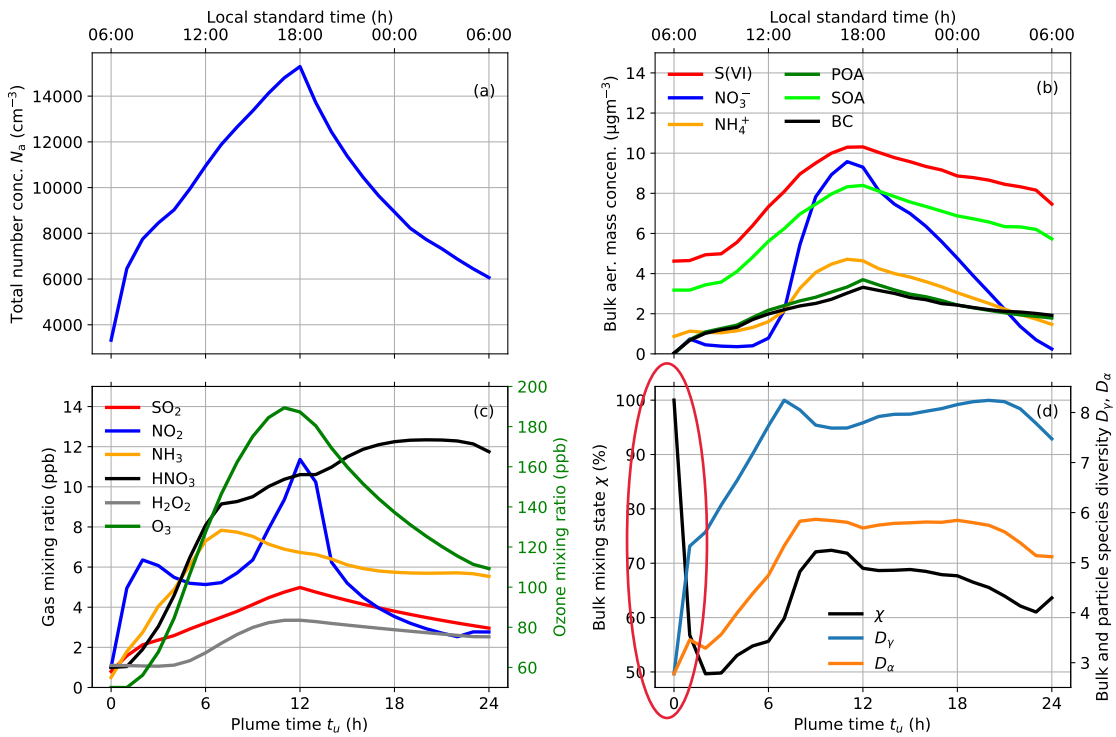


Figure 3.2: Temporal variation of (a) total number concentration, (b) mass concentrations of selected aerosol species, (c) mixing ratios of selected gas-phase species and (d) aerosol mixing state metrics for the high-emission case.

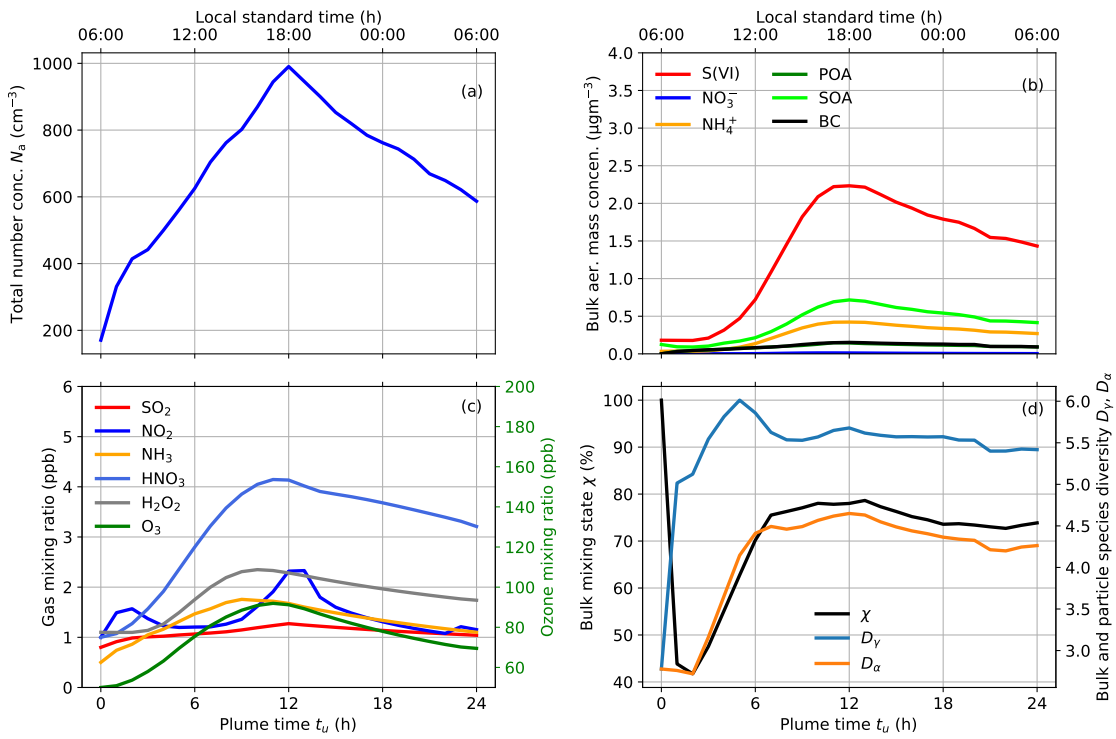


Figure 3.3: Temporal variation of (a) total number concentration, (b) mass concentrations of selected aerosol species, (c) mixing ratios of selected gas-phase species and (d) aerosol mixing state metrics for the low-emission case.

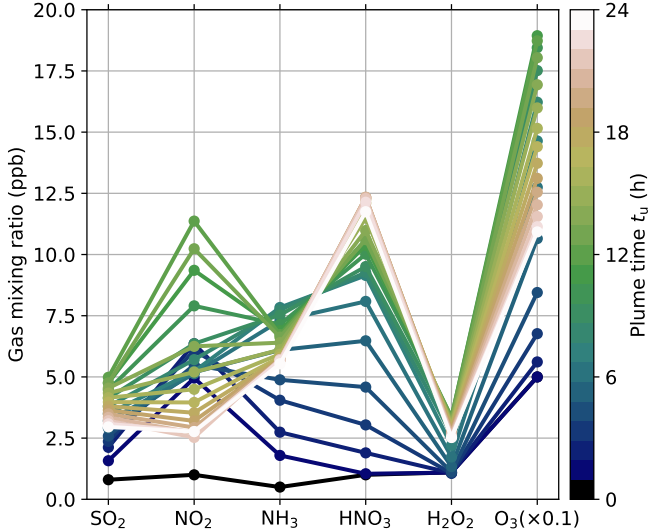


Figure 3.4: Initial conditions for selected gas-phase species for the cloud parcel simulations (high-emission case). Colors indicate the different plume hours. Note that the mixing ratio for O_3 is multiplied by 0.1 to be able to use the same scale on the ordinate as for the other gases.

changes during cloud processing, using the aerosol population from the high-emission case at $t_u = 12$ h as the initial conditions for the cloud parcel simulation, and focus on the first cloud cycle ($N_{\text{cycle}} = 1$).

Figure 3.5a shows the evolution of several key variables for this case. The initial RH for each cloud parcel simulation was 99%, and the aerosol water content of each particle was adjusted for RH=99% based on the dry aerosol composition. The parcel reached supersaturation within 1 min. During the first 10 min the liquid water content increased and reached a maximum of 1.23 g kg^{-1} at 10 min. We determined the cloud droplet number concentration following the strategy used in Ching et al. (2012), where particles with wet diameter larger than $2 \mu\text{m}$ were classified as cloud droplets. As shown in the figure, the cloud droplet number concentration (CDNC) was 2011 cm^{-3} at the time when the maximum supersaturation was reached. This number concentration decreased somewhat as the relative humidity slowly relaxed to saturation, which can be explained by the so-called “inertial effect” (Chuang et al., 1997; Nenes et al., 2001). This refers to droplets with diameter larger than $2 \mu\text{m}$ that were not truly activated, i.e., they had a critical diameter larger than $2 \mu\text{m}$ and this critical diameter was not reached during the simulation time. After 20 min, as the RH dropped below 100%, the cloud droplet number concentration declined faster and the cloud evaporated.

The CDNC is comparatively high for the example shown in Figure 3.5, since we started out with a large aerosol number concentration of over $15,000 \text{ cm}^{-3}$. CDNC of this magnitude were observed, for example, during the IMPACT field campaign (Brenguier et al., 2011). Using aerosols from other plume hours as inputs yielded CDNC below 2000 cm^{-3} , as shown in Figure 3.6 (but always larger than 1000 cm^{-3}). For the low-emission case, the CDNC were much lower, between 100 and 640 cm^{-3} , consistent with observations in more moderately polluted urban environ-

ments (Ahmad et al., 2013).

Figure 3.5b and Figure 3.5c show the evolution of several key gas and aqueous-phase species. Ammonia in the gas-phase dissolved and immediately formed ammonium. Aqueous-phase NH_4^+ increased from 4.7 to $9.8 \mu\text{g m}^{-3}$. Nitrate increased rapidly from 9.3 to $37.4 \mu\text{g m}^{-3}$ at the beginning due to the uptake of HNO_3 . These processes are explained by the R1-R10 reactions in Table S1. After this, nitrate was further formed through reaction R15.

The dissolved sulfur dioxide formed SO_3^{2-} and HSO_3^- , and could be oxidized to sulfate by aqueous-phase H_2O_2 or O_3 through R11-R15. The sulfate aqueous formation rates are highly pH-dependent, and the H_2O_2 oxidation reaction R13 is dominant for pH lower than 5, while the O_3 pathway R12 becomes more important for pH higher than 6 (Seinfeld et al., 2016a; Shao et al., 2019a). For the cases shown here, the cloud droplets were acidic, and therefore the oxidation by H_2O_2 dominated. Sulfur dioxide in the gas-phase decreased from 4.98 to 1.94 ppb, and the S(VI), including SO_4^{2-} and HSO_4^- , increased from 5.16 to $20.23 \mu\text{g m}^{-3}$ during the simulation period.

The evolution of the number size distributions based on wet diameter is illustrated in Figure 3.5d. At $t_c = 0$, the size distribution peaked at $0.3 \mu\text{m}$. As discussed above, in less than 1 min, a subset of the particles activated to form cloud droplets and the particle size distribution evolved from initially unimodal to bimodal, with the first peak representing the interstitial (not activated) particles and the second peak representing the cloud droplets. The interstitial aerosol remained unchanged since this simulation did not include coagulation. We will investigate the impact of coagulation further in Chapter 3.3.4. With increasing liquid water content and aqueous chemistry processes occurring, the cloud droplets continued to grow and the droplet mode peaked at $11 \mu\text{m}$ at 20 min.

Next, we will turn to the changes in aerosol size distributions. To provide a summary of the 25 individual cloud parcel simulations, we show here the average over all 25 scenarios with the variability amongst cases indicated by the standard deviation (colored band). Figure 3.7 shows the number and mass concentration as a function of dry diameter before entering the cloud and after each cloud cycle for the high-emission case. After the first cloud cycle, a second mode appeared for the dry number distribution, transforming the unimodal number distribution that peaked at a dry diameter of $0.1 \mu\text{m}$ to a bimodal distribution with a second peak at $0.3 \mu\text{m}$. For each additional cloud cycle, the peak of the second mode kept moving to larger diameters and reached $0.5 \mu\text{m}$ after the fourth cloud cycle.

The number size distribution of the cloud droplet residuals peaked at a dry diameter of $0.3 \mu\text{m}$ after the first cloud cycle, which is consistent with field observations (Fast et al., 2019; Ditas et al., 2012; Ge et al., 2012). For subsequent cloud cycles, the diameters increased further, because each cycle added more secondary aerosol mass on the already cloud-processed particles. This may not be representative for real clouds, where particle growth may be limited by gas precursors or oxidants and where entrainment occurs. However, cloud droplet residuals as large as $1 \mu\text{m}$ aerodynamic diameter were observed for particles collected at a mountain site in Southern China (Lin et al., 2017).

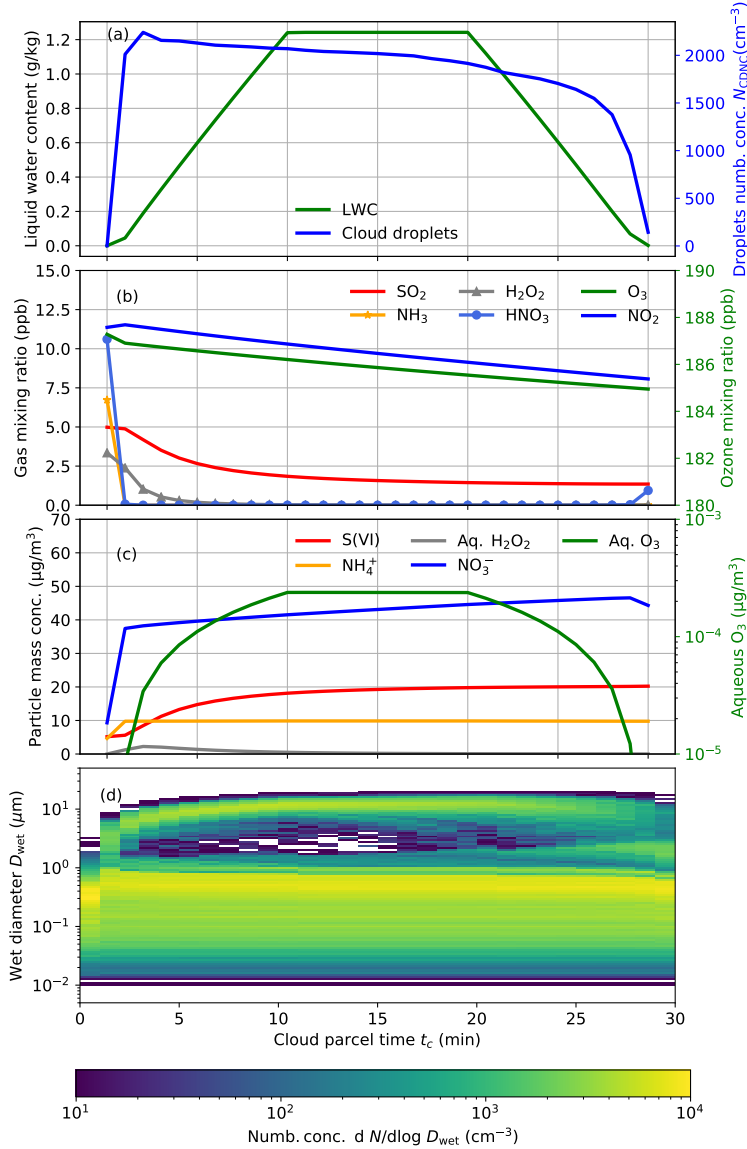


Figure 3.5: The evolution of (a) liquid water content (LWC) and cloud droplet number concentration (b) mixing ratios of key gas-phase species (c) key aqueous-phase species and (d) number concentration with respect to wet diameter. Results are for the aerosol population at $t_u = 12$ h (high-emission case) and for $N_{\text{cycle}} = 1$.

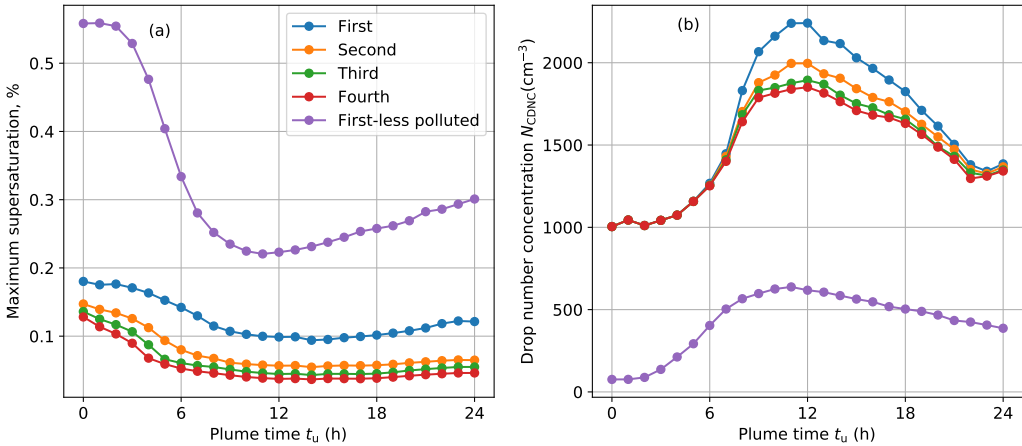


Figure 3.6: (a) Maximum supersaturation reached in the cloud parcel and (b) cloud droplet number concentration in the four cycles.

In order to quantify the diameter changes, we define the mean diameter \bar{D} as

$$\bar{D} = \frac{\sum_{i=1}^n N_i D_i}{N_{\text{total}}}, \quad (3.5)$$

where i is the particle index, n is the total number of computational particles, N_{total} is the total number concentration, N_i and D_i are the number concentration and diameter of computation particle i . The increase in diameter was largest for the first cycle, where \bar{D} increased 24% and grew from 0.1 to $0.124 \mu\text{m}$. The fourth cycle only led to a 5% mean diameter increase. For the mass, as shown in Figure 3.7b, distributions are dominated by the larger particles, as expected. Similar to the trend seen in the number size distribution, the mass increased most in the first cycle. The dry mass concentration, averaged over all 25 cases, increased from 21.2 to $67.2 \mu\text{g cm}^{-3}$ in the first cycle, which corresponds to 217%. After the fourth cycle, the mass increased from 110.4 to $152.8 \mu\text{g cm}^{-3}$ (38%).

The size distributions for the low-emission case are shown in Figure 3.8. The average mode diameter of the cloud droplet mode after the first cycle is somewhat larger ($\sim 0.35 \mu\text{m}$) than in the high-emission case even though the gas-phase precursor concentrations were lower. This can be explained by the fact that the CDNC was substantially lower than in the high-emission case, and the gas-phase concentrations were still high enough to allow more secondary aerosol mass to form per droplet.

Figure 3.9 shows the size-resolved mass fractions averaged over the 25 cases for each cloud simulation at the beginning of the first cloud cycle (grey) and at the end of the fourth cloud cycle (RH=99%) in high-emission cases. As expected, no change in the size-resolved composition occurred for particles smaller than about $0.1 \mu\text{m}$, as these particles remained interstitial aerosol. For the activated particles, the sulfate mass fraction increased from 9.6% to 38.7% in the size range of $0.14\text{--}0.25 \mu\text{m}$, and the nitrate mass fraction increased from 2.8% to 56.8% in the size range

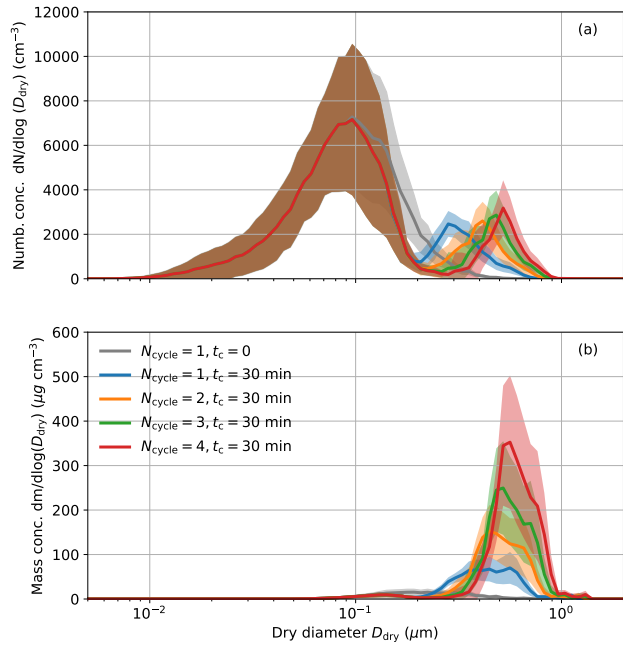


Figure 3.7: (a) Number and (b) mass size distribution with respect to dry diameter before the first cloud cycle and after each subsequent cloud cycle (high-emission case). The solid lines are the averaged distributions of all 25 cases for each cloud cycle. The shaded area represents the 1σ region of the average. The grey line is the distribution at $t_c = 0$ min, and the other lines are the distributions at the end of each cloud cycle. The composition of the particles was evaluated at RH = 99%. The brown shading in (a) is due to the overlapping colors of different cycles.

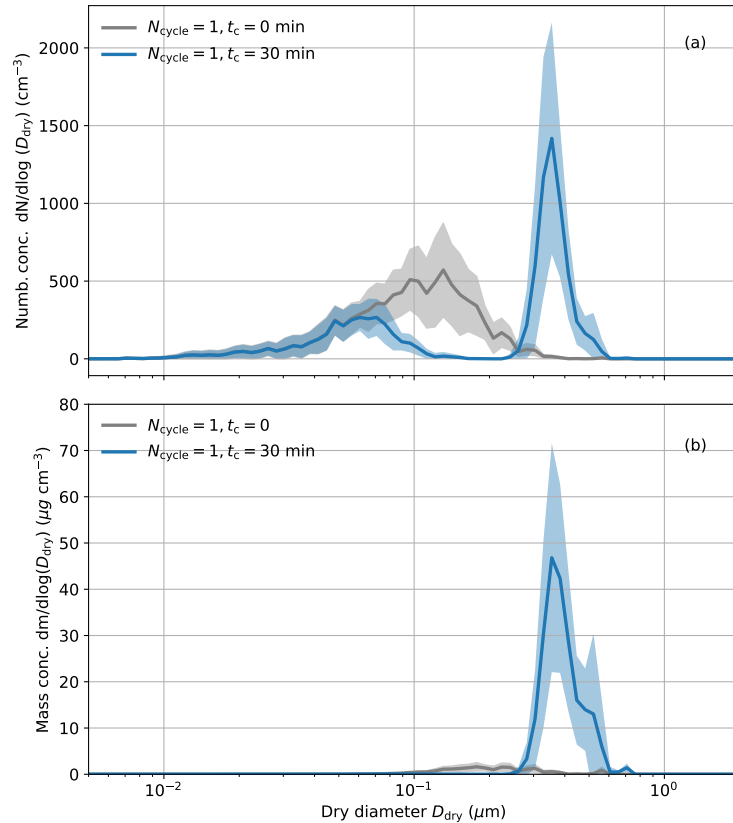


Figure 3.8: (a) Number and (b) mass size distribution with respect to dry diameter before (grey) and after (blue) the first cloud cycle for the low-emission case. The solid lines are the averaged distributions of all 25 cases for each cloud cycle. The shaded area represents the 1σ region of the average. The distributions at the end of each cycle. The composition of the particles was evaluated at RH = 99%.

of 0.21–0.89 μm . Ge et al. (2012) also found that particles were more enriched with nitrate and sulfate after aqueous processing from samples collected from Central Valley of California. For the particles in size range of 0.1–0.2 μm , the fraction of inorganic and SOA species decreased and the fraction of POA and BC species increased after cloud processing. This can be explained by the fact that there were two groups of particles in this size range, one group with mainly inorganic species and SOA, and the other group with mainly BC and POA. Particles in the first group were activated and grew larger due to cloud processing. Because more ammonium sulfate and nitrate was produced than SOA, the fraction of inorganics increased more than the SOA fraction. As a result, in the size range of 0.7–0.9 μm , particles transferred from organics-dominant to inorganics-dominant. The reduced SOA mass fraction in this size range can also be explained by the simplified aqueous SOA formation mechanism in the current study, which for example does not include the formation of IEPOX-derived organosulfates that have shown to be important in the ambient atmosphere (Hatch et al., 2011). In summary, even in the same size ranges (here 0.1–0.2 μm), particles with different compositions can evolve differently. This is challenging to resolve for models that represent composition with one-dimensional distributions, assuming internally mixed particles within one size bin, and further work is needed to investigate the bias that may be introduced by this assumption.

For our current work, the cloud simulations were set up using the temperature profile shown in figure 3.1b. Specifically, we considered a cloud that was maintained for about 30 min. In the real environment, clouds may last from minutes to days, depending on cloud type and the surrounding environment (Cotton et al., 2010), and they may also experience a range of different updraft velocities. Since the largest rate of secondary mass formation occurred within a few minutes after the cloud formed, shortening the cloud parcel time did not impact the conclusions as long as the first few minutes were captured. With longer cloud lifetime, secondary aerosol mass formation may continue, provided that the reactants are not depleted. Variations in updraft velocities/cooling rates will result in different maximum supersaturations, and hence differences in the subpopulations of activated particles. We did not explore these sensitivities here to keep the scope focused on the changes of particle populations after typical but complete cloud processes.

The previous analyses showed the size-resolved state of the aerosol. However, even within a certain size range, particles can exhibit differences in composition, and we introduced this earlier as the aerosol mixing state. With our particle-resolved modeling approach, we are able to resolve this detail and quantify how aerosol mixing state changes with cloud processing. In order to visualize the change in aerosol mixing state, Figure 3.10 displays the two-dimensional size distribution of sulfate mass fraction $n(D_{\text{dry}}, w_{\text{SO}_4})$ for the example of two plume hours $t_u = 0$ and $t_u = 12 \text{ h}$, before entering the cloud simulation and after four cloud cycles. At the beginning of the urban plume simulation ($t_u = 0 \text{ min}$), all particles had the same composition, and $n(D_{\text{dry}}, w_{\text{SO}_4})$ was 36% across the entire population (Figure 3.10a). Over the course of the urban plume simulation, $n(D_{\text{dry}}, w_{\text{SO}_4})$ was controlled by condensation, coagulation and dilution processes, and it became more diverse as shown in Figure 3.10b. The aerosol

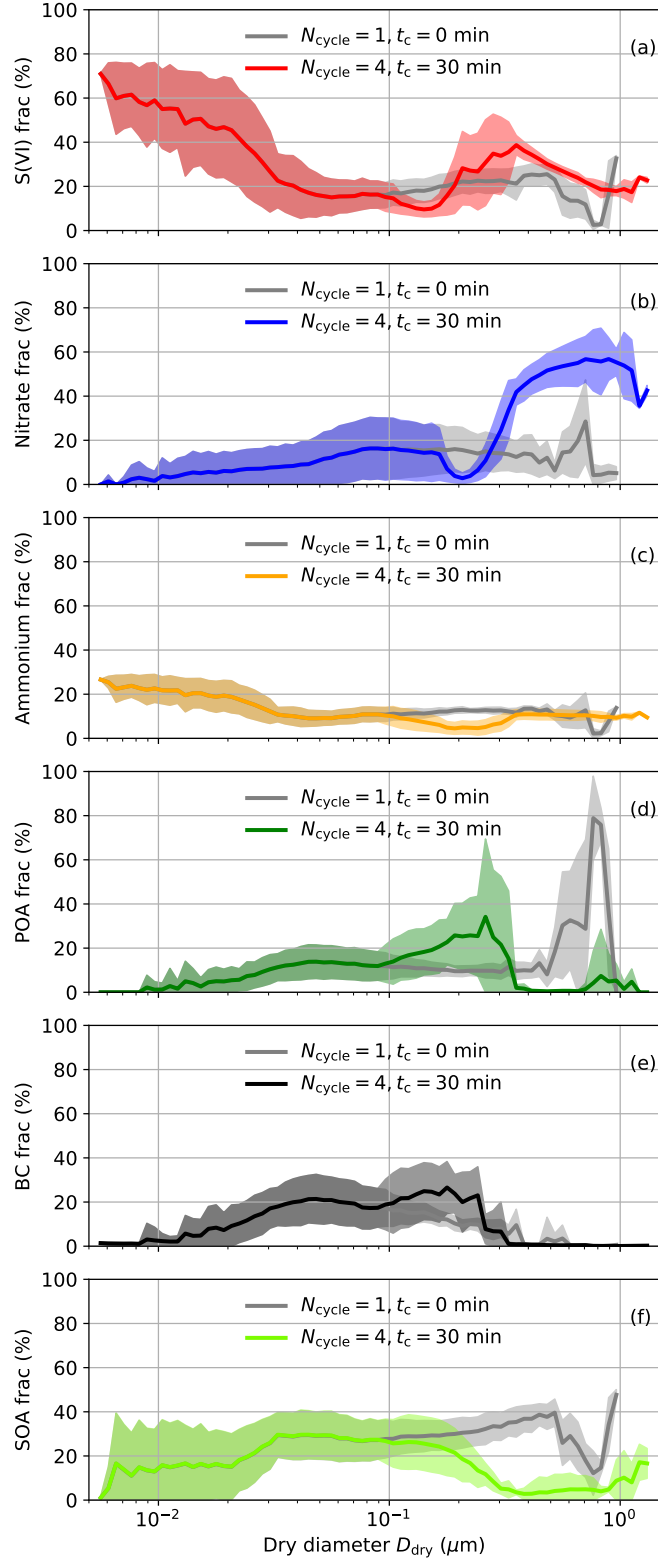


Figure 3.9: Size-resolved mass fractions of (a) S(VI), (b) nitrate, (c) ammonium, (d) POA, (e) BC and (f) SOA at $t_c = 0 \text{ min}$ of the first cloud cycle (grey lines), and $t_c = 30 \text{ min}$ after the fourth cloud cycle (colored lines) for the high-emission case. Solid lines are the average values of all 25 cases for each cycle and the shaded band represents the range of one standard deviation. The composition was evaluated at RH = 99%.

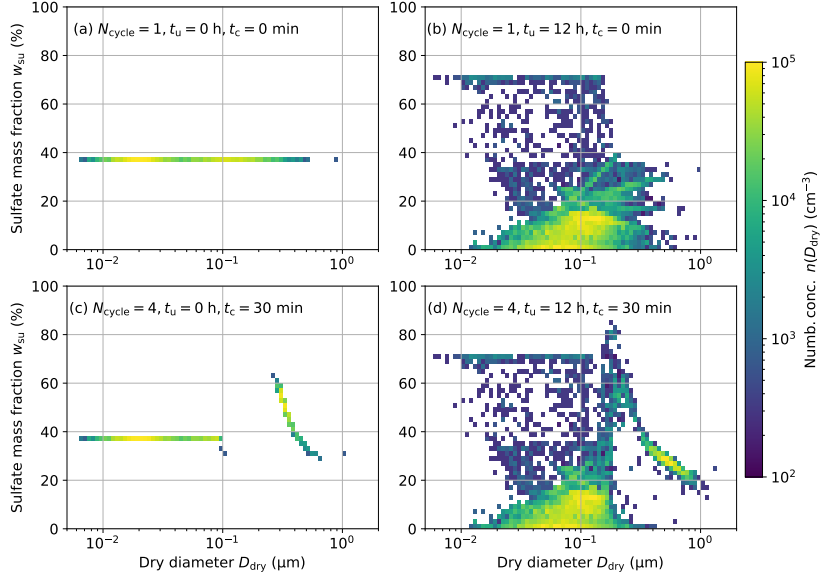


Figure 3.10: Two-dimensional number concentration distribution $n(D_p, w_{SO_4})$ before cloud processing for (a) $t_u = 0$ h and (b) $t_u = 12$ h (high-emission case), (c) population from (a) after four cloud cycles, (d) population from (b) after four cloud cycles.

primary emissions consisted of BC- and POA-containing particles (from gasoline, diesel and cooking emissions), which over time became coated with sulfate (as well as nitrate and SOA), resulting in particles with sulfate mass fraction of about 20% or less. In Figure 3.10b, particles in the size range of 0.01–0.2 μm appeared with a sulfate mass fraction of 70%. These are background particles that were introduced into the simulation by dilution with their initial SOA content (model species API1) having evaporated. The low particle number concentrations in between these main particle types originate from coagulation events.

Figure 3.10c and Figure 3.10d show the distributions after four cloud cycles. Note that the initial concentrations of the gas-phase species between the two plume hours differed as shown in Figure 3.2c. Using the population at $t_u = 0$ h, all particles started with the same composition, and particles with diameters larger than 0.1 μm underwent cloud processing, resulting in sulfate mass fractions between 30 and 60%. Since we started with particles that were all identical and after cloud processing, the particles differ in sulfate mass fractions (and other secondary species), the aerosol population became more diverse and more externally mixed. The gap in the 0.1–0.3 μm diameter range was caused by the growth of the activated particles while the non-activated particles remained unchanged. Using the population at $t_u = 12$ h, we can still see the signature of the particles that underwent cloud processing, however, it is difficult to infer if the population became more internally or externally mixed. This is where calculating mixing state metrics will help, which we will investigate next.

3.3.3 Impacts on mixing state and cloud condensation nuclei concentration

As shown qualitatively in Figure 3.10, cloud processes can change the diversity and the mixing state of particle populations. In this section we will quantify these changes for our cases more precisely using the metrics described in Chapter 3.2.4. Figure 3.11 shows the evolution of D_α , D_γ and χ after each of the four cloud cycles. After the first cloud cycle, the average particle species diversity D_α increased for aerosols that used plume hours 0 to 6 as inputs for the cloud parcel simulations. These populations started with relatively low average particle diversities. In contrast, D_α decreased for aerosols that used plume hours 7 to 24 as inputs for the cloud parcel simulations. This illustrates the fact that the addition of aerosol mass (mainly sulfate and nitrate) to a subset of particles in a population can lead to a decrease or increase in average particle diversity, depending on what the starting point is. When D_α was initially low, then adding secondary species led to more diverse particles, and D_α increased. This was the case when the aerosol consisted of different types of freshly emitted aerosol and the particles each only contained few species in the early stages of the urban plume simulation. When D_α was initially high, adding a small number of secondary species decreased the diversity, since those newly added species dominated. This was the case when the aerosol consisted of aged particles where several species commonly existed within one particle. This argument applies to both D_α and D_γ . Note that these two cases were contrasted in Riemer and West (2013) as “Prototypical cases 5 and 6”. Comparing the different cloud cycles, we observed that each cloud cycle led to a less diverse population than the previous cloud cycle.

If D_α and D_γ changed at the same rate, then χ would remain unchanged by cloud processing. However, here D_α generally decreased less than D_γ , and therefore χ increased for each cloud parcel simulation. The freshly emitted particles experienced the largest changes, especially for urban plume particle populations at $t_u = 2$ h, with χ increasing from 50% to 83% after four cycles. One exception was the case using the aerosol at $t_u = 0$ h as input, which was 100% internally mixed. The first cloud cycle therefore led to a more external mixture (but subsequent cloud cycles led to more internal mixtures), however this case is likely not relevant for real atmospheric conditions as a completely internal mixture is an idealized assumption.

Figure 3.12 graphs the progression of the diversity metrics in a D_α - D_γ diagram using the aerosol at $t_u = 12$ h as input as an example. After each cloud cycle, the mixing state index moved closer to the diagonal line which indicates a complete internal mixture ($\chi = 100\%$), with χ increasing from 69% to 87%. However, a complete internal mixture was never reached because the interstitial aerosol still contributed diversity.

The change of aerosol mixing state is likely related to the fraction of activated particles because only those undergo aqueous-phase chemistry. Figure 3.13 compares cloud droplet number fraction (number concentration of cloud droplets divided by total aerosol concentration at the start of the cloud parcel simulation) and change in mixing state for the high-emission case and the low-emission case for the first cloud cycle. The cloud droplet fraction varied between

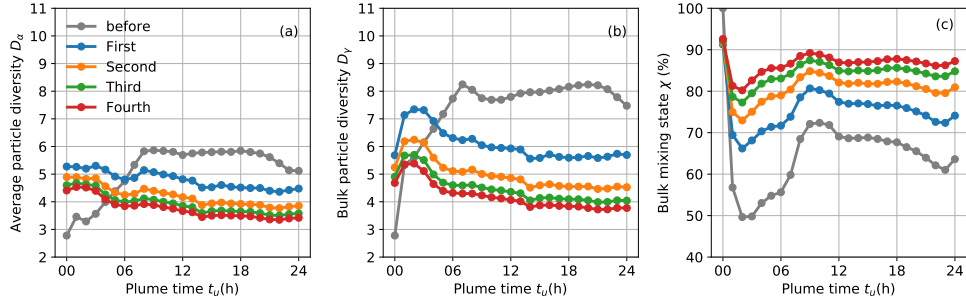


Figure 3.11: Evolution of average particle diversity D_α , bulk particle diversity D_γ and bulk mixing state χ (%) at the beginning of cloud cycle 1 and after each of the four cloud cycles (high-emission case).

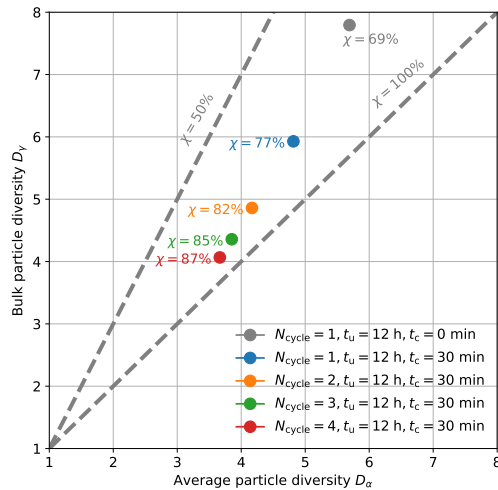


Figure 3.12: Average particle diversity D_α and bulk particle diversity D_γ diagram for the aerosol at $t_u = 12$ h at the beginning of cloud cycle 1 and after each of the four cloud cycles (high-emission case).

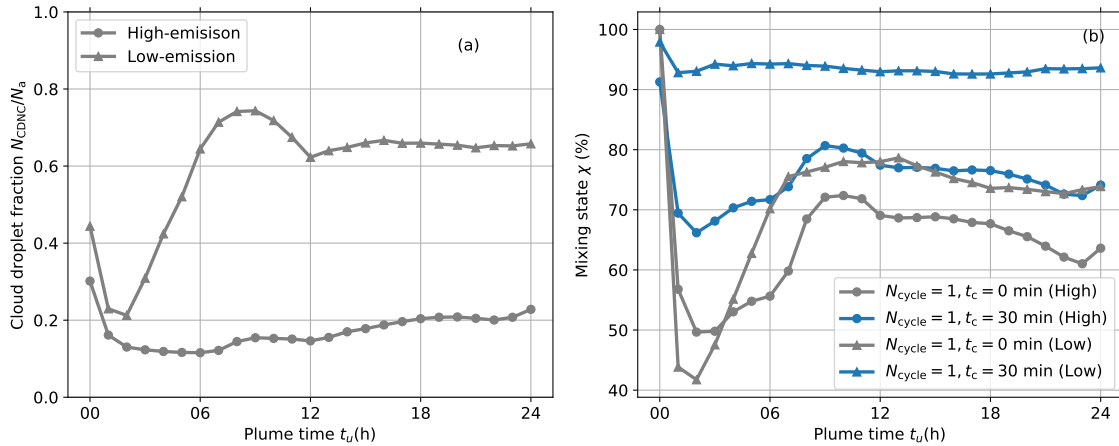


Figure 3.13: (a) Cloud droplet fraction for the low-emission case and the high-emission case (b) Mixing state before (grey lines) and after first cloud cycle (blue lines). Circles are for the high-emission case and triangles are for low-emission case.

10% and 23% and between 20% and 70% for the high-emission and low-emission cases, respectively (Figure 3.13a). The change in mixing state was indeed larger for the low-emission case where χ reaches values of over 90% after the first cloud cycle (Figure 3.13b).

CCN properties are determined by particle size and composition. As illustrated above, the activated particles grew during cloud processing and attained high hygroscopicity because of the added ammonium sulfate and ammonium nitrate. Particles with higher hygroscopicity and larger sizes have smaller critical supersaturation and activate at lower supersaturation level. Aerosol hygroscopicity has been observed to increase significantly because of the increased ammonium sulfate and ammonium nitrate mass fraction after cloud processing (Henning et al., 2014; Christiansen et al., 2020; Saliba et al., 2020).

Figure 3.16a shows the change of CCN spectrum after each cloud cycle for the high-emission case. As before, the solid lines indicate the average over the 25 urban plume cases and the shaded bands show the range of one standard deviation. For environmental supersaturations larger than 0.15%, the CCN/CN ratio remained unchanged after undergoing cloud processing. For supersaturations lower than 0.15%, the CCN/CN ratio increased with the largest increase occurring after the first cloud cycle. This is expected, since the interstitial aerosol remained unchanged during all cloud cycles, and only the particles that formed cloud droplets in the first cycle become progressively more easily activated (i.e. activate at lower and lower supersaturations).

Figure 3.16b illustrates the changes in CCN number concentration for the individual plume hours and an environmental supersaturation of 0.02%. Before cloud processing, the CCN number concentrations for all plume hours were less than 30 cm^{-3} at this supersaturation level. After cloud processing, the CCN/CN ratio increased to about 12%, which translates to a substantial increase of absolute CCN number concentration because of the large number

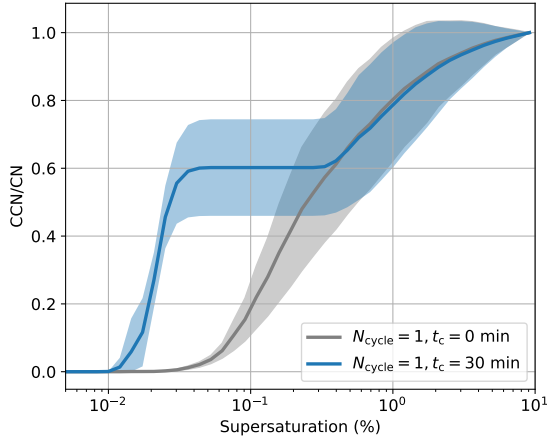


Figure 3.14: Normalized CCN spectrum before (grey) and after (blue) the first cloud cycle for the low-emission case. Solid lines are the mean distributions of all 25 cases at each cycle and the shaded band represents the 1σ range.

concentration present in this scenario. For example, the population at $t_u = 12$ h experienced an increase of CCN concentration from 25 to 547 cm^{-3} after the first cycle. While the CCN concentrations for supersaturations above the value that was reached in the cloud parcel simulations did not change, it was sensitive for supersaturations lower than what was reached in the cloud parcel simulations.

CCN concentrations for supersaturation thresholds larger than 0.15% did not change as a result of aqueous-phase chemistry. This particular threshold value was determined by the maximum supersaturation obtained in our cloud parcel simulations, which then governs the subpopulation of particles that activate. This threshold value is expected to increase for larger cooling rates which would result in larger maximum supersaturations (assuming the same aerosol population).

The results look qualitatively similar for the low-emission case (Figure 3.14), however here the supersaturation threshold above which the CCN/CN did not change was somewhat larger, consistent with the overall higher supersaturations that were reached in the cloud parcel simulations (Figure 3.6a).

Increases in CCN/CN ratio are generally attributed to both increased particle size and (potentially) increased hygroscopicity. To disentangle the two factors, we performed a sensitivity calculation where we set the hygroscopicity parameter κ of sulfate, nitrate, and ammonium to 0.1 (representative of SOA) for the particles that had experienced cloud processing (i.e., we artificially decreased the hygroscopicity of these particles). The modified CCN/CN spectrum is shown in Figure 3.15. While the addition of ammonium sulfate and nitrate increased CCN/CN from 0.01 to 0.11 for supersaturations lower than 0.04%, for the sensitivity calculation, the ratio only increased to 0.09. That is, only increasing the size, but keeping κ to a value representative of SOA rather than sulfate or nitrate will reduce the effect by 18%.

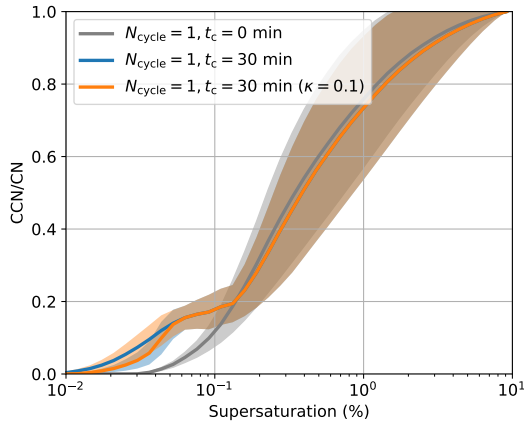


Figure 3.15: Normalized CCN spectrum before (grey) and after (blue) the first cloud cycle (high-emission case). The orange line is the CCN spectrum when assuming $\kappa = 0.1$ for sulfate, nitrate and ammonium for the particles that underwent cloud processing. Solid lines are the mean distributions of all 25 cloud parcel cases and the shaded band represents the 1σ range.

It is worth mentioning that our conclusion that CCN concentration increased after cloud processing is based on the changes of critical supersaturation. Previous studies showed that cloud processing can lead in fact to lower cloud droplet number concentrations in subsequent cloud cycles. While an increase in particle size due to aqueous-phase chemistry lowers the critical supersaturation of these particles, this will suppress the environmental supersaturation in the subsequent cloud cycle, overall reducing cloud droplet number concentration Choularton et al. (1997); Feingold and Kreidenweis (2000); Romakkaniemi et al. (2006); Ivanova and Leighton (2008); Bower et al. (1999). In our study, the maximum environmental supersaturation indeed decreased in the following cycles because of the presence of the larger, cloud-processed particles (Figure 3.6a), and the cloud droplet concentrations accordingly decreased in the following cycles (Figure 3.6b). This is consistent with Feingold and Kreidenweis (2000), where decreased cloud droplet number concentration in the subsequent cloud cycles was found for the environments with larger updraft velocity ($> 0.1 \text{ m s}^{-1}$) and does not contradict our current findings that processed particles have a higher activation potential.

3.3.4 Effects of in-cloud coagulation on aerosol mixing state

So far we presented results that did not account for coagulation events within the cloud. We generally include two different coagulation mechanisms in PartMC, coagulation due to gravitational differential settling using the coagulation efficiencies according to Hall (1980), and Brownian coagulation (Jacobson, 2005). For the size ranges of droplets in our cloud parcel simulations, which is lower than $20 \mu\text{m}$ and not large enough to initiate effective collision-coalescence (Pruppacher and Klett, 2012), coagulation due to gravitational differential settling was negligible, and therefore we

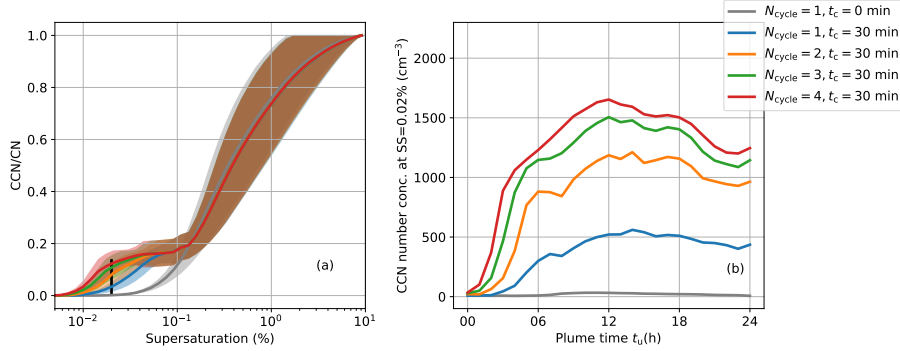


Figure 3.16: (a) CCN spectrum and (b) CCN number concentration at $ss = 0.02\%$ after each of the four cloud cycles (high-emission case). Solid lines in (a) are the mean distributions of all 25 cases at each cycle and the shaded band represents the 1σ range. The black line in (a) indicates the supersaturation level at 0.02%, taken here as an illustrative example.

focus the discussion on the impact of Brownian coagulation. This is a process that is often ignored in aerosol models (Pierce et al., 2015b). Pierce et al. (2015b) report that interstitial coagulation in clouds led to a 15%–21% decrease of total number concentration globally, associated with a global-mean aerosol indirect effect of including interstitial scavenging of +0.5 to +1.3 W m⁻².

We use the aerosol from $t_u = 12$ h as input, since this population had the largest total number concentration (see Figure 3.2a), and so we expected the impacts of Brownian coagulation to be maximized for this case. Because coagulation events were simulated stochastically and introduce an element of randomness into our simulations, we repeated the cloud parcel simulation three times and report the average and 95% confidence interval.

Figure 3.17a compares the number distribution before and after the first cloud cycle including only aqueous chemistry and including aqueous chemistry and coagulation. For the case without Brownian coagulation, the size distribution did not change for diameters smaller than 0.1 μm . With Brownian coagulation, the number concentration of particles smaller than 0.1 μm decreased slightly. The changes in number size distributions comparing $t_c = 0$ min and 30 min are shown in Figure 3.17b. Brownian coagulation rates were higher for particle pairs with large diameter difference. Here, Brownian coagulation depleted the number concentration of particles between 0.01 – 0.1 μm (the interstitial aerosol). The effects of aqueous-phase chemistry occurred at larger sizes and moved the particles from 0.1 – 0.3 μm to 0.3 – 0.5 μm .

Since Brownian coagulation in the cloud mainly affected interstitial particles, the changes to the CCN spectrum were expected to be small and should be mainly visible for higher supersaturation levels. As shown in Figure 3.18, the CCN spectrum moved left only for supersaturation level higher than 0.2%. For example, with Brownian coagulation, the CCN/CN ratio increased by 4.1% from 0.74 to 0.77 at $ss = 0.5\%$. Figure 3.18b shows the change of CN (total aerosol number concentrations) and CCN concentration in the simulated 30 minutes. Since the decrease of total

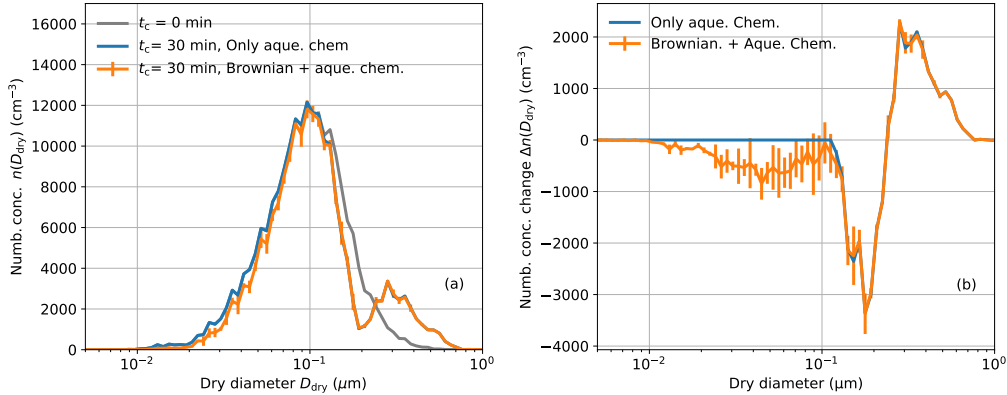


Figure 3.17: (a) Number distribution at initial condition $t_c = 0$ (grey), at $t_c = 30 \text{ min}$ with aqueous chemistry only (blue) and at $t_c = 30 \text{ min}$ with Brownian coagulation and aqueous chemistry (orange) (b) the change of number size distribution due to aqueous chemistry and Brownian coagulation. The solid orange line is the average of three realizations of the cloud parcel model simulation and the error bar is the 95% confidence interval.

aerosol concentration was larger, this led to the reported increase in CCN/CN ratio. Including Brownian coagulation caused a decrease of total aerosol concentration (by 5.9%) and of CCN concentration (by 1.7%) over the 30-min cloud parcel simulation. We expect this effect to be more pronounced for aerosol populations that contain a nucleation mode (Romakkaniemi et al., 2006), which our case did not include.

Figure 3.18c shows the evolution of D_α and D_γ using output from every minute during the cloud parcel simulation. The trajectory of the case with Brownian coagulation was almost identical with the case without Brownian coagulation, indicating negligible effects of coagulation on mixing state. Although the differences were small, it was noticeable that including coagulation does not change D_γ , since the aerosol bulk mass concentrations were not changed. However, it increased D_α , since the average particle diversity increases during coagulation (archetypical Case 4 in Riemer and West (2013)).

3.3.5 Changes in aerosol scattering and absorption abilities

The changes in aerosol size distribution and composition not only affect CCN properties, but also aerosol optical properties. We analyzed the aerosol optical properties changes in the high-emission and low-emission cases after the first cloud cycle. As shown in Figure 3.19, all populations have larger scattering coefficients after cloud processing, consistent with the findings by Yuskiewicz et al. (1999) and Romakkaniemi et al. (2006). The enhancement was more obvious for the low-emission case, where the median scattering coefficient increased from 1.3×10^{-4} to $10.9 \times 10^{-4} \text{ m}^{-1}$.

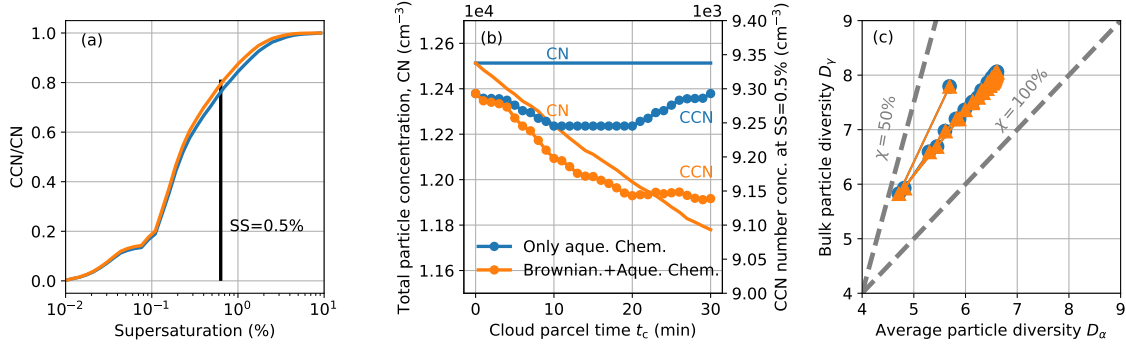


Figure 3.18: (a) CCN spectrum and (b) total CN and CCN concentration at $ss = 0.5\%$ with only aqueous chemistry (blue) and with both Brownian coagulation and aqueous chemistry (orange). The vertical line in (a) is for $ss = 0.5\%$, and solid and dotted lines in (b) are for total CN and CCN concentrations at that level respectively. (c) Effects of coagulation on aerosol mixing state metrics. The points correspond to output from every minute during the cloud parcel simulation.

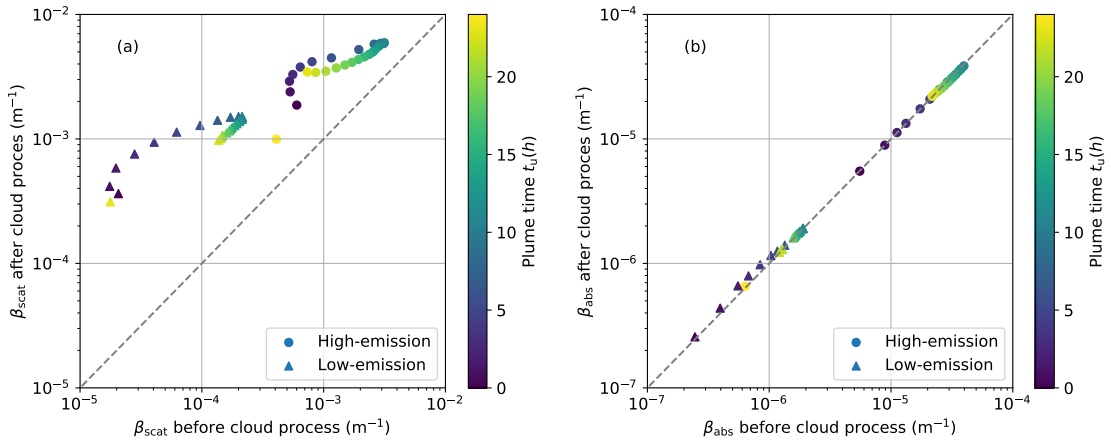


Figure 3.19: Optical properties before and after cloud processing. (a) Scattering coefficient β_{scat} . (b) Absorption coefficient β_{abs} . Circles are for high-emission case and triangles are for low-emission case. The color indicates the plume hour.

The absorption coefficients do not change after cloud processing. This can be explained by the fact that only few BC-containing particles were activated. As shown in Figure 3.20, in both the high-emission and low-emission case, the activated particles contain less than 10% of BC. Particles with larger BC fraction are smaller particles and they were not affected by cloud processing.

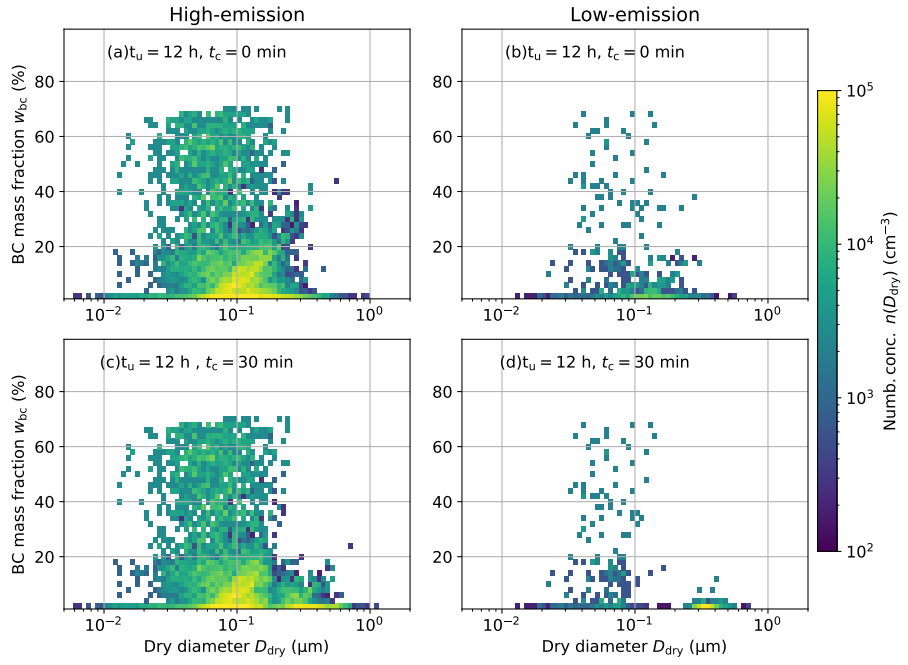


Figure 3.20: Two-dimensional number concentration distribution $n(D_p, w_{bc})$ before cloud processing (a,b) and after cloud processing (c,d) for aerosol populations from $t_u=12 \text{ h}$. The left column is for high-emission case and the right column is for low-emission case.

3.4 Conclusions

In this study, we investigated the impact of in-cloud aqueous-phase chemistry on aerosol mixing state. Using the particle-resolved model PartMC-MOSAIC, we generated particle populations of different aerosol mixing states from urban plume simulations representing polluted conditions. We used these as inputs for 30-min cloud parcel simulations that included the reduced CAPRAM 2.4 aqueous-phase chemistry mechanism. Each cloud parcel simulation was driven by the same temperature profile, with decreasing temperature during the first 10 min, constant temperature during the second 10 min, and increasing temperature during the third 10 min. While the cloud parcel simulations were simplified in that we assumed adiabatic conditions, our results are a first step towards investigating aerosol-cloud interactions within a particle-resolved framework that allows for representing aerosol mixing state without simplifying assumptions.

Coming back to the questions that we posed in the introduction, we conclude the following. We quantified changes in mixing state as a result of in-cloud processes using the diversity metrics D_α (average particle diversity) and D_γ (bulk aerosol diversity) and the mixing state index χ . The aqueous-phase chemistry processes had an “equalizing

effect” on the diversity metrics, meaning that D_α and D_γ increased due to aqueous-phase chemistry when the initial values were low and decreased when the initial values were high. The first condition applied for plume time hours 0–6 in our high-emission scenario, when fresh emissions dominated which tend to be of low diversity, consistent with observational findings (Healy et al., 2014). Adding secondary species to the activated particles increased the diversities. The opposite was the case when D_α and D_γ values started out high, which applied to plume time hours 7–24, when the plume was aged. Here, adding secondary species to the activated particles decreased the diversities.

Whether the overall population became more or less internally mixed depended on the relative changes in D_α and D_γ . For most populations in our study, aqueous-phase chemistry led to a more internally mixed aerosol. For example, for the population of plume hour $t_u = 12$ h, χ increased from 69% to 77% after the first cloud cycle, and to 87% after the fourth cloud cycle. However, a completely internal mixture was not achieved under the conditions investigated here, since only a portion of the aerosol population activated and the remaining interstitial aerosol always contributed diversity to the population. An exception was the case of plume hour $t_u = 0$, when the initial aerosol population was completely internally mixed. In this case, aqueous-phase chemistry caused the population to become more externally mixed.

The change in mixing state index χ due to cloud processing depended also on the fraction of particles that formed cloud droplets. In our high-emission case, this fraction remained below 23% and χ did not exceed 90% even after the fourth cloud cycle. In contrast, for the low-emission case, the fraction of activated particles ranged between 20% and 75%, and χ increased to over 90% after the first cloud cycle.

The size changes after cloud processing led to significant changes to aerosol microphysical properties. With ammonium nitrate and ammonium sulfate added to the activated particles, after the cloud evaporated, the activation potential of the resuspended aerosol particles increased remarkably for low supersaturation thresholds. For example, the CCN concentration for particles from the high-emission case at $t_u = 12$ h and supersaturation level 0.02% increased by a factor of 20 from 30 cm^{-3} to 547 cm^{-3} after the first cloud cycle. For subsequent cloud cycles, the increase was smaller and by the fourth cycle, it was only 8.8%.

The effects of coagulation due to gravitational settling were negligible in our simulations. This can be explained by the fact that the cloud droplets did not grow large enough for gravitational settling to take over as main coagulation mechanisms. Brownian coagulation occurred mainly between the interstitial particles at around $0.1 \mu\text{m}$ and cloud droplets at $10 \mu\text{m}$. The number concentration reduction caused by coagulation was up to 5.8 % in the cases considered while the CCN concentration was reduced by less than 2%. This therefore resulted in an increase of the CCN/CN ratio for supersaturations higher than 0.2%. The change in aerosol mixing state caused by coagulation was negligible. It should be noted that our simulations did not take into account the impact of phoretic or turbulence effects on coagulation, which could modify the efficiency of in-cloud coagulation.

We also found that cloud processing enhanced particle scattering due to particle growth, and the effects are more profound for high-emission case, with the median scattering coefficient increasing from 1.3×10^{-4} to $10.9 \times 10^{-4} \text{ m}^{-1}$. For the scenarios considered here, the particle absorption did not change, which can be explained by the fact that the cloud droplets only contained small amounts of BC.

Chapter 4

Quantifying the effects of mixing state on aerosol optical properties

This chapter develops a framework to systematically quantify the aerosol optical value errors introduced by simplified aerosol representation. I first introduce the processes to create reference and sensitivity scenarios. Then, I present the errors in aerosol absorbing and scattering properties introduced by internal mixture assumptions used by sectional aerosol models. The work is in preparation for *Atmospheric Chemistry and Physics*.

4.1 Introduction

Aerosol particles scatter and absorb incoming solar radiation, thereby impacting the global radiative balance and surface temperatures (Mitchell Jr, 1971; Charlson et al., 1992; Yu et al., 2006; Winker et al., 2010; Oikawa et al., 2013; Subba et al., 2020). Black carbon (BC), commonly emitted from combustion, has a direct radiative forcing of $+0.9 \text{ W m}^{-2}$, which is next only to CO₂ (Bond et al., 2013; Gustafsson and Ramanathan, 2016) in its warming impact. At the same time, the overall global average aerosol direct radiative forcing in the clear-sky environment is -1.9 W m^{-2} because of the presence of other non-absorbing aerosol species, which exert a cooling impact (Bellouin et al., 2005).

Radiative effects of aerosols depend on their optical properties, which, as a whole, are determined by the individual particles that the aerosol consists of. As observed in field campaigns, particles are mixtures of inorganic and organic species, and exhibit significant spacial and temporal variation in their abundance and composition (Zhang et al., 2007; Bzdek et al., 2012; Laskin et al., 2006), with considerable diversity in composition existing within individual aerosol populations. The topic of this chapter is to quantify the importance of diversity in composition for aerosol optical properties.

Aerosol composition impacts aerosol optical properties for several reasons. First, aerosol species differ in their complex refractive index. While inorganic species and many organic species have a purely real refractive index (i.e. only scatter radiation) for wavelength of visible sunlight, black carbon and some organic carbon species have a non-zero imaginary part of the refractive index and hence also absorb radiation (Corbin et al., 2018; Esteve et al., 2014; Cappa et al., 2019). Second, aerosol species differ in their hygroscopicity. This governs aerosol water uptake in a

humidified environment, which is important for scattering (Michel Flores et al., 2012; Zieger et al., 2013; Titos et al., 2014, 2016).

Lastly, the arrangement of the different aerosol species within a particle is important for determining their scattering and absorption. For mixed particles without strongly absorbing species, i.e. BC, a volume-mixing rule can be used to calculate the refractive index of the entire particle. When the particle contains BC, assuming a core-shell configuration was proven to be more accurate (Bond et al., 2006) (still assuming sphericity as particle shape). The absorption enhancement of BC-containing particles due to their non-absorbing coatings has been widely investigated (Moffet and Prather, 2009; Liu et al., 2017; Wu et al., 2020; Fierce et al., 2020). Taking the non-spherical shapes of BC-containing particles into account complicates matter considerably since Mie calculations cannot be applied and more sophisticated optical models need to be used, which are computationally much more expensive. By using the Discrete Dipole Approximation model, Scarnato et al. (2013) found BC-NaCl mixtures absorption coefficients enhancement is higher for compact BC particles completely embedded in NaCl than for lacy BC particles.

To understand the importance of aerosol composition in calculating aerosol optical properties, it is useful to define the term aerosol mixing state, that is, the distribution of aerosol species among the particles in a population (Riemer et al., 2009; Riemer and West, 2013). Aerosol mixing state in the ambient atmosphere ranges between the two idealized extremes of an external mixture on the one hand, where different aerosol species reside in different particles, and an internal mixture on the other hand, where all particles consist of the same mixture of species. Aerosols close to emission sources tend to be more (although not completely) externally mixed (Bondy et al., 2018; Rissler et al., 2014). After emission, aging processes, such as coagulation between particles and condensation of gas species on the particles, transform aerosol populations towards more internal mixtures (Healy et al., 2014; Liu et al., 2013; Zaveri et al., 2010).

Aerosol mixing state is challenging to represent in 3D chemical transport models, which usually rely on simplifying assumptions for computational efficiency. These assumptions then determine how aerosol optical properties are calculated. Optical properties are here understood by three widely-used parameters: absorption cross section, scattering cross section and asymmetry parameter (Majdi et al., 2020). For example, many 3D models use a modal approach to represent aerosol, such as The Community Multiscale Air Quality Modeling System (CMAQ)(Binkowski et al., 2007; Appel et al., 2017) and Modal Aerosol Module (MAM)(Liu et al., 2012b). The modes are externally mixed from each other, whereas within each mode, the aerosol is assumed to be internally mixed. For BC-containing modes, sphericity and a core-shell configuration are assumed, so that Mie calculations can be applied to calculate optical properties. Fierce et al. (2016) found that neglecting the diversity in coating thickness for BC-containing particles (a result of the internal mixture assumption) leads to overestimated absorption enhancement by up to 200%. Another approach is the sectional model representation, which tracks size-resolved composition, but not particle composition

diversity within a certain size, such as Two-Moment Aerosol Sectional (TOMAS) and the GLObal Model of Aerosol Processes (GLOMAP)(Kodros et al., 2018; Spracklen et al., 2005). Still, mixing state assumptions need to be invoked for each size bin. The importance of mixing state was quantified through optical closure studies. Using the measured aerosol size distributions and composition collected over East China Sea, Koike et al. (2014) found that neglecting BC mixing state can lead to uncertainty level of -18% to $+9\%$ in calculated absorption aerosol optical depth.

The uncertainties in optical properties introduced by mixing state assumptions had been also widely evaluated through model sensitivity studies. Using the AQMEII-2 model inter-comparison framework, Curci et al. (2015) quantified the sensitivity of aerosol optical properties to several parameters, including aerosol mixing state and size distribution, and they found that aerosol mixing state is the dominant factor introducing uncertainties, explaining 30–35% of the aerosol optical depth and single scattering albedo (SSA) uncertainty. Kodros et al. (2018) found that the direct radiative forcing (DRF) can vary from -1.65 to -1.34 W m^{-2} over the pan-Arctic region in spring depending on the assumption of internal or external mixture. The variation is similar when the assumptions are used to calculate DRF at the top of atmosphere (Ma et al., 2012). An open question of these sensitivity studies is that no benchmark simulation exists that represents the real mixing state, and therefore the importance of mixing state can only be assessed based on differences between varied idealized assumptions. By applying a detailed particle-resolved benchmark model, Fierce et al. (2017) found that simple mixing state assumption can result in an artificial redistribution of BC mass between particles and lead to errors in absorption. The redistribution was further confirmed to be the main source for the discrepancies between the simulated and experimentally-determined particle optical properties (Fierce et al., 2020).

The goal of this study is to systematically quantify the errors in optical properties due to simplified assumptions for mixing state, here quantified with the mixing state index χ Riemer and West (2013). A similar framework was used to quantify the error in CCN concentration (Ching et al., 2017), showing that CCN error can range from -40% to 150% when assuming the aerosol was internally mixed. The error depended on supersaturation level that CCN concentrations were evaluated at, and also aerosol mixing state. In this chapter, we want to answer: Given the aerosol mixing state, what is the error in aerosol optical values when assuming internal mixture and what are the reasons?

The chapter is structured as follows: Model description, scenario design and the definition of metrics are given in Chapter 4.2. Chapter 4.3 shows the relation between the errors in aerosol scattering and absorption and mixing state for dry aerosol populations, and Chapter 4.4 further analyzes the errors for the aerosol populations at different levels of ambient relative humidity. The errors in single scattering albedo and its implications for aerosol direct radiative forcing are analyzed in Chapter 4.5. Chapter 4.6 summarizes the main findings.

4.2 Model description, scenario libraries and metrics

4.2.1 Particle-resolved model PartMC-MOSAIC

The model used to generate the particle populations for this study is the particle-resolved model PartMC-MOSAIC. A comprehensive description of the model can be found in Riemer et al. (2009) for PartMC and in Zaveri et al. (2008a) for MOSAIC. PartMC is a Lagrangian box model which tracks the evolution of particles in a fully-mixed computational volume. The processes of emission, coagulation and dilution are simulated stochastically. Gas-phase chemistry and gas-aerosol partitioning are incorporated by coupling with the deterministic model MOSAIC. Specifically, MOSAIC uses the carbon bond based mechanism CBM-Z for gas-phase photochemical reactions (Zaveri and Peters, 1999), MTEM for calculating electrolyte activity coefficients in aqueous inorganic mixtures and MESA for calculating the phase states of the particles (Zaveri et al., 2005b). The secondary organic aerosol (SOA) treatment follows the SORGAM scheme. Aerosol water uptake is calculated using Zdanovskii-Stokes-Robinson (ZSR) method (Zaveri et al., 2008a; Zdanovskii, 1948; Stokes and Robinson, 1966) based on the composition of the inorganic portion of the particles. By this method, organic species are treated as hydrophobic, and do not contribute to water uptake. The impact of this assumption on optical properties was quantified by Nandy et al. (2021), where they found errors in single scattering ability can be over 6% if neglecting organic compounds water uptake.

4.2.2 Scenario library design

Following the strategy in Zheng et al. (2021b) and Hughes et al. (2018), we created a scenario library of a large number of PartMC-MOSAIC simulations, for this study with a focus on the aging of carbonaceous aerosol. To produce particle populations with a wide range of compositions and mixing states, we varied the model input parameters within the ranges shown in Table 4.1. We used Latin hypercube sampling (McKay et al., 2000) to create input parameter combinations for a total of 100 model simulations. The simulation time for each simulation was 24 hours beginning at 6 am local time with hourly output. This yielded a total of 2500 particle populations. All scenarios were run with 10 000 computational particles. To create aerosol initial conditions with realistic mixing states, we adopted the approach described in Zheng et al. (2021b): We carried out a first set of simulations, starting with the aerosol initial concentrations set to zero for all simulations (the “initial runs”). We then repeated the same set of simulations, but replaced the aerosol initial condition with a randomly sampled population from the initial runs (the “restart runs”). For the analysis in this chapter, we only used the results from the restart runs.

Table 4.1: Baseline and range for the input variables

Input parameters	Baseline	Range
Enviroment Variables		
Relative humidity (RH)		[0.1, 1) or [0.4, 1)
Latitude		(70°S, 70°N) or (90°S, 90°N)
Day of year		[1, 365]
Temperature		Based on latitude and day of year
Gas emission rates ($\text{mol m}^{-2} \text{s}^{-1}$)		
Sulfur dioxide (SO_2)	8.5×10^{-9}	[0-200%]
Nitrogen dioxide (NO_2)	3.0×10^{-9}	[0-200%]
Nitrogen oxide (NO)	5.7×10^{-8}	[0-200%]
Ammonia (NH_3)	8.9×10^{-9}	[0-200%]
Carbon oxide (CO)	7.8×10^{-7}	[0-200%]
Methanol (CH_3OH)	2.3×10^{-10}	[0-200%]
Acetaldehyde (ALD2)	1.7×10^{-9}	[0-200%]
Ethanol (ANOL)	5.3×10^{-9}	[0-200%]
Acetone (AONE)	7.8×10^{-10}	[0-200%]
Dimethyl sulfide (DMS)	3.8×10^{-11}	[0-200%]
Ethene (ETH)	1.8×10^{-8}	[0-200%]
Formaldehyde (HCHO)	4.1×10^{-9}	[0-200%]
Isoprene (ISOP)	2.4×10^{-10}	[0-200%]
Internal olefin carbons (OLEI)	5.9×10^{-9}	[0-200%]
Terminal olefin carbons (OLET)	5.9×10^{-9}	[0-200%]
Paraffin carbon (PAR))	1.7×10^{-7}	[0-200%]
Toluene (TOL)	6.1×10^{-9}	[0-200%]
Xylene (XYL)	5.6×10^{-9}	[0-200%]
Carbonaceous aerosol emission (single mode)		
Geometric mean diameter (D_g)		[25, 250] nm
Geometric standard deviation of diameter (σ_g)		[1.4, 2.5]
BC/OC mass ratio		[0, 100%]
Particle emission flux		$[0, 1.6 \times 10^7] \text{ m}^{-2} \text{ s}^{-1}$

Table 4.2: Refractive indices of aerosol species at $\lambda = 550$ nm

Compounds	Refractive index
H_2SO_4	1.43
$(\text{NH}_4)_2\text{SO}_4$	1.52
$(\text{NH}_4)\text{HSO}_4$	1.47
NH_4NO_3	1.5
H_2O	1.33
BC	$1.82 + 0.74i$
SOA	1.45
POA	1.45

4.2.3 Optical properties calculations

We calculated the optical properties of the particle populations using Mie calculations (Zaveri et al., 2010). These properties included the asymmetry parameter g , scattering cross section σ_{scat} and absorption cross section σ_{abs} for each particle. Particles were assumed to be spherical, and when BC was present, a core-shell configuration was assumed, with BC as the core and non-BC species as the shell. In PartMC-MOSAIC, each chemical species was assigned a refractive index and the values were the same as Zaveri et al. (2010), as listed in Table 4.2. The shell refractive index of the particle was the volume average of all the shell species, including aerosol water. The absorptivity of brown carbon has been of great interest in recent years (Corbin et al., 2018; Cappa et al., 2019), however, this was not considered in the current work. We used the wavelength λ of 550 nm for our analysis. In PartMC-MOSAIC, all particles are tracked individually in a well-mixed computational volume, and we obtain the ensemble optical property values by summing over all particles in the volume. The ensemble scattering, absorption and extinction coefficients at wavelength λ are given as

$$\beta_{\text{scat}}(\lambda) = \sum_i^N \sigma_{\text{scat},i}(\lambda) n_i, \quad (4.1)$$

$$\beta_{\text{ext}}(\lambda) = \sum_i^N \sigma_{\text{scat},i}(\lambda) n_i, \quad (4.2)$$

$$\beta_{\text{abs}}(\lambda) = \beta_{\text{ext}}(\lambda) - \beta_{\text{scat}}(\lambda), \quad (4.3)$$

where i is the particle index, n_i is the number concentration associated with particle i and N is the number of computational particles in the population. We determined the optical properties of all particle populations of our scenario libraries using these equations.

4.2.4 Quantifying the impact of mixing state through composition-averaging

To quantify the impacts of mixing state on aerosol optical properties, we employed the strategy of “composition-averaging” similar to Ching et al. (2016a). The technique is shown conceptually in Fig. 4.1. For each population in our reference scenario library, we averaged the dry particle compositions within prescribed size bins. We chose eight size bins between 0.039 and 10 μm , consistent with the bin structure of the sectional aerosol module MOSAIC used in WRF-Chem (Fast et al., 2006).

The composition-averaging procedure preserves the bulk mass concentration of each species, the total number concentration, and the particle diameters within each bin. It changes the composition so that each bin becomes internally mixed, however the composition can vary between bins. This mimics the assumption frequently made in sectional models, namely that each size bin contains an internally mixed aerosol. It is worth mentioning that PartMC-MOSAIC represents particles outside the MOSAIC bin range, especially for the lower boundary, and we used an extra bin (bin 0) to preserve the total number and mass concentrations.

The changes of two important parameters for aerosol optical properties due to composition-averaging are illustrated in Fig. 4.1, BC mass fraction and the real part of the refractive index. In the reference case, a wide range of BC mass fractions exists within the same size bin. After composition-averaging, all particles within a size bin have the same BC mass fraction. Since composition-averaging preserves the particle diameters, BC and other species are redistributed so that all particles within a size bin obtain the same mass fractions. Specifically, if a particle has lower BC mass fraction than the average level in the same size bin, BC is added to this particle from those with higher BC content. The coating species are also redistributed after composition-averaging which causes the refractive index of the coating to change. Hence, comparing optical properties before and after composition-averaging in the dry population P_1 isolates the impact of mixing state on aerosol optical properties.

Since the aerosol water content plays an important role for aerosol optical properties, we further calculated water uptake for the reference populations and for the composition averaged populations for 50% (P_2) and for 90% (P_3) relative humidity, respectively. At RH = 50%, depending on the exact composition, some particles take up water, and at RH = 90%, most particles take up water, except particles that only contain hydrophobic species, such as pure black carbon or primary organic carbon. Note that while the dry aerosol mass was conserved by the composition-averaging procedure, the water content was re-calculated after composition-averaging and could change compared to the reference population. We will discuss the impact of composition-averaging for dry conditions in Chapter 4.3 and the impact of water uptake in Chapter 4.4.

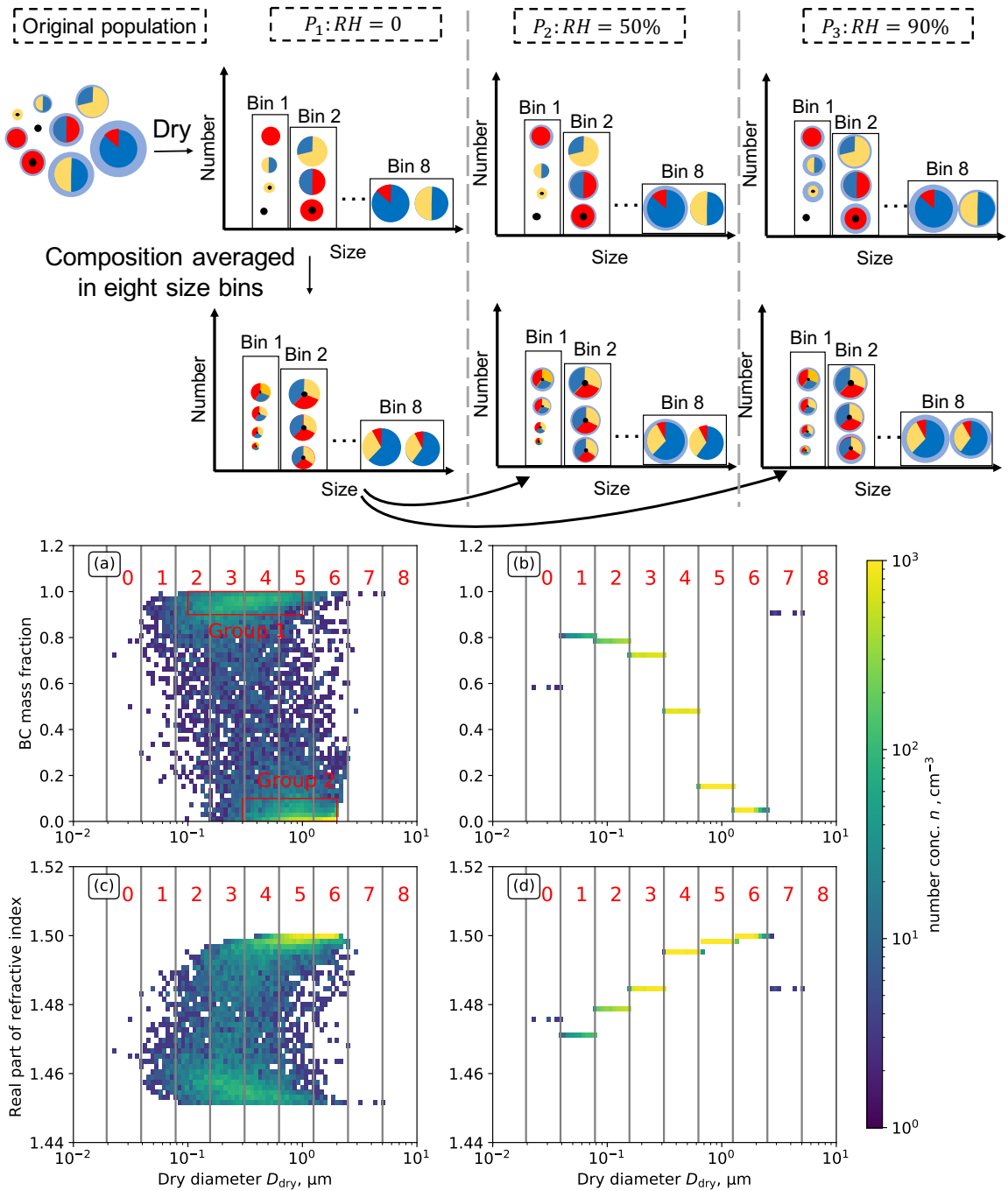


Figure 4.1: Conceptual framework of composition-averaging. In the top panel, aerosol species and water are shown with different colors. Water is in light blue, BC is in black, and other colors are for the other chemical species. The middle and bottom panels are the two-dimensional distributions of BC mass fraction and real part of refractive index for a particle population from reference (a,c) and sensitivity (b,d) scenario. The plots are colored by number concentration. Red numbers and grey lines represent the size bin ranges, comparable to the bin structure used in WRF-Chem. Bin 0 is the extra bin to preserve the total number concentration. The two red rectangles are for the analysis in Chapter 4.3. This population is taken from scenario 76 at 1 h, with $\chi=36\%$.

4.2.5 Mixing state metrics

We quantified the optical properties error introduced by simplified mixing state representation by using the metrics developed by Riemer and West (2013). These metrics include the single-particle diversity D_i , the average particle species diversity D_α and bulk population species diversity D_γ . For a population with N particles, total mass μ and A species, we can calculate those metrics from the total mass of particle i , μ_i , total mass of species a in the population, μ^a , and mass of species a in particle i , μ_i^a , for $i = 1, \dots, N$ and $a = 1, \dots, A$. Mass fraction of species a in particle i , p_i^a , mass fraction of particle i in the population, p_i and mass fraction of species a in the population, p^a are given by

$$p_i^a = \frac{\mu_i^a}{\mu_i}, \quad p_i = \frac{\mu_i}{\mu}, \quad p^a = \frac{\mu^a}{\mu}. \quad (4.4)$$

Single particle diversity D_i describes the effective species number in each particle, and is defined as

$$D_i = \prod_{a=1}^A (p_i^a)^{-p_i^a}. \quad (4.5)$$

For particles containing the same number of species type, particle diversity D_i reaches its maximum when species are present in equal amounts. Based on D_i , we can construct D_α and D_γ , which describes the average effective species number in each particle and bulk population respectively:

$$D_\alpha = \prod_{i=1}^N (D_i)^{p_i}, \quad (4.6)$$

$$D_\gamma = \prod_{i=1}^A (p^a)^{-p^a}. \quad (4.7)$$

Finally, the mixing state metric χ is defined as the affine ratio of D_α and D_γ :

$$\chi = \frac{D_\alpha - 1}{D_\gamma - 1}. \quad (4.8)$$

The values of χ vary between 0% to 100%. When $\chi = 0\%$, it indicates that the population is fully externally mixed and each particle only contains one species. The population is internally mixed when $\chi = 100\%$, and all particles have the same species mass fractions. For this work, our focus is the optical properties of the particles. Differing from the traditional chemical species mixing state index, we grouped the aerosol species by absorbing and non-absorbing species and defined a new index, χ_{opt} . It still ranges between 0% to 100% and signifies the degree to which absorbing and non-absorbing species are mixed. Since we only consider two (surrogate) aerosol species, the maximum value of

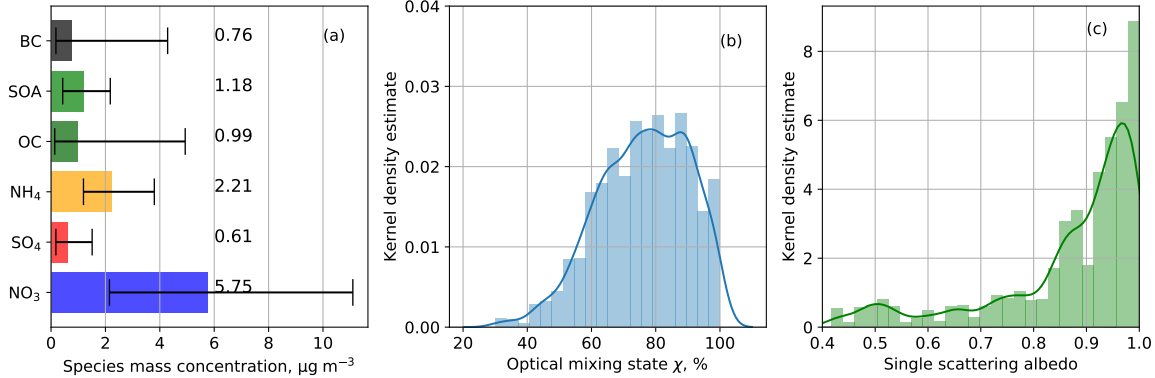


Figure 4.2: Distribution of (a) bulk species concentration, (b) optical mixing state χ and (c) SSA in the scenario libraries. Error bars in (a) are for ± 1 IQR and numbers are the median species concentration.

D_i , D_α and D_γ is 2. For the remainder of the chapter, we will refer to this index simply as χ .

Within our ensemble of aerosol populations, some were found with higher species concentrations than what would be expected in the ambient atmosphere. We applied upper thresholds to eliminate those which were calculated as the sum of 75th percentile and 1.5 IQR (interquartile range) for each of the aerosol species. After this procedure, 1809 out of 2500 populations were used for error analysis. Figure 4.2 shows the range of bulk chemical species concentrations, mixing state index, and optical properties within the selected scenario library. The simulated aerosol bulk species mass concentration in the library covered a wide range of urban conditions (Fig.4.2a), and the values were comparable to the measurements in different locations (Jimenez et al., 2009; Lanz et al., 2010). As for the distribution of mixing state, most populations had a mixing state index χ larger than 40%, with a median value of 85%. The fact that χ values smaller than 40% did not occur in our scenario library was consistent with the notion that BC rarely existed in a completely external mixture. It is frequently co-emitted with organic carbon, which form internal mixtures at the time of emission. Additionally, in urban environments, BC ages quickly, forming internal mixtures with secondary species. Figure 4.2c shows that the single scattering albedo (SSA) was larger than 0.4 for all populations, with a median value of 0.88. While SSA values lower than 0.5 can be considered extremely low (4%), most populations (72%) are with SSA larger than 0.85, which is consistent with fine mode SSA observations from AERONET (Levy et al., 2007).

The following sections describe the error introduced by composition-averaging assumptions and how the error depends on mixing state. Similar to the methods used by Ching et al. (2017), we stratified the populations by optical mixing state index χ . In order to isolate the impacts of mixing state (in the sense of how the chemical species except for aerosol water are distributed across the population) from the impacts of water uptake, we first analyzed the results for the dry population scenarios P_1 . This quantified the effects of chemical species redistribution caused by simplified mixing state assumption used in sectional models. Particles were partially or fully deliquescent in scenarios P_2 and P_3 , and these populations will be further analyzed in Chapter 4.4 to quantify the water uptake effects on aerosol optical

properties resulting from internally mixing hygroscopic and hydrophobic species.

4.3 Errors in aerosol absorptivity and scattering for dry particles

We quantified the errors in aerosol optical properties by comparing the values of reference and composition-averaged populations. The relative error for the aerosol populations was calculated as

$$\epsilon(v, \chi) = \frac{v'(\chi) - v(\chi)}{v(\chi)}, \quad (4.9)$$

where v can be SSA, β_{abs} or β_{scat} , and χ is mixing state index. We analyzed the error of these three parameters separately.

4.3.1 Errors in aerosol absorptivity due to composition-averaging

Absorption was overestimated universally after composition-averaging, and, as expected, the error was higher for more externally-mixed populations (low χ values), with $\epsilon(\beta_{\text{abs}})$ reaching up to +70% for χ of 30% (Fig.4.3). Each dot represents a particle population from the scenario library. As shown in the box plot inset, the mean overestimation was 18% and the maximum reached over 80%. The figure further contains information of BC bulk mass concentration and relative BC core size changes, which are the two main factors in determining absorptivity (Bond and Bergstrom, 2006), as represented by circle size and color, respectively. The relative BC core size change is defined as

$$\Delta D^{\text{core}} = \frac{\sum_{i=1}^N n_i D_i^{\text{core}'} - \sum_{i=1}^N n_i D_i^{\text{core}}}{\sum_{i=1}^N n_i D_i^{\text{core}}}, \quad (4.10)$$

where i is the particle index, n_i and D_i^{core} are the associated number concentration and core diameter in the reference scenario, and $D_i^{\text{core}'}$ is the core diameter in the sensitivity scenario. It is interesting to note that ΔD^{core} is always positive, that is, the average core diameter after composition-averaging is larger than the average core diameter before composition-averaging. This is a result of particle mass being a convex function of particle diameter (assuming spherical particles). Calculating the new core diameters after composition averaging will therefore always lead to on-average larger core diameters than averaging the core diameters before composition averaging.

The decreasing error with increasing χ can be explained by the magnitude of ΔD^{core} . Evidently, composition-averaging caused larger changes of BC core sizes when the populations were more externally mixed. For example, for $\chi = 30\%$, the change in core sizes was as large than +25%, while for $\chi = 95\%$, the change in core sizes was less than 5%. We also noticed a wide range of errors for populations with χ between 60 and 70%, i.e., partially internally-mixed populations. In fact, the highest overestimation of 82% was reached at $\chi = 63\%$. As indicated by the circle size, these

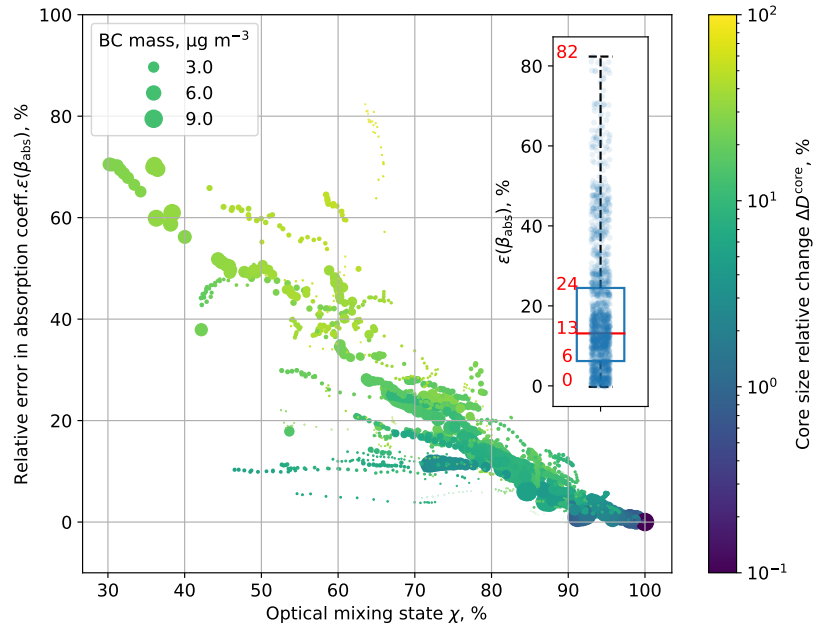


Figure 4.3: Relative error in absorption coefficients $\epsilon(\beta_{\text{abs}})$ after composition averaging. Each dot represents an aerosol population. The color denotes the change of BC diameter due to composition-averaging, and the marker size represents BC bulk mass in the population. The box plot inset shows the distribution of the error. The red line shows the median, and the edges of the dashed lines are the minimum and maximum values. Red numbers are for the minimum, first quartile, mean, third quartile and maximum values.

populations contained very little BC ($0.01 \mu\text{g m}^{-3}$) and even small changes in core sizes can lead to large relative errors in volume absorption coefficient.

For some particles, composition-averaging increases the sizes of BC cores (while at the same time decreasing the coating thickness) and for other particles it decreases the BC cores sizes (while increasing the coating thickness). It is therefore not immediately clear that composition-averaging consistently causes overestimation of aerosol absorption coefficients. At per-particle scale, for particles of the same diameter, σ_{abs} increases with increasing BC core, even though the coating thickness (and hence the absorption enhancement) decreases (Fig. 4.4).

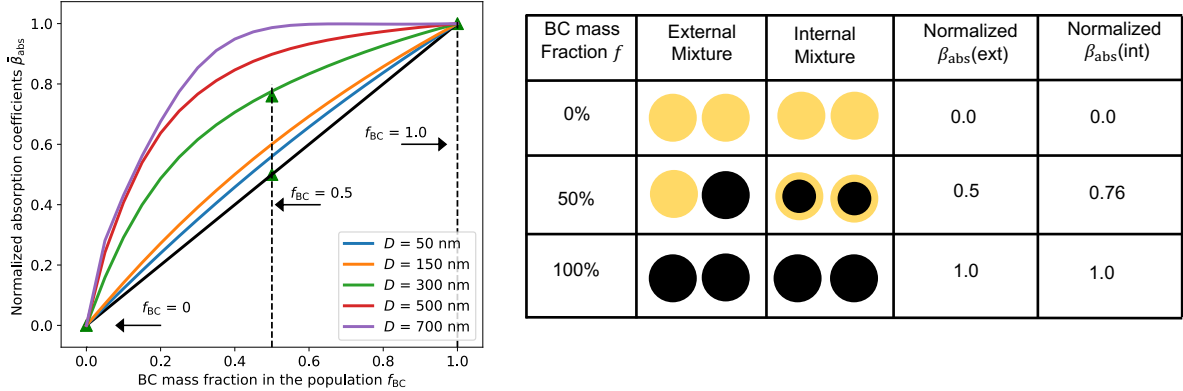


Figure 4.5: Normalized absorption coefficient as a function of BC mass fraction for five monodisperse populations with different sizes. The coating species is ammonium bisulfate with refractive index 1.47. Absorption coefficients are normalized by β_{abs} of the population with $f_{BC} = 1$ (pure BC). The black line is for BC in external mixture. Colored lines are for BC in internal mixture of different sizes. Table on the right sketches three 300 nm internal and external populations with BC mass fraction of 0%, 50%, and 100%. Black is for BC and yellow for coating species.

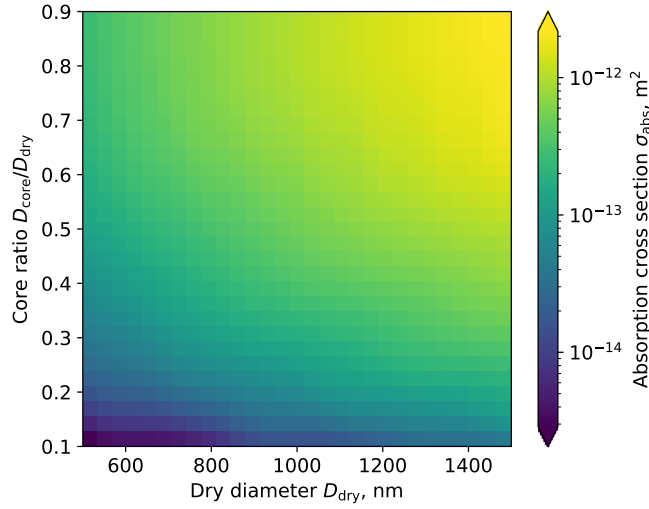


Figure 4.4: Particle absorption cross section σ_{abs} as a function of dry diameter and core ratio

However, $\epsilon(\beta_{abs})$ is determined by the entire population. The internal mixture in each size bin is reached by moving species from a group of particles to another group of particles. As the BC mass fraction distribution in Fig.4.1 shows, there are two major groups of particles in the population: Group 1 are particles with higher BC mass fraction, and group 2 are particles with lower BC mass. Particles in group 1 experience decreased absorbing ability because they are losing BC, and vice versa for particles in Group 2.

To further illustrate the effects at the population level, we show the effects of composition-averaging on the volume absorption coefficient for a simplified case of five monodisperse populations of different sizes, starting out with

completely externally mixed populations consisting of BC and ammonium bisulfate (Fig.4.5). Absorption coefficients are normalized by the absorption coefficient for $f_{BC} = 1$ (pure BC). The black line shows the normalized volume absorption coefficient for populations when all particles are externally mixed for bulk BC mass fractions f_{BC} varying between 0 and 100%. For external mixtures, absorption increases linearly with increasing BC mass fraction (black line). The linear relationship applies for all five externally-mixed populations with different diameters, so we can only see one black line in the figure.

The colored lines represent the internally-mixed monodisperse populations (i.e., after composition-averaging) for different diameters. These populations all have higher absorption coefficients compared to the corresponding externally mixed populations. The effect is more pronounced for larger particles and intermediate BC mass fractions because the maximum Δ_{core} is reached. As the table (Fig.4.5) shows, for a 300 nm population, the normalized absorption is 0.76 when the particles are internally mixed, higher than an external mixed population (0.5). Although this example is an idealized case since our populations lie between external and internal mixtures before composition-averaging and are polydisperse, this illustrates that assuming internal mixture will lead to absorption overestimation.

The current analysis was based on particles of the same sizes. However, even in the same size bins, diameters can vary up to several hundred nanometers. Cases with BC redistribution between particles of different sizes were further explored in Fig. 4.6 and confirmed that the internal mixture assumption will still lead to positive biases.

Figure 4.6 shows the relative error when moving BC from smaller particles to larger particles. Before composition averaging, small particles P_1 have diameter D_1 , BC fraction f_1 and absorption cross section σ_1 . The large particles P_2 have diameter D_2 , BC fraction f_2 and absorption cross section σ_2 . After composition-averaging, all particles have BC mass fraction f , with $f_1 > f$ and $f_2 < f$. Since the overall BC mass is conserved, we need to move BC mass from N particles of type P_1 and N is given by:

$$N = \frac{D_2^3(f - f_2)}{D_1^3(f_1 - f)}. \quad (4.11)$$

The resulting relative change in absorption coefficient for a population with N particles P_1 and one particle P_2 is defined as:

$$\epsilon(\beta_{abs}) = \frac{(\sigma'_2 + N\sigma'_1) - (\sigma_2 + N\sigma_1)}{(\sigma_2 + N\sigma_1)}, \quad (4.12)$$

where σ'_2 , σ'_1 are the absorption cross section of P_1 and P_2 after composition-averaging, respectively. As we can see from Equation 4.12, absorption relative error β_{abs} is determined by the parameters of the two particles, including $f_1, f_2, f, D_1, D_2, \sigma_1, \sigma_2$. The relations between $\Delta\beta$ and these parameters should be nonlinear and it is hard to get a unified trend for different size bins.

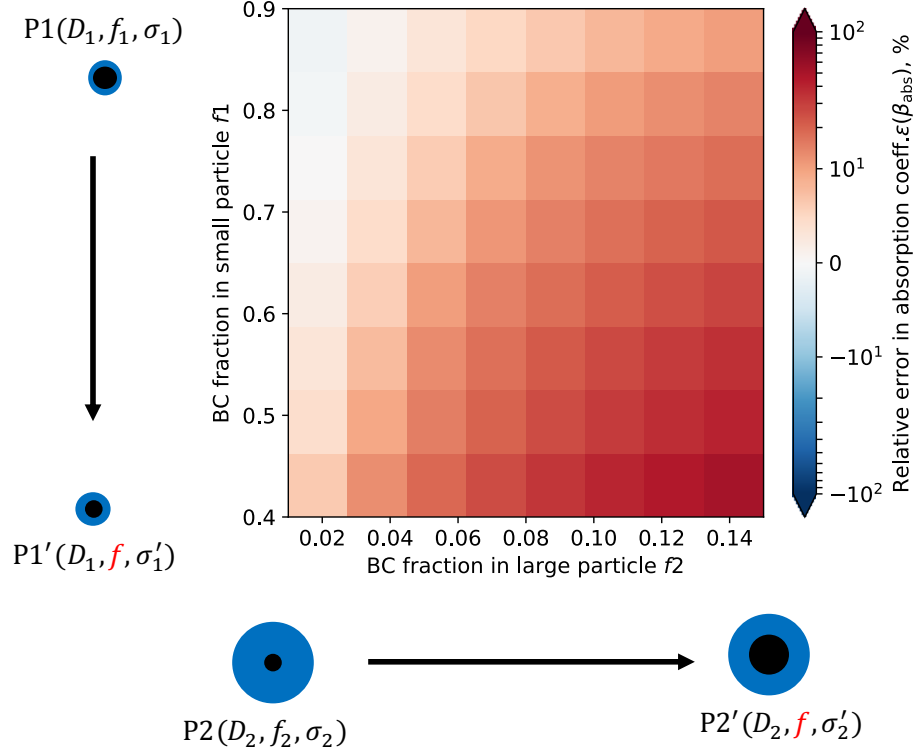


Figure 4.6: Explanation for particle optical property changes after redistribution of BC mass among a population with P_1 and P_2 . P_1 and P_2 are two particles in the same size bin, but with different diameter D_1 and D_2 . f_1 and f_2 are for the BC mass fraction before composition-averaging, and f is the unified BC mass fraction after internal mixture assumption is used. σ_1 and σ_2 are for the absorption cross section of the two particles. $D_1 = 600$ nm, $D_2 = 1200$ nm and $f = 0.2$ are the specified values for this figure.

For an initial trial, figure 4.6 shows the relative error β_{abs} when moving BC from particles P_1 with $D_1 = 600$ nm and f_1 ranging from 0.4–0.9 to a large particle P_2 with $D_2 = 1200$ nm and f_2 ranging from 0.01–0.15, to make them with unified f at 0.2. These two diameters are the lower and upper boundaries of Bin 5. For the ranges considered here, the error is mainly positive, especially for P_2 with large f_2 and P_1 with small f_1 , and $\Delta\beta$ reaches 59% when $f_1 = 0.4$ and $f_2 = 0.15$. These are the populations where the increasing absorption ability from the large particles overweighting the weakening absorption of those smaller particles after redistribution of the species. There are also some populations with small overestimation, or even underestimation when P_2 is with lower f_2 and P_1 with higher f_1 . When f_1 is 0.9 and f_2 is 0.01, $\Delta\beta$ is -1.3% . These results confirm the nonlinear variations when redistributing the species in an aerosol population. It is worth to mention that the case in the figure is with the simple assumption that particles in the population are only with two diameters, but in the simulation cases, aerosol populations are more complex with different sizes and BC mass fractions in the same size bin.

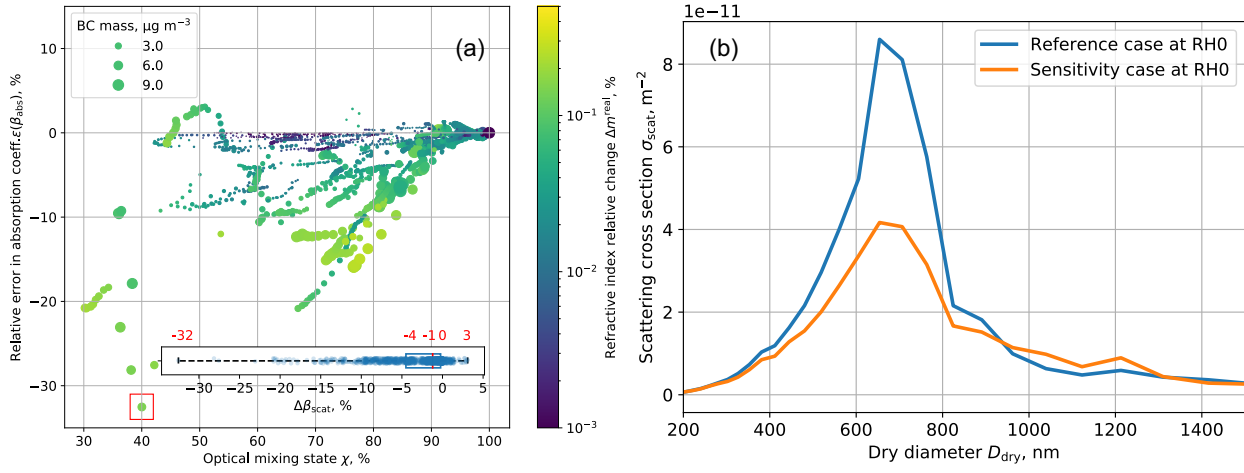


Figure 4.7: (a) Same as Figure 4.3, but for $\epsilon(\beta_{\text{scat}})$. The color is for refractive index relative change and the marker size represents BC bulk mass in the population. Red box is the populations analyzed in (b). (b) Size-resolved scattering coefficients at reference and sensitivity scenario library. This population is from scenario 77 at 2h.

4.3.2 Error in aerosol scattering due to composition-averaging

Considering the volume scattering coefficient, composition-averaging resulted in a negative relative error (Fig.4.7). Similar to what we found for $\epsilon(\beta_{\text{abs}})$, the magnitudes of $\epsilon(\beta_{\text{scat}})$ decreased with increasing χ , but were overall smaller, with the largest underestimation of -32% for a population with $\chi = 40\%$ and a median of -1.2% .

There are two factors that can affect particle scattering ability after composition-averaging, the change of the BC core size (and the corresponding change in coating thickness), and the change in the refractive index of the coating. As Fig. 4.8 shows, adding a BC core decreases the scattering ability for particles with diameters less than 1200 nm, which are the typical size ranges considered in our study. This explains the larger scattering underestimation with higher BC mass concentration in Fig. 4.7.

To further explore the effects of coating volume changes, Fig. 4.7(b) shows the size-resolved scattering coefficients before and after composition-averaging for the aerosol populations from scenario 77 at 2h, which produced the largest scattering coefficients underestimation (-32%). There is a significant decrease of σ_{scat} in the size range of 400–800 nm in the sensitivity populations, and the core ratio increment in bin 4 is responsible for this decrease (Fig. 4.9).

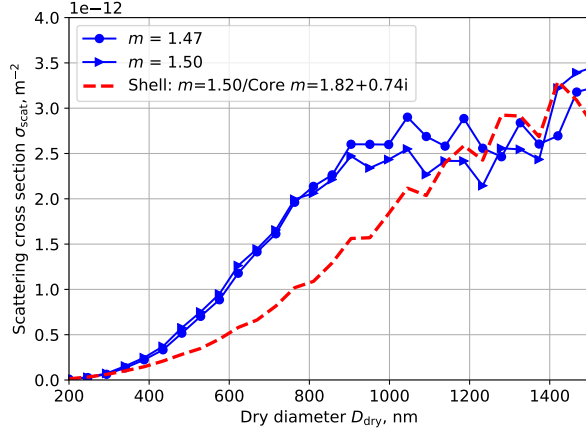


Figure 4.8: Relation between scattering ability, refractive indices and diameter. Blue lines are for non-absorbing particles and symbols indicate different refractive index. Red line is for absorbing particles including a BC core of $0.2D$.

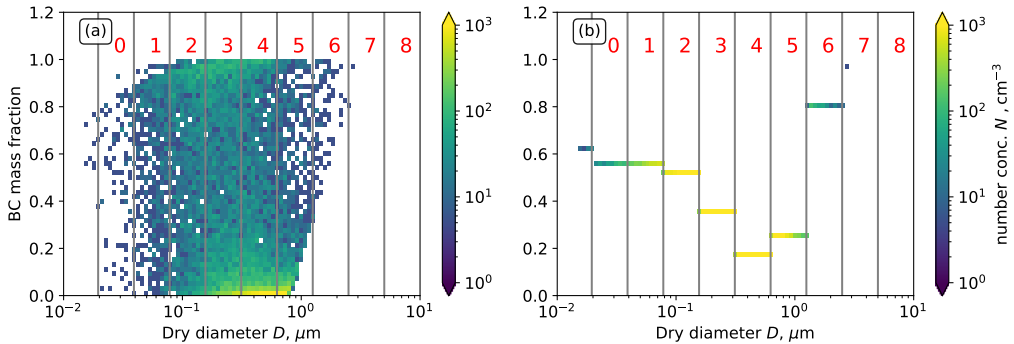


Figure 4.9: Two-dimensional distributions of BC mass fraction in (a) Reference scenario and (b) Sensitivity scenario at RH0. This population is from scenario 77 at 2h.

The blue lines in Fig. 4.8 show the scattering cross sections for two different real refractive indices. For particles with diameters between 800 and 1200 nm, a lower refractive index leads to a larger scattering cross section, even though the difference is smaller than the change caused by adding a BC core. Similar to the BC core size change ΔD^{core} in Figure 4.3, we defined a volume-weighted refractive index change, Δm^{real} , to help understand the changes in scattering. The index change is defined as:

$$\Delta m^{\text{real}} = \frac{\sum_{i=1}^N V_i m^{\text{real}'} - \sum_{i=1}^N V_i m^{\text{real}}}{\sum_{i=1}^N V_i m^{\text{real}}}, \quad (4.13)$$

where i is the particle index, V_i is the particle volume, m^{real} is the real part of the coating refractive index of the particles in the reference library, and $m^{\text{real}'}$ is for particles in the sensitivity library. As shown in Fig. 4.7, aerosol

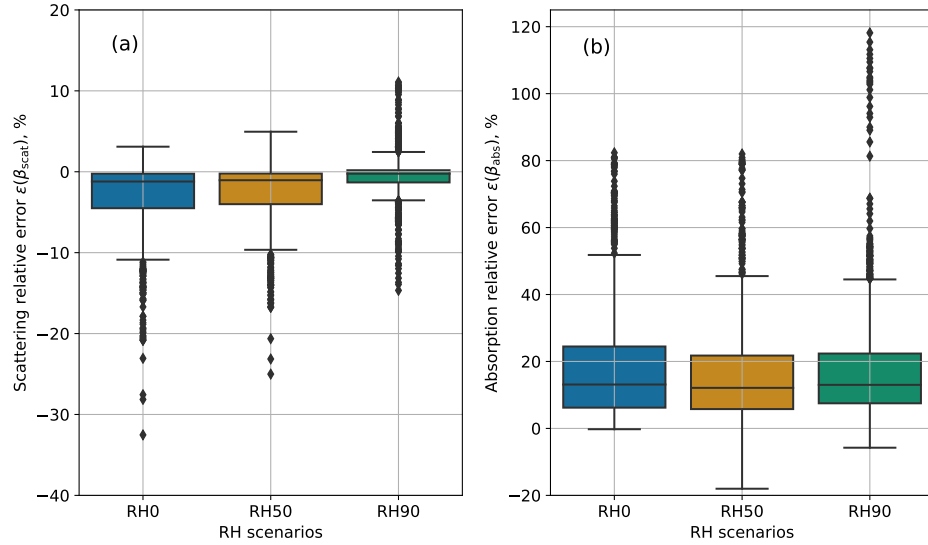


Figure 4.10: Box plot of (a) scattering relative error $\epsilon(\beta_{\text{scat}})$ and (b) absorption relative error $\epsilon(\beta_{\text{abs}})$ at three RH levels (0%, 50% and 90%). Dots are the populations with values outside $Q3 + 1.5IQR$.

populations with small errors in scattering tend to be associated with small Δm^{real} . For more externally-mixed populations (with lower χ), Δm^{real} tended to be larger.

For the effects of composition-averaging for particle scattering, we conclude that at a given value of χ , the magnitude of $\epsilon(\beta_{\text{scat}})$ was determined by the change in core/coating volumes and by changes in the coating refractive index. The increase of BC core sizes after composition-averaging is the major factor for the decrease of the scattering coefficients. Populations with large underestimation are those with higher BC mass concentrations and large refractive index changes.

4.4 The effects of water uptake on aerosol optical properties

The analysis so far was based on dry aerosol populations. In this section we investigate the impact of water uptake on the errors in absorption and scattering by considering RH values of 50% and 90%. As a reminder, we performed composition-averaging on the dry population first, and then calculated water uptake based on the averaged composition for 50% RH and 90% RH, respectively.

Considering all populations, the range of relative errors in β_{scat} decreases with increasing RH. The median value of $\epsilon(\beta_{\text{scat}})$ decreased from 1.2% for dry populations RH0 to 0.2% for 90% RH, and the IQR decreased from 4.2% to 1.5% (Fig.4.10a). In contrast, the range of relative errors in β_{abs} remains approximately the same (Fig.4.10b). The median value of error $\epsilon(\beta_{\text{abs}})$ remained at 13% and IQR decreased from 18.3% to 14.9%.

The different response of $\epsilon(\beta_{\text{abs}})$ and $\epsilon(\beta_{\text{scat}})$ after the population become humidified is due to changes of the

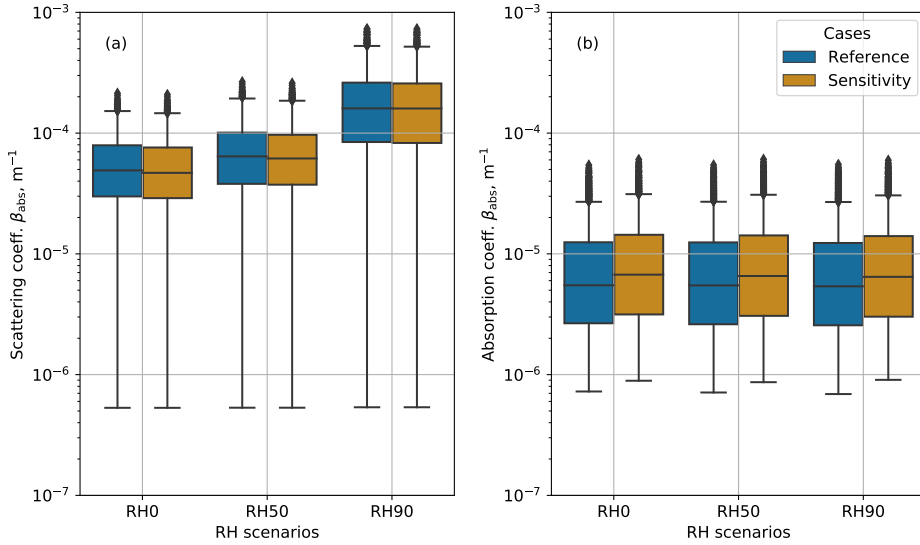


Figure 4.11: Box plots of (a) volume scattering coefficients β_{scat} , (b) volume absorption coefficients β_{abs} at the RH levels of 0, 50, 90%. Dark blue is for populations in reference scenario and Dark orange is for sensitivity scenario.

coating species after water uptake, and this is examined in Fig. 4.11. At humidified environment, scattering coefficients increased significantly. Compared with median $\beta_{\text{scat}} = 4.42 \times 10^{-5} \text{ m}^{-1}$ at RH = 10 %, β_{scat} increased to $5.90 \times 10^{-5} \text{ m}^{-1}$ and $14.8 \times 10^{-5} \text{ m}^{-1}$ at RH = 50 % and at RH = 90 %, respectively. The enhancement ratio, defined by the β_{scat} values in higher RH cases and dry case, are 1.33 at RH = 50% and 3.35 at RH = 90% in our scenario populations, which are in accordance with the previous studies (Titos et al., 2016; Burgos et al., 2020). However, the differences between the reference and sensitivity are small and keep almost unchanged at higher RH environment, which implies the water absorption ability is not affected by species redistribution. The increase of scattering coefficients and insignificant change of the differences explain the decrease of $\epsilon(\beta_{\text{abs}})$ with increasing RH. As for absorption coefficients in humidified environment, the differences between reference and sensitivity cases stay the same and the effect of RH in absorption coefficients is minimal.

4.5 Errors in single scattering albedo and implications for directive radiative forcing

The changes of scattering and absorption coefficients lead to changes in SSA, which is an important quantity that determines radiative forcing. With the definition of SSA, we can calculate the absolute error ΔSSA as:

$$\Delta\text{SSA} = \frac{\beta'_{\text{scat}}}{\beta'_{\text{scat}} + \beta'_{\text{abs}}} - \frac{\beta_{\text{scat}}}{\beta_{\text{scat}} + \beta_{\text{abs}}} = \frac{\beta'_{\text{scat}}\beta_{\text{abs}} - \beta_{\text{scat}}\beta'_{\text{abs}}}{(\beta'_{\text{scat}} + \beta'_{\text{abs}})(\beta_{\text{scat}} + \beta_{\text{abs}})}, \quad (4.14)$$

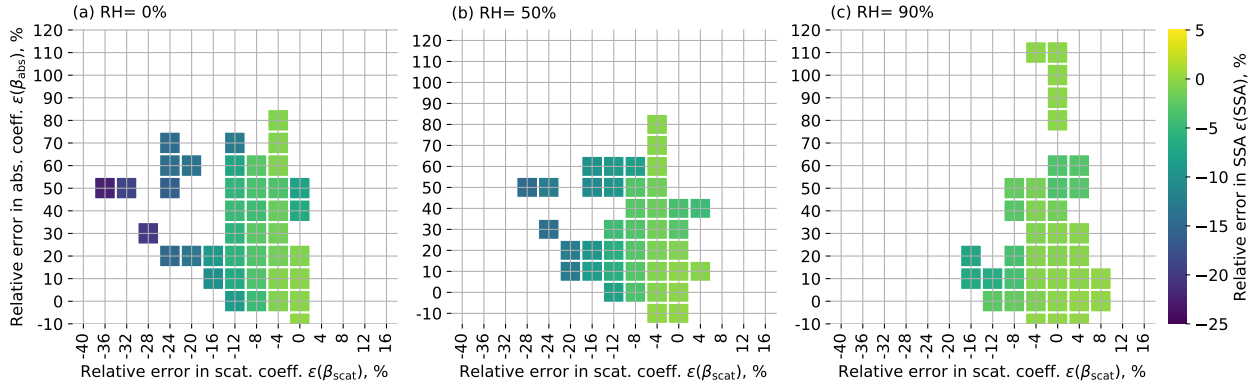


Figure 4.12: Relation between errors in SSA, scattering and absorption coefficients. Color represents the mean $\epsilon(\text{SSA})$ in the corresponding $\epsilon(\beta_{\text{scat}})$ and $\epsilon(\beta_{\text{abs}})$ histogram.

where β'_{scat} , β'_{abs} are for the scattering and absorption coefficients after composition-averaging. Based on the previous analysis, we know that β'_{scat} tends to be lower than β_{scat} and β'_{abs} greater than β_{abs} . Combining these changes with equation 4.14, these variations will result in negative values for ΔSSA and the relative error $\epsilon(\text{SSA})$, which is confirmed by Fig. 4.12.

In order to connect $\epsilon(\text{SSA})$ with $\epsilon(\beta_{\text{scat}})$ and $\epsilon(\beta_{\text{scat}})$, we sorted the populations by $\epsilon(\beta_{\text{scat}})$ and $\epsilon(\beta_{\text{abs}})$ ranges and calculated the mean $\epsilon(\text{SSA})$ for each $\epsilon(\beta_{\text{scat}})$ - $\epsilon(\beta_{\text{abs}})$ bin. For all three RH levels, $\epsilon(\text{SSA})$ was negative, meaning that composition-averaging causes an underestimation of SSA. The largest $\epsilon(\text{SSA})$ (-22%) occurred for the largest underestimation in $\epsilon(\beta_{\text{scat}})$ in the $\text{RH} = 0\%$ environment. Populations with $\epsilon(\text{SSA})$ lower than -10% were related to populations with large negative magnitudes of $\epsilon(\beta_{\text{scat}})$. Relative errors in SSA decreased in more humidified environment, accompanied by decreasing errors in scattering coefficients. The median $\epsilon(\text{SSA})$ decreased from -7.5% for $\text{RH} = 0\%$ to -2.2% in $\text{RH} = 90\%$.

The underestimation of SSA can have significant impacts in calculating direct radiative forcing. McComiskey et al. (2008) evaluated the response of directive radiative forcing to changes of several quantities, including aerosol optical depth, single scattering albedo and other related factors. They found the total uncertainties in directive radiative forcing ranged from 0.2 to 3.1 W m^{-2} and SSA introduced the largest uncertainties. Through perturbation analysis, Loeb and Su (2010) also found the SSA to be the dominant factors for direct radiative forcing uncertainties and with SSA perturbed ± 0.06 over ocean and ± 0.03 over land, the resulted uncertainties in direct aerosol radiative forcing range between -0.55 and 1.11 W m^{-2} . Considering the SSA error of -7.5% and -2.2% in dry and humidified environment in the current simulation, combining the median SSA values (Fig. 4.13), these errors translate to -0.069 and -0.021 perturbation level in SSA, respectively, and lead to the same order of magnitude of direct radiative forcing uncertainties as Loeb and Su found 

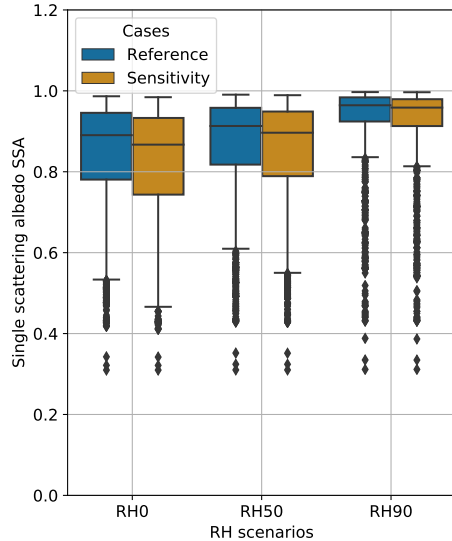


Figure 4.13: Box plots of single scattering albedo at different RH levels. Dark blue is for populations in reference scenario and Dark orange is for sensitivity scenario.

4.6 Conclusion and discussion

Simplified representation of aerosol mixing state used in current regional or global models may introduce errors in simulating aerosol optical properties, thus leading to uncertainties in calculating directive radiative forcing. In this study, the errors introduced by internal mixture assumptions used in sectional aerosol models were systematically quantified. We created a reference scenario library with 1800 aerosol populations by performing particle-resolved aerosol model simulations with PartMC-MOSAIC. We constructed a sensitivity library where particles were internally mixed in a prescribed set of size bins by applying composition-averaging. Aerosol populations from the reference and sensitivity library were then exposed to three different RH levels to understand the relative role of chemical species and water redistribution introduced by the internal mixture assumption.

The internal mixture assumption generally led to an overestimation of the volume absorption coefficients and an underestimation of the volume scattering coefficients. The relative errors for $\epsilon(\beta_{\text{abs}})$ and $\epsilon(\beta_{\text{scat}})$ reached up to 70% and -32%, respectively. The relative errors generally increased for more externally-mixed populations, although at a given value for χ a range of errors can be found, especially for the error in the scattering coefficient. For the error in the absorption coefficient, this range can be explained by the magnitude of BC core size changes that are induced by composition-averaging. For the error in the scattering coefficient, it can be explained by the magnitude of the changes in the refractive index of the coating that are induced by the composition-averaging.

For the cases with RH of 50% and 90%, the bulk aerosol water content was almost identical for the aerosol

populations in reference and sensitivity libraries. The relative error in the volume absorption coefficient $\epsilon(\beta_{\text{abs}})$ displayed a similar pattern for RH of 50% and 90% compared to the dry environment. The relative error in the volume scattering coefficient $\epsilon(\beta_{\text{scat}})$ decreased for higher relative humidities because of the enhanced scattering ability through hygroscopic growth.

The absorption overestimation and scattering underestimation resulted in an underestimation of SSA. Populations with the largest underestimation of SSA were associated with populations with the largest underestimation in scattering. At RH = 90%, decreasing relative scattering error also leads to smaller SSA inaccuracy. Based on previous studies in the literature these SSA error magnitudes translate to uncertainty ranges between -0.55 and 1.11 W m^{-2} in direct aerosol radiative forcing.

It is worth emphasizing that we used Mie theory with core-shell configuration to calculate optical properties assuming spherical particle shapes. Our results are therefore most representative of BC-containing populations, where the BC core is collapsed rather than a fractal aggregate (China et al., 2013, 2015). More accurate methods, such as discrete dipole approximation (DDA) should be used to represent these more irregular particle shapes (Scarnato et al., 2013; Curtis et al., 2008; Luo et al., 2019; Wu et al., 2020).

The species complex index should be also explored further. For current work, we used refractive index value $1.82 + 0.74i$ for BC, which is close to the medium index suggested by Stier et al. (2007), but it can vary among different measurements. Furthermore, we did not consider the absorbing abilities of organic carbons, and several studies had lately been conducted to constrain the imaginary index values of brown carbon (Liu et al., 2020). Esteve et al. (2014) has showed the index of organic aerosols are a large uncertainties in quantifying aerosol absorbing abilities. At last, for current aerosol populations, we focused on fine mode particles and ignored sea salt and dust particles, and it should also be important to include these particles for reducing the uncertainties in direct radiative forcing.

Chapter 5

Conclusions

5.1 Work summary

This dissertation improved the understanding of aerosol aging processes in clouds and the role of aerosol mixing state for aerosol scattering and absorption of sunlight. The key questions for this work were: (1) To what extent does aqueous phase chemistry change the aerosol mixing state of the aerosol that entered the cloud, and what is the role of coagulation between the interstitial particles and cloud droplets for mixing state of the aerosol? (2) Given the degree of the aerosol population mixing state, what are the errors in aerosol optical properties introduced by the internal mixture assumption and what are the causes?

In answering the first question, I designed cloud parcel simulations by using a newly developed particle-resolved aqueous chemistry model. It is a zero-dimensional adiabatic cloud parcel model with comprehensive aqueous phase reactions. The model was evaluated by comparing with results from the literature and was proved to be able of capturing the aqueous reactions involved in sulfate formation (Chapter 2). I quantified aerosol mixing state changes after aqueous chemistry processes and generalized the findings by using aerosol populations from different urban environment. I also evaluated the role of coagulation between interstitial particles and cloud droplets for aerosol mixing state (Chapter 3).

For the second question, I developed a framework to quantify the error in aerosol optical values introduced by simplified aerosol representation (Chapter 4). I created an a reference aerosol population ensemble with a wide variety of aerosol mixing state using PartMC-MOSAIC. I quantified the errors by comparing the optical properties from the reference populations to populations where the composition was averaged. I developed several metrics to explain the errors. I further explored the impact of water uptake on the optical value errors by exposing these populations to different levels of relative humidity.

5.2 Contributions

Quantifying cloud processing effects on aerosol properties. With the newly coupled particle-resolved aqueous

chemistry model, I quantified the changes of aerosol properties after cloud processing on a per-particle level. For aerosol populations dominated by fresh emissions, adding secondary species produced from aqueous chemistry increased the particle diversity. However, whether the overall population became more or less internally mixed depended on the relative changes of average particle diversity (D_α) and bulk aerosol diversity (D_γ), which determines the aerosol mixing state metric χ . For most of the cases, aqueous chemistry processes resulted in more internally-mixed populations, as shown in Fig. 5.1. Additional cloud cycles made the populations more internally mixed, but a completely internal mixture was not achieved for the simulations under consideration. The change in mixing state due to cloud processing depended also on the fraction of particles that formed cloud droplets. In the high-emission case, less than 23% of particles were activated and the mixing state metric χ remained below 90%. For the low-emission case, the activated particle portion reached up to 75% and χ increased to over 90% after cloud processing. Another finding was that after cloud processing, CCN concentration increased substantially for supersaturation levels lower than the maximum cloud supersaturation. For an aged aerosol population, CCN concentration at supersaturation level 0.02% increased from 30 to 547 cm^{-3} . In contrast to in-cloud chemistry, coagulation within clouds had a negligible impact on aerosol mixing state.

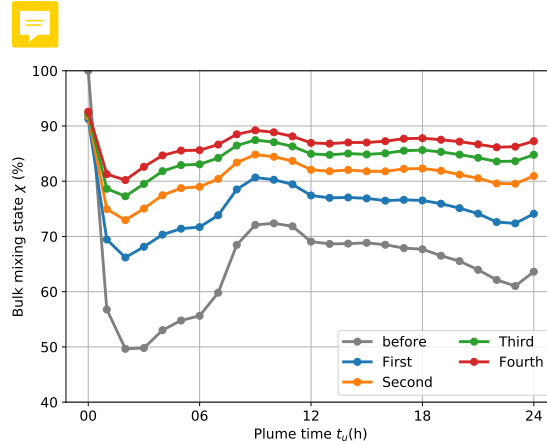


Figure 5.1: Evolution of bulk mixing state χ (%) at the beginning of cloud cycle 1 and after each of the four cloud cycles.

Quantifying the error in aerosol optical properties incurred by the internal mixture assumption. I quantified the errors introduced by the internal-mixture-assumption used in sectional aerosol models. Using a size-resolved aerosol representation generally led to an overestimation of volume absorption coefficients and an underestimation of the volume scattering coefficients. The errors were larger for externally mixed populations, as one might expect. For absorption, the relative error reached up to 70% for dry aerosol populations. These magnitudes are comparable to the ones Ching et al. (2017) found for the errors in CCN, as shown in Fig 5.2. The magnitude of the error was smaller for the scattering error, about half of the error in absorption. The increased BC core size after composition-averaging was responsible for the absorption overestimation, and scattering underestimation. The perturbations of the refractive

index of the coating also contributed to the scattering underestimation. SSA can be underestimated up to -22% and higher underestimation was associated with larger scattering underestimation. The relative humidity and associated water uptake had little effect in changing the optical value errors brought by the internal mixture assumption.

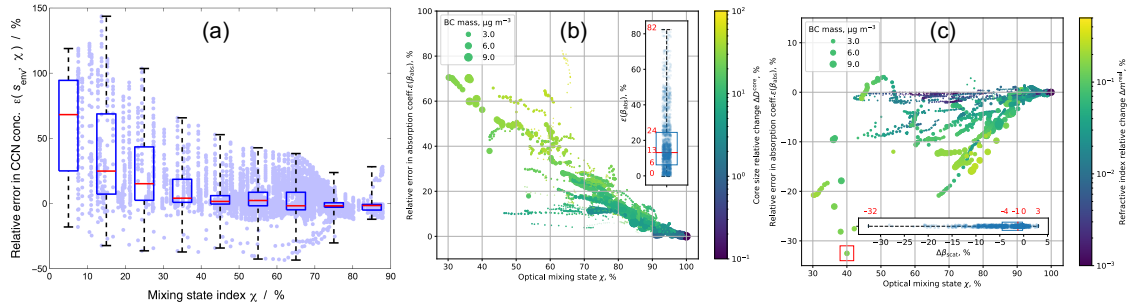


Figure 5.2: Relative error in (a) CCN concentration at supersaturation levels between 0.05% to 1%, (b) absorption coefficients and (c) scattering coefficients. (a) is adapted from Ching et al. (2017). Check Fig. 4.3 and Fig. 4.7 in Chapter 4 for figure (b) and (c) details

5.3 Future work suggestions

The findings presented in this thesis opened up several avenues for further explorations.

Sensitivity of aqueous sulfate formation to per-particle properties. I explored the capability of the particle-resolved aqueous chemistry approach to simulate the aqueous sulfate reaction systems. My simulation results confirm that the sulfate formation catalyzed by TMI can be important, but I have not yet systematically quantified the sensitivity of these processes to environmental conditions. More simulations with varied conditions should be conducted to generalized the cases with efficient TMI-catalyzed sulfate formation and to highlight the relevance of mixing state for these processes.

Improving the representation of cloud dynamics. The adiabatic cloud parcel model used for this thesis is very detailed in terms of aerosol representation but very simplified in terms of representing dynamical processes in the cloud. In particular, the mixing of the in-cloud air with air from outside the cloud is currently not included, but could be important because it changes the gas mixing ratios and aerosol number concentrations within the cloud. Future work could address this shortcoming and allow for a more realistic representation of the interactions of aerosol and cloud chemistry and cloud dynamics.

Considering the absorption of organic aerosol. In the current work, I did not consider the light absorption of organic aerosol. Several recent studies have been devoted to constraining the imaginary index values of brown carbon (Liu et al., 2020), and Esteve et al. (2014) showed that the refractive index of organic aerosols introduce large uncertainties in quantifying aerosol absorbing abilities. Future work could incorporate these results and quantify how

the presence of absorbing organic aerosol modulates the findings shown in this thesis.

Improving the representation of irregular shapes for BC-containing particles. I used Mie theory with core-shell configuration to calculate optical properties, which relies on the assumption of spherical particle shapes. Our results are therefore most representative of BC-containing populations, where the BC core is collapsed rather than a fractal aggregate (China et al., 2013, 2015). However, BC-containing particles with fractal shape do exist in the atmosphere, and therefore more accurate methods, such as discrete dipole approximation (DDA) should be used to represent these more irregular particle shapes (Scarnato et al., 2013; Curtis et al., 2008; Luo et al., 2019; Wu et al., 2020).

Including dust and sea aerosol in calculations of optical properties errors. For the simulations shown in Chapter 4, I focused on fine mode particles over urban regions. Sea salt and dust particles were not included when creating the scenario library populations. Considering the large coverage of the Earth with oceans and deserts, it is also important to include these particle types when evaluating the importance of mixing state for optical properties.

Appendix A

Appendix to Chapter 2

A.1 List of aqueous reactions coupled to PartMC-MOSAIC

This appendix shows the thermodynamic and kinetic data for the aqueous chemistry reactions coupled with PartMC-MOSAIC. It is based on the reduced CAPRAM 2.4 mechanism, and the full mechanism can refer to Ervens (2003).

Table A.1 lists the coefficients for Henry's Law.

Table A.1: Henry's Law coefficients

Henry's Law	Equilibrium	K_{298} (M atm $^{-1}$)*	$-\Delta H/R$ (K)
H1	$\text{CO}_2(\text{g}) \rightleftharpoons \text{CO}_2(\text{aq})$	3.1×10^{-2}	2423
H2	$\text{O}_3(\text{g}) \rightleftharpoons \text{O}_3(\text{aq})$	1.14×10^{-2}	2300
H3	$\text{HO}_2(\text{g}) \rightleftharpoons \text{HO}_2(\text{aq})$	9.0×10^3	0
H4	$\text{OH}(\text{g}) \rightleftharpoons \text{OH}(\text{aq})$	25	5280
H5	$\text{H}_2\text{O}_2(\text{g}) \rightleftharpoons \text{H}_2\text{O}_2(\text{aq})$	1.02×10^5	6340
H6	$\text{NO}_2(\text{g}) \rightleftharpoons \text{NO}_2(\text{aq})$	1.2×10^{-2}	1263
H7	$\text{HONO}(\text{g}) \rightleftharpoons \text{HONO}(\text{aq})$	49	4880
H8	$\text{HNO}_3(\text{g}) \rightleftharpoons \text{NO}_3^- + \text{H}^+$	4.62×10^6	10500
H9	$\text{NO}_3(\text{g}) \rightleftharpoons \text{NO}_3(\text{aq})$	6×10^{-1}	0
H10	$\text{N}_2\text{O}_5(\text{g}) \rightleftharpoons \text{N}_2\text{O}_5(\text{aq})$	1.4×10^0	0
H11	$\text{NH}_3(\text{g}) \rightleftharpoons \text{NH}_3(\text{aq})$	60.7	3920
H12	$\text{HCl}(\text{g}) \rightleftharpoons \text{Cl}^- + \text{H}^+$	1.89×10^6	8910
H13	$\text{HCHO}(\text{g}) \rightleftharpoons \text{HCHO}(\text{aq})$	2.5	7216
H14	$\text{ORA1}(\text{g}) \rightleftharpoons \text{ORA1}(\text{aq})$	5.53×10^3	5630
H15	$\text{SO}_2(\text{g}) \rightleftharpoons \text{SO}_2(\text{aq})$	1.24	3247
H16	$\text{OP1}(\text{g}) \rightleftharpoons \text{OP1}(\text{aq})$	310	5607
H17	$\text{ORA2}(\text{g}) \rightleftharpoons \text{ORA2}(\text{aq})$	5.5×10^3	5890
H18	$\text{MO2}(\text{g}) \rightleftharpoons \text{MO2}(\text{aq})$	310	5607
H19	$\text{ETHPX}(\text{g}) \rightleftharpoons \text{ETHPX}(\text{aq})$	340	87
H20	$\text{ETOH}(\text{g}) \rightleftharpoons \text{ETOH}(\text{aq})$	190	6290
H21	$\text{CH3OH}(\text{g}) \rightleftharpoons \text{CH3OH}(\text{aq})$	220	5390
H22	$\text{ALD}(\text{g}) \rightleftharpoons \text{ALD}(\text{aq})$	4.8	6254
H23	$\text{BR2}(\text{g}) \rightleftharpoons \text{BR2}(\text{aq})$	0.758	3800
H24	$\text{CL2}(\text{g}) \rightleftharpoons \text{CL2}(\text{aq})$	9.15×10^{-2}	2490
H25	$\text{SULF}(\text{g}) \rightleftharpoons \text{HSO}_4^- + \text{H}^+$	8.7×10^{14}	0
H26	$\text{HNO}_4(\text{g}) \rightleftharpoons \text{HNO}_4(\text{aq})$	3×10^4	0
H27	$\text{ACO}_3(\text{g}) \rightleftharpoons \text{ACO}_3(\text{aq})$	6.69×10^2	5893
H28	$\text{GLY}(\text{g}) \rightleftharpoons \text{GLY}(\text{aq})$	1.40	0
H29	$[\text{O}_2]^{**}(\text{g}) \rightleftharpoons \text{O}_2(\text{aq})$	1.3×10^{-3}	1700

Table A.1: Continued.

Henry's Law	Equilibrium	K_{298} (M atm $^{-1}$)	$-\Delta H/R$ (K)
H30	$\text{CLNO}_2(\text{g}) \rightleftharpoons \text{CLNO}_2(\text{aq})$	0.024	0.0
H31	$\text{BRNO}_2(\text{g}) \rightleftharpoons \text{BRNO}_2(\text{aq})$	0.3	0.0
H32	$\text{BRCL}(\text{g}) \rightleftharpoons \text{BRCL}(\text{aq})$	0.94	0.0
H33	$\text{NO}(\text{g}) \rightleftharpoons \text{NO}(\text{aq})$	1.9×10^{-3}	0.0

*: $K = K_{298} \exp\left(-\frac{\Delta H}{R}\left(\frac{1}{T} - \frac{1}{298}\right)\right)$

**: Specie with square bracket indicates its concentration is constant.

Table A.2 lists the coefficients for aqueous chemical reactions.

Table A.2: Aqueous chemical reactions

Aqueous chemistry	Reaction	K_{298} (M $^{-n}$ s $^{-1}$)	$-E/R$ (K)
A1	$\text{FEOH}^{2+} \longrightarrow \text{FE}^{2+} + \text{OH}(\text{aq})$	4.76×10^{-3}	2.20
A2	$\text{NO}_3^- \longrightarrow \text{NO}_2(\text{aq}) + \text{OH}(\text{aq}) + \text{OH}^-$	4.57×10^{-7}	2.59
A3	$\text{H}_2\text{O}_2(\text{aq}) \longrightarrow \text{OH}(\text{aq}) + \text{OH}(\text{aq})$	7.64×10^{-6}	2.46
A4	$\text{FEC}_2(\text{O}_4)_2^- \longrightarrow \text{FE}^{2+} + \text{C}_2\text{O}_4^{2-} + \text{CO}_2(\text{aq}) + \text{CO}_2^-$	2.47×10^{-2}	1.96
A5	$\text{H}_2\text{O}_2(\text{aq}) + \text{FE}^{2+} \longrightarrow \text{FE}^{3+} + \text{OH}(\text{aq}) + \text{OH}^-$	50.0	0.0
A6	$\text{H}_2\text{O}_2(\text{aq}) + \text{Cu}^+ \longrightarrow \text{Cu}^{2+} + \text{OH}(\text{aq}) + \text{OH}^-$	7000.0	0.0
A7	$\text{O}_2^- + \text{FE}^{3+} \longrightarrow \text{FE}^{2+} + \text{O}_2(\text{aq})$	1.5×10^8	0.0
A8	$\text{HO}_2(\text{aq}) + \text{FE(OH)}^{2+} \longrightarrow \text{FE}^{2+} + \text{O}_2(\text{aq}) + [\text{H}_2\text{O}](\text{aq})$	1.3×10^5	0.0
A9	$\text{O}_2^- (\text{aq}) + \text{FE(OH)}^{2+} \longrightarrow \text{FE}^{2+} + \text{O}_2(\text{aq}) + \text{OH}^-$	1.5×10^8	0.0
A10	$\text{O}_2^- + \text{FE}^{2+} \longrightarrow \text{FE}^{3+} + \text{H}_2\text{O}_2(\text{aq}) + 2 \text{OH}^- - 2 [\text{H}_2\text{O}](\text{aq})$	1.0×10^7	0.0
A11	$\text{HO}_2(\text{aq}) + \text{FE}^{2+} \longrightarrow \text{FE}^{3+} + \text{H}_2\text{O}_2(\text{aq}) + 2 \text{OH}^- - 2 [\text{H}_2\text{O}](\text{aq})$	1.2×10^6	-5050.0
A12	$\text{OH}(\text{aq}) + \text{FE}^{2+} \longrightarrow \text{FE(OH)}^{2+}$	4.3×10^8	-1100
A13	$\text{O}_2^- + \text{Cu}^+ \longrightarrow \text{Cu}^{2+} + \text{H}_2\text{O}_2(\text{aq}) + 2 \text{OH}^- - 2 [\text{H}_2\text{O}](\text{aq})$	1.0×10^{10}	0.0
A14	$\text{HO}_2(\text{aq}) + \text{Cu}^+ \longrightarrow \text{Cu}^{2+} + \text{H}_2\text{O}_2(\text{aq}) + \text{OH}^- - [\text{H}_2\text{O}](\text{aq})$	2.3×10^9	0.0
A15	$\text{HO}_2(\text{aq}) + \text{Cu}^{2+} \longrightarrow \text{Cu}^+ + \text{O}_2(\text{aq}) + \text{H}^+$	1.0×10^8	0.0
A16	$\text{O}_2^- + \text{Cu}^{2+} \longrightarrow \text{Cu}^+ \text{O}_2(\text{aq})$	8×10^9	0.0
A17	$\text{FE}^{3+} + \text{Cu}^+ \longrightarrow \text{FE}^{2+} + \text{Cu}^{2+}$	1.3×10^7	0.0
A18	$\text{FE(OH)}^{2+} + \text{Cu}^+ \longrightarrow \text{FE}^{2+} + \text{Cu}^{2+} + \text{OH}^-$	1.3×10^7	0.0
A19	$\text{O}_3(\text{aq}) + \text{O}_2^- \longrightarrow \text{O}_3^- + \text{O}_2(\text{rm aq})$	1.5×10^9	0.0
A20	$\text{HO}_3(\text{aq}) \longrightarrow \text{OH}(\text{aq}) + \text{O}_2(\text{aq})$	330.0	-4500.0
A21	$\text{H}_2\text{O}_2(\text{aq}) + \text{OH}(\text{aq}) \longrightarrow \text{HO}_2(\text{aq}) + \text{H}_2\text{O}$	3.0×10^7	-1680
A22	$\text{HSO}_3^- + \text{OH}(\text{aq}) \longrightarrow \text{SO}_3^- + \text{H}_2\text{O}$	2.7×10^9	0
A23	$\text{Cu}^+ + \text{O}_2(\text{aq}) \longrightarrow \text{Cu}^{2+} + \text{O}_2^-$	4.6×10^5	0.0
A24	$\text{FE}^{2+} + \text{O}_3(\text{aq}) \longrightarrow \text{FEO}^{2+} + \text{O}_2(\text{aq})$	8.2×10^5	-4690.0
A25	$\text{FEO}^{2+} + \text{Cl}^- \longrightarrow \text{FE}^{3+} + \text{CLOH}^- + \text{OH}^- - [\text{H}_2\text{O}](\text{aq})$	100.0	0.0

Table A.3 lists constants for equilibrium equations.

Table A.2: Continued.

Aqueous chemistry	Reaction	K_{298} ($M^{-n} s^{-1}$)	$-E/R$ (K)
A26	$\text{FEO}^{2+} + \text{FE}^{2+} \longrightarrow 2\text{FE}^{3+} + 2\text{OH}^-$	7.2×10^4	-842.0
A27	$\text{N}_2\text{O}_5(\text{aq}) \longrightarrow \text{NO}_2^+ + \text{NO}_3^-$	1.0×10^9	0.0
A28	$\text{NO}_2^+ + [\text{H}_2\text{O}](\text{aq}) \longrightarrow \text{NO}_3^- + \text{H}^+ + \text{SO}_3^-$	8.9×10^7	0.0
A29	$\text{NO}_3(\text{aq}) + \text{HSO}_3^- \longrightarrow \text{NO}_3^- + \text{H}^+ + \text{SO}_3^-$	1.3×10^9	-2000.0
A30	$\text{NO}_3(\text{aq}) + \text{SO}_4^{2-} \longrightarrow \text{NO}_3^- + \text{SO}_4^-$	1.0×10^5	0.0
A31	$\text{NO}_4^- \longrightarrow \text{NO}_2^- + \text{O}_2(\text{aq})$	4.5×10^{-2}	0.0
A32	$\text{HNO}_4(\text{aq}) + \text{HSO}_3^- \longrightarrow \text{HSO}_4^- + \text{H}^+ + \text{NO}_3^-$	3.3×10^5	0.0
A33	$\text{NO}_2^+ + \text{Cl}^- \longrightarrow \text{CLNO}_2(\text{aq})$	1.0×10^{10}	0.0
A34	$\text{NO}_2^+ + \text{Br}^- \longrightarrow \text{BRNO}_2(\text{aq})$	1.0×10^{10}	0.0
A35	$\text{CLNO}_2(\text{aq}) + \text{Br}^- \longrightarrow \text{NO}_2^- + \text{BRCL}(\text{aq})$	5.0×10^6	0.0
A36	$\text{BRNO}_2(\text{aq}) + \text{Br}^- \longrightarrow \text{BR}_2(\text{aq}) + \text{NO}_2^-$	2.55×10^4	0.0
A37	$\text{BRNO}_2(\text{aq}) + \text{Cl}^- \longrightarrow \text{NO}_2^- + \text{BrCl}(\text{aq})$	10.0	0.0
A38	$\text{HMS}^- + \text{OH}(\text{aq}) \longrightarrow \text{CHOHSO}_3^- + [\text{H}_2\text{O}](\text{aq})$	3.0×10^8	0.0
A39	$\text{O}_2\text{CHOHSO}_3^- + \text{O}_2(\text{aq}) \longrightarrow \text{O}_2\text{CHOHSO}_3^-$	2.6×10^9	0.0
A40	$\text{O}_2\text{CHOHSO}_3^- \longrightarrow \text{HO}_2(\text{aq}) + \text{CHOSO}_3^-$	1.7×10^4	0.0
A41	$\text{O}_2\text{CHOHSO}_3^- \longrightarrow \text{O}_2\text{CHO}(\text{aq}) + \text{HSO}_3^-$	7×10^3	0.0
A42	$\text{CHOSO}_3^- + [\text{H}_2\text{O}](\text{aq}) \longrightarrow \text{HSO}_3^- + \text{ORA1}(\text{aq})$	1.26×10^{-2}	0.0
A43	$\text{O}_2\text{CHO}(\text{aq}) + [\text{H}_2\text{O}](\text{aq}) \longrightarrow \text{ORA1}(\text{aq}) + \text{HO}_2(\text{aq})$	44.32	0.0
A44	$\text{HSO}_3^- + \text{H}_2\text{O}_2(\text{aq}) + \text{H}^+ \longrightarrow \text{SO}_4^{2-} + 2\text{H}^+ + [\text{H}_2\text{O}](\text{aq})$	7.2×10^7	-4000.0
A45	$\text{HSO}_3^- + \text{O}_3(\text{aq}) \longrightarrow \text{SO}_4^{2-} + \text{H}^+ + \text{O}_2(\text{aq})$	3.7×10^5	-5530.0
A46	$\text{SO}_3^{2-} + \text{O}_3(\text{aq}) \longrightarrow \text{SO}_4^{2-} + \text{O}_2(\text{aq})$	1.5×10^9	-5280.0
A47	$\text{SO}_5^- + \text{FE}^{2+} \longrightarrow \text{HSO}_5^- + \text{FE OH}^{2+}$	2.65×10^7	-5809.0
A48	$\text{HSO}_5^- + \text{FE}^{2+} \longrightarrow \text{SO}_4^- + \text{FE OH}^{2+}$	3.0×10^4	0.0
A49	$\text{FE}^{2+} + \text{SO}_4^- \longrightarrow \text{FE OH}^{2+} + \text{SO}_4^{2-} + \text{H}^+$	4.6×10^9	2165.0
A50	$\text{SO}_5^- + \text{SO}_5^- \longrightarrow \text{SO}_4^- + \text{SO}_4^- + \text{O}_2(\text{aq})$	2.2×10^8	-2600.0
A51	$\text{SO}_5^- + \text{HO}_2(\text{aq}) \longrightarrow \text{SO}_5\text{O}_2\text{H}^-$	1.7×10^9	0.0
A52	$\text{SO}_5\text{O}_2^{2-} \longrightarrow \text{HSO}_5^- + \text{O}_2(\text{aq}) + \text{OH}^- - [\text{H}_2\text{O}](\text{aq})$	1.2×10^3	0.0
A53	$\text{SO}_3^- + \text{O}_2(\text{aq}) \longrightarrow \text{SO}_5^-$	2.5×10^9	0.0
A54	$\text{SO}_4^- + [\text{H}_2\text{O}](\text{aq}) \longrightarrow \text{SO}_4^{2-} + \text{OH}(\text{aq}) + \text{H}^+$	11.0	-1110.0
A55	$\text{HSO}_5^- + \text{HSO}_3^- + \text{H}^+ \longrightarrow 2\text{SO}_4^{2-} + 3\text{H}^+$	7.14×10^6	0.0
A56	$\text{CH}_3\text{OH}(\text{aq}) + \text{OH}(\text{aq}) \longrightarrow \text{CH}_2\text{OH}(\text{aq}) + [\text{H}_2\text{O}](\text{aq})$	1.0×10^9	0.0
A57	$\text{CH}_2\text{OH}(\text{aq}) + \text{O}_2(\text{aq}) \longrightarrow \text{O}_2\text{CH}_2\text{OH}(\text{aq})$	2×10^9	0.0
A58	$\text{O}_2\text{CH}_2\text{OH}(\text{aq}) + \text{O}_2\text{CH}_2\text{OH}(\text{aq}) \longrightarrow \text{CH}_2\text{OH}(\text{aq}) + \text{O}_2(\text{aq}) + \text{aHCHO}$	1.05×10^9	0.0
A59	$\text{ETOH}(\text{aq}) + \text{OH}(\text{aq}) \longrightarrow \text{CH}_3\text{CHOH}(\text{aq}) + [\text{H}_2\text{O}](\text{aq})$	1.9×10^9	0.0
A60	$\text{CH}_3\text{CHOH}(\text{aq}) + \text{O}_2(\text{aq}) \longrightarrow \text{O}_2\text{CH}_3\text{CHOH}(\text{aq})$	2.0×10^9	0.0
A61	$\text{O}_2\text{CH}_3\text{CHOH}(\text{aq}) + \text{ALD}(\text{aq}) \longrightarrow \text{HO}_2(\text{aq})$	52.0	-7217.0
A62	$\text{CH}_2\text{OH}_2(\text{aq}) + \text{OH}(\text{aq}) \longrightarrow \text{CHOH}_2(\text{aq}) + [\text{H}_2\text{O}](\text{aq})$	1.0×10^9	-1020.0
A63	$\text{CHOH}_2(\text{aq}) + \text{O}_2(\text{aq}) \longrightarrow \text{HO}_2(\text{aq}) + \text{ORAQ}_1(\text{aq})$	2.0×10^9	0.0
A64	$\text{CH}_3\text{CHOH}_2(\text{aq}) + \text{OH}(\text{aq}) \longrightarrow \text{CH}_3\text{COH}_2(\text{aq}) + [\text{H}_2\text{O}](\text{aq})$	1.2×10^9	0.0
A65	$\text{ALD}(\text{aq}) + \text{OH}(\text{aq}) \longrightarrow \text{CH}_3\text{CO}(\text{aq}) + [\text{H}_2\text{O}](\text{aq})$	3.6×10^9	0.0
A66	$\text{ORA1}(\text{aq}) + \text{OH}(\text{aq}) \longrightarrow \text{CO}_2\text{H}(\text{aq}) + [\text{H}_2\text{O}](\text{aq})$	1.3×10^8	-1000.0
A67	$\text{HCOO}^- + \text{OH}(\text{aq}) \longrightarrow \text{CO}_2\text{H}(\text{aq}) + \text{OH}^-$	3.2×10^9	-1000.0
A68	$\text{ORA}_2(\text{aq}) + \text{OH}(\text{aq}) \longrightarrow \text{CH}_2\text{COOH}(\text{aq}) + [\text{H}_2\text{O}](\text{aq})$	1.5×10^7	-1330.0
A69	$\text{MCOO}^- + \text{OH}(\text{aq}) \longrightarrow \text{CH}_2\text{COO}^- + [\text{H}_2\text{O}](\text{aq})$	1.5×10^7	-1800.0
A70	$\text{CH}_2\text{COOH}(\text{aq}) + \text{O}_2(\text{aq}) \longrightarrow \text{ACO}_3(\text{aq})$	1.7×10^9	0.0
A71	$\text{MO}_2(\text{aq}) + \text{MO}_2(\text{aq}) \longrightarrow \text{CH}_3\text{OH}(\text{aq}) + \text{HCHO}(\text{aq}) + \text{O}_2(\text{aq})$	7.4×10^7	0.0
A72	$\text{MO}_2(\text{aq}) + \text{MO}_2(\text{aq}) \longrightarrow \text{Ch}_3\text{O}(\text{aq}) + \text{CH}_3\text{O}(\text{aq}) + \text{O}_2(\text{aq})$	3.6×10^7	-2200.0
A73	$\text{ACO}_3(\text{aq}) + \text{ACO}_3(\text{aq}) \longrightarrow 2\text{MO}_2(\text{aq}) + 2\text{CO}_2(\text{aq}) + \text{O}_2(\text{aq})$	1.5×10^8	0.0
A74	$\text{MO}_2(\text{aq}) + \text{HSO}_3^- \longrightarrow \text{OP}_1(\text{aq}) + \text{SO}_3^-$	5.0×10^5	0.0

Table A.2: Continued.

Aqueous chemistry	Reaction	K_{298} ($M^{-n} s^{-1}$)	$-E/R$ (K)
A75	$\text{ETHPX(aq)} + \text{ETHPX(aq)} \longrightarrow \text{CH}_3\text{CH}_2\text{O(aq)} + \text{CH}_3\text{CH}_2\text{O(aq)} + \text{O}_2(\text{aq})$	1.0×10^8	750.0
A76	$\text{CH}_3\text{CH}_2\text{O(aq)} \longrightarrow \text{CH}_3\text{CHOH(aq)}$	1.0×10^6	0.0
A77	$\text{OH(aq)} + \text{HC}_2\text{O}_4^- \longrightarrow \text{C}_2\text{O}_4^- + [\text{H}_2\text{O}](\text{aq})$	3.2×10^7	0.0
A78	$\text{OH(aq)} + \text{C}_2\text{O}_4^{2-} \longrightarrow \text{OH}^- + \text{C}_2\text{O}_4^-$	5.3×10^6	0.0
A79	$\text{C}_2\text{O}_4^- + \text{O}_2(\text{aq}) \longrightarrow \text{CO}_2(\text{aq}) + \text{O}_2^- + \text{CO}_2(\text{aq})$	2×10^9	0.0
A80	$\text{OH(aq)} + \text{CHOH}_2\text{CHOH}_2(\text{aq}) \longrightarrow \text{COH}_2\text{CHOH}_2(\text{aq}) + [\text{H}_2\text{O}](\text{aq})$	1.1×10^9	-1516.0
A81	$\text{COH}_2\text{CHOH}_2(\text{aq}) + \text{O}_2(\text{aq}) \longrightarrow \text{aO}_2\text{COH}_2\text{CHOH}_2(\text{aq})$	1.38×10^9	0.0
A82	$\text{O}_2\text{COH}_2\text{CHOH}_2(\text{aq}) \longrightarrow \text{HO}_2(\text{aq}) + \text{CHOH}_2\text{COOH(aq)}$	2×10^9	0.0
A83	$\text{HO(aq)} + \text{CHOH}_2\text{COOH(aq)} \longrightarrow \text{COH}_2\text{COOH(aq)} + [\text{H}_2\text{O}](\text{aq})$	1.1×10^9	-1516.0
A84	$\text{COH}_2\text{COOH(aq)} + \text{O}_2(\text{aq}) \longrightarrow \text{O}_2\text{COH}_2\text{COOH(aq)}$	2.0×10^9	0.0
A85	$\text{O}_2\text{COH}_2\text{COOH(aq)} \longrightarrow \text{HO}_2(\text{aq}) + \text{H}_2\text{C}_2\text{O}_4(\text{aq})$	2.0×10^9	0.0
A86	$\text{CH}_3\text{COH}_2(\text{aq}) + \text{O}_2(\text{aq}) \longrightarrow \text{CH}_3\text{COH}_2\text{OO(aq)}$	2.0×10^9	0.0
A87	$\text{CH}_3\text{COH}_2\text{OO(aq)} \longrightarrow \text{H}^+ + \text{H}^+ + \text{MCOO}^- + \text{O}_2^-$	1.0×10^5	0.0
A88	$\text{CH}_3\text{O(aq)} \longrightarrow \text{CH}_2\text{OH(aq)}$	1.0×10^6	0.0
A89	$\text{CH}_2\text{COO}^- + \text{O}_2(\text{aq}) \longrightarrow \text{O}_2\text{CH}_2\text{COO}^-$	2.0×10^9	0.0
A90	$\text{O}_2\text{CH}_2\text{COO}^- + \text{O}_2\text{CH}_2\text{COO}^- \longrightarrow 2 \text{CHOH}_2\text{COO}^- + \text{H}_2\text{O}_2(\text{aq})$	2.0×10^7	0.0
A91	$\text{CO}_2^- + \text{O}_2(\text{aq}) \longrightarrow \text{CO}_2(\text{aq}) + \text{O}_2^-$	4.0×10^9	0.0
A92	$\text{Cl}_2^- + \text{FE}^{2+} \longrightarrow 2 \text{Cl}^- + \text{FE}^{3+}$	1.0×10^7	-3030.0
A93	$\text{Cl}_2^- + \text{HO}_2(\text{aq}) \longrightarrow 2 \text{Cl}^- + \text{H}^+ + \text{O}_2(\text{aq})$	1.3×10^{10}	0.0
A94	$\text{Cl}_2^- + \text{HSO}_3^- \longrightarrow 2 \text{Cl}^- + \text{H}^+ + \text{SO}_3^-$	1.7×10^8	-400.0
A95	$\text{Cl}_2(\text{aq}) + [\text{H}_2\text{O}](\text{aq}) \longrightarrow \text{H}^+ + \text{Cl}^- + \text{HOCL(aq)}$	0.4	-7900.0
A96	$\text{Cl}_2^- + [\text{H}_2\text{O}](\text{aq}) \longrightarrow \text{H}^+ + \text{Cl}^- + \text{Cl}^- + \text{HO(aq)}$	23.4	0.0
A97	$\text{Br}^- + \text{SO}_4^- \longrightarrow \text{SO}_4^{2-} + \text{Br}(\text{aq})$	2.1×10^9	0.0
A98	$\text{Br}^- + \text{NO}_3(\text{aq}) \longrightarrow \text{NO}_3^- + \text{Br}(\text{aq})$	3.8×10^9	0.0
A99	$\text{Br}_2^- + \text{Br}_2^- \longrightarrow \text{Br}_2(\text{aq}) + 2 \text{Br}$	1.7×10^9	0.0
A100	$\text{Br}_2^- + \text{FE}^{2+} \longrightarrow 2 \text{Br}^- + \text{FE}^{3+}$	3.6×10^6	-3330.0
A101	$\text{Br}_2^- + \text{H}_2\text{O}_2(\text{aq}) \longrightarrow 2 \text{Br}^- + \text{H}^+ + \text{HO}_2(\text{aq})$	1.0×10^5	0.0
A102	$\text{Br}_2^- + \text{HO}_2(\text{aq}) \longrightarrow 2 \text{BR}^- + \text{O}_2(\text{aq}) + \text{H}^+$	6.5×10^9	0.0
A103	$\text{Br}_2^- + \text{HSO}_3^- \longrightarrow 2 \text{BR}^- + \text{H}^+ + \text{SO}_3^-$	5.0×10^7	-780.0
A104	$\text{Br}_2(\text{aq}) + [\text{H}_2\text{O}](\text{aq}) \longrightarrow \text{H}^+ + \text{Br}^- + \text{HOBr(aq)}$	0.031	-7500.0
A105	$\text{BrOH}^- \longrightarrow \text{Br}(\text{aq}) + \text{OH}^-$	4.2×10^6	0.0

Table A.3: Equilibrium reactions

Aqueous equilibria	Reaction	K_{298} ($M^{-n} s^{-1}$)	$-\Delta(H)/R$ (K)
D1	$H_2O(aq) \rightleftharpoons OH^- + H^+$	1.8×10^{-16}	-6800.0
D2	$CO_2(aq) \rightleftharpoons HCO_3^- + H^+$	4.3×10^{-7}	-913.0
D3	$NH_3(aq) + H_2O \rightleftharpoons NH_4^+ + OH^-$	3.17×10^{-7}	-560.0
D4	$HO_2(aq) \rightleftharpoons O_2^- + H^+$	1.6×10^{-5}	5.0×10^{10}
D5	$HONO(aq) \rightleftharpoons NO_2^- + H^+$	5.3×10^{-4}	-1760.0
D6	$HNO_4(aq) \rightleftharpoons NO_4^- + H^+$	1×10^{-5}	5×10^{10}
D7	$NO_2(aq) + HO_2(aq) \rightleftharpoons HNO_4(aq)$	2.2×10^9	4.6×10^{-3}
D8	$SO_2(aq) + H_2O \rightleftharpoons HSO_3^- + H^+$	3.13×10^{-4}	1940.0
D9	$HSO_3^- \rightleftharpoons SO_3^{2-} + H^+$	6.22×10^{-8}	1960.0
D10	$HSO_4^- \rightleftharpoons H^+ + SO_4^{2-}$	1.02×10^{-2}	2700.0
D11	$ORA1(aq) \rightleftharpoons H^+ + HCOO^-$	1.77×10^{-4}	12.0
D12	$ORA2(aq) \rightleftharpoons H^+ + MCOO^-$	1.75×10^{-5}	46.0
D13	$FE^{3+} + [H_2O](aq) \rightleftharpoons FEOH^{2+} + H^+$	1.1×10^{-4}	4.3×10^8
D14	$HCHO(aq) + [H_2O](aq) \rightleftharpoons CH_2OH_2(aq)$	36.0	4030.0
D15	$ALD(aq) + [H_2O](aq) = CH_3CHOH_2(aq)$	2.46×10^{-2}	2500.0
D16	$HSO_3^- + HCHO(aq) \rightleftharpoons HMS^-$	790.0	-3293.0
D17	$HMS^- \rightleftharpoons HSO_3^- + HCHO(aq)$	1.197×10^{-7}	-5831.0
D18	$SO_3^{2-} + HCHO(aq) \rightleftharpoons HMS^- + OH^- - [H_2O](aq)$	2.5×10^7	-2752.0
D19	$HMS \rightleftharpoons HCHO(aq) + SO_3^{2-} + H^+$	3.79×10^{-3}	-5290.0
D20	$Cl(aq) + Cl^- \rightleftharpoons Cl_2^-$	1.4×10^5	6×10^4
D21	$Br + Br^- \rightleftharpoons Br_2^-$	6.32×10^5	1.9×10^4
D22	$Cl^- + HO(aq) \rightleftharpoons ClOH^-$	0.7	6.1×10^9
D23	$ClOH^- + H^+ \rightleftharpoons Cl(aq) + [H_2O](aq)$	5.1×10^6	4100.0
D24	$Br^- + HO(aq) \rightleftharpoons BrOH^-$	333.0	3.3×10^7
D25	$BrOH^- + H^+ \rightleftharpoons Br(aq) + [H_2O](aq)$	1.8×10^{12}	2.45×10^{-2}
D26	$HO_3(aq) \rightleftharpoons H^+ + O_3^-$	6.3×10^{-9}	5.2×10^{10}
D27	$CHOHSO_3^- \rightleftharpoons CHOSO_3^{2-} + H^+$	1.34×10^{-6}	4.4×10^{10}
D28	$SO_5O_2H^- \rightleftharpoons H^+ + SO_5O_2^{2-}$	1.5×10^{-5}	5.0×10^{10}
D29	$HC_2O_4m = C_2O_4mm + Hp <=>$	6.25×10^{-5}	5.0×10^{10}
D30	$H_2C_2O_4(aq) \rightleftharpoons HC_2O_4^- + H^+$	6.4×10^{-2}	5.0×10^{10}
D31	$CHOH_2COOH(aq) \rightleftharpoons H^+ + CHOH_2COO^-$	3.16×10^{-4}	2.0×10^{10}
D32	$GLY(aq) + [H_2O](aq) \rightleftharpoons CHOH_2CHOH_2(aq)$	3900.0	5.5×10^{-3}
D33	$FE^{3+} + C_2O_4^{2-} = FEC_2O_4^+$	2.9×10^9	3.0×10^{-3}
D34	$FEC_2O_4^+ + C_2O_4^{2-} \rightleftharpoons FEC_2(O_4)_2^-$	6.3×10^6	3.0×10^{-3}
D35	$SO_4^- + CL^- \rightleftharpoons SO_4^{2-} + CL(aq)$	1.2	2.1×10^8
D36	$NO_3(aq) + CL^- \rightleftharpoons NO_3^- + CL(aq)$	3.4	-4300
D37	$CH_3CO(aq) + [H_2O](aq) \rightleftharpoons CH_3COH_2(aq)$	367.0	0.0
D38	$ACO_3(aq) \rightleftharpoons H^+ + O_2CH_2COO^-$	1.75×10^{-5}	46.0
D39	$Na^+ + Na_C^+ \rightleftharpoons Na^+ + Na_C^+$	0.0	0.0

Appendix B

Appendix to Chapter 3

Table B.1: Thermodynamic and kinetic data for a subset of CAPRAM 2.4 mechanism

Henry's Law	Equilibrium	K_{298}^* (M atm $^{-1}$)	$-\Delta H/R$ (K)
H1	$\text{CO}_2(\text{g}) \rightleftharpoons \text{CO}_2(\text{aq})$	3.1×10^{-2}	2423
H2	$\text{O}_3(\text{g}) \rightleftharpoons \text{O}_3(\text{aq})$	1.14×10^{-2}	2300
H3	$\text{HO}_2(\text{g}) \rightleftharpoons \text{HO}_2(\text{aq})$	1.14×10^{-2}	2300
H4	$\text{OH}(\text{g}) \rightleftharpoons \text{OH}(\text{aq})$	9×10^3	0
H5	$\text{H}_2\text{O}_2(\text{g}) \rightleftharpoons \text{H}_2\text{O}_2(\text{aq})$	1.02×10^5	6340
H6	$\text{NO}_2(\text{g}) \rightleftharpoons \text{NO}_2(\text{aq})$	1.2×10^{-2}	1263
H7	$\text{HNO}_3(\text{g}) \rightleftharpoons \text{NO}_3^- + \text{H}^+$	4.62×10^6	10500
H8	$\text{NO}_3(\text{g}) \rightleftharpoons \text{NO}_3(\text{aq})$	6×10^{-1}	0
H9	$\text{N}_2\text{O}_5(\text{g}) \rightleftharpoons \text{N}_2\text{O}_5(\text{aq})$	1.4×10^0	0
H10	$\text{NH}_3(\text{g}) \rightleftharpoons \text{NH}_3(\text{aq})$	60.7	3920
H11	$\text{HCl}(\text{g}) \rightleftharpoons \text{CL}^- + \text{H}^+$	1.89×10^6	8910
H12	$\text{SO}_2(\text{g}) \rightleftharpoons \text{SO}_2(\text{aq})$	1.24	3247
H13	$\text{SULF}(\text{g}) \rightleftharpoons \text{HSO}_4^- + \text{H}^+$	8.7×10^{14}	0
H14	$\text{HNO}_4(\text{g}) \rightleftharpoons \text{HNO}_4(\text{aq})$	3×10^4	0
H15	$\text{O}_2(\text{g}) \rightleftharpoons \text{O}_2(\text{aq})$	1.3×10^{-3}	1700
H16	$\text{NO}(\text{g}) \rightleftharpoons \text{NO}(\text{aq})$	1.9×10^{-3}	0
Aqueous equilibria		K (M)	$-\Delta H/R$ (K)
D1	$\text{H}_2\text{O}(\text{aq}) \rightleftharpoons \text{OH}^- + \text{H}^+$	1.8×10^{-16}	-6800
D2	$\text{CO}_2(\text{aq}) \rightleftharpoons \text{HCO}_3^- + \text{H}^+$	1.72×10^6	-913
D3	$\text{NH}_3(\text{aq}) + \text{H}_2\text{O}(\text{aq}) \rightleftharpoons \text{NH}_4^+ + \text{OH}^-$	3.17×10^{-7}	-560
D4	$\text{HO}_2(\text{aq}) \rightleftharpoons \text{O}_2^- + \text{H}^+$	3.17×10^{-7}	5.0×10^{10}

Continued

Table B.1: Thermodynamic and kinetic data for a subset of CAPRAM 2.4 mechanism (Continued)

Aqueous equilibria	Reaction	K (M)	$-\Delta H/R$ (K)
D5	$\text{HNO}_4(\text{aq}) \rightleftharpoons \text{NO}_4^- + \text{H}^+$	1×10^5	5.0×10^{10}
D6	$\text{NO}_2(\text{aq}) + \text{HO}_2(\text{aq}) \rightleftharpoons \text{HNO}_4(\text{aq})$	2.2×10^9	4.6×10^{-3}
D7	$\text{SO}_2(\text{aq}) + \text{H}_2\text{O}(\text{aq}) \rightleftharpoons \text{HSO}_3^- + \text{H}^+$	3.13×10^{-4}	1940
D8	$\text{HSO}_3^- \rightleftharpoons \text{SO}_3^{2-} + \text{H}^+$	6.22×10^{-8}	1960
D9	$\text{HSO}_4^- \rightleftharpoons \text{H}^+ + \text{SO}_4^{2-}$	1.02×10^{-2}	2700
Aqueous chemistry	Reaction	K_{298} (M $^{-n}$ s $^{-1}$)	$-E/R$ (K)
A1	$\text{H}_2\text{O}_2(\text{aq}) + \text{OH}(\text{aq}) \longrightarrow \text{HO}_2(\text{aq}) + \text{H}_2\text{O}$	3.0×10^7	-1680
A2	$\text{HSO}_3^- + \text{OH}(\text{aq}) \longrightarrow \text{SO}_3^- + \text{H}_2\text{O}$	2.7×10^9	0
A3	$\text{N}_2\text{O}_5(\text{aq}) \longrightarrow \text{NO}_3^- + \text{NO}_2^+$	1.0×10^9	0
A4	$\text{NO}_2^+ + \text{H}_2\text{O}(\text{aq}) \longrightarrow \text{NO}_3^- + \text{H}^+ + \text{H}^+$	8.9×10^7	0
A5	$\text{NO}_3(\text{aq}) + \text{HSO}_3^- \longrightarrow \text{NO}_3^- + \text{H}^+ + \text{SO}_3^-$	1.3×10^9	-2000
A6	$\text{NO}_3(\text{aq}) + \text{SO}_4^{2-} \longrightarrow \text{NO}_3^- + \text{SO}_4^-$	1.0×10^5	0
A7	$\text{NO}_4^- \longrightarrow \text{NO}_2^- + \text{O}_2(\text{aq})$	4.5×10^{-2}	0
A8	$\text{HNO}_4(\text{aq}) + \text{HSO}_3^- \longrightarrow \text{HSO}_4^- + \text{H}^+ + \text{NO}_3^-$	3.3×10^5	0
A9	$\text{HSO}_3^- + \text{H}_2\text{O}_2(\text{aq}) + \text{H}^+ \longrightarrow \text{SO}_4^{2-} + 2\text{H}^+ + \text{H}_2\text{O}$	7.2×10^7	-4000
A10	$\text{HSO}_3^- + \text{O}_3(\text{aq}) \longrightarrow \text{SO}_4^{2-} + \text{H}^+ + \text{O}_2(\text{aq})$	3.7×10^5	-5530
A11	$\text{SO}_3^{2-} + \text{O}_3(\text{aq}) \longrightarrow \text{SO}_4^{2-} + \text{O}_2(\text{aq})$	1.5×10^9	-5280
A12	$\text{SO}_5^- + \text{SO}_5^- \longrightarrow \text{SO}_4^- + \text{SO}_4^- + \text{O}_2(\text{aq})$	2.2×10^8	-2600
A13	$\text{SO}_5^- + \text{HO}_2(\text{aq}) \longrightarrow \text{SO}_5\text{O}_2\text{H}^-$	1.7×10^9	0
A14	$\text{SO}_3^- + \text{O}_2(\text{aq}) \longrightarrow \text{SO}_5^-$	2.5×10^9	0
A15	$\text{SO}_4^- + \text{H}_2\text{O}(\text{aq}) \longrightarrow \text{SO}_4^{2-} + \text{OH}(\text{aq}) + \text{H}^+$	11	-1110
A16	$\text{HSO}_5^- + \text{HSO}_3^- + \text{H}^+ \longrightarrow 2\text{SO}_4^{2-} + 3\text{H}^+$	7.14×10^6	0

*: Note that Henry's Law partitioning is treated kinetically with an uptake rate constant calculated as in equation 1 of Ervens et al. (2003), and then using the equilibrium constant to calculate the evaporation rate constant.

References

- Adams, P. J. and Seinfeld, J. H.: Predicting global aerosol size distributions in general circulation models, *Journal of Geophysical Research: Atmospheres*, 107, AAC–4, 2002.
- Ahmad, I., Mielonen, T., Grosvenor, D. P., Portin, H. J., Arola, A., Mikkonen, S., Kühn, T., Leskinen, A., Joutsensaari, J., Komppula, M., et al.: Long-term measurements of cloud droplet concentrations and aerosol–cloud interactions in continental boundary layer clouds, *Tellus B: Chemical and Physical Meteorology*, 65, 20138, 2013.
- Alexander, B., Hastings, M., Allman, D., Dachs, J., Thornton, J., and Kunasek, S.: Quantifying atmospheric nitrate formation pathways based on a global model of the oxygen isotopic composition ($\Delta^{17}\text{O}$) of atmospheric nitrate, *Atmospheric Chemistry and Physics*, 9, 5043–5056, 2009a.
- Alexander, B., Park, R. J., Jacob, D. J., and Gong, S.: Transition metal-catalyzed oxidation of atmospheric sulfur: Global implications for the sulfur budget, *Journal of Geophysical Research: Atmospheres*, 114, 1–13, [https://doi.org/https://doi.org/10.1029/2008JD010486](https://doi.org/10.1029/2008JD010486), 2009b.
- Alexander, B., Park, R. J., Jacob, D. J., and Gong, S.: Transition metal-catalyzed oxidation of atmospheric sulfur: Global implications for the sulfur budget, *Journal of Geophysical Research: Atmospheres*, 114, 2009c.
- Alexander, B., Allman, D., Amos, H., Fairlie, T., Dachs, J., Hegg, D. A., and Sletten, R. S.: Isotopic constraints on the formation pathways of sulfate aerosol in the marine boundary layer of the subtropical northeast Atlantic Ocean, *Journal of Geophysical Research: Atmospheres*, 117, 2012.
- Andrejczuk, M., Reisner, J., Henson, B., Dubey, M., and Jeffry, C.: The potential impacts of pollution on a nondrizzling stratus deck: Does aerosol number matter more than type?, *Journal of Geophysical Research: Atmospheres*, 113, D19 204, [https://doi.org/https://doi.org/10.1029/2007JD009445](https://doi.org/10.1029/2007JD009445), 2008.
- Anenberg, S. C., Horowitz, L. W., Tong, D. Q., and West, J. J.: An estimate of the global burden of anthropogenic ozone and fine particulate matter on premature human mortality using atmospheric modeling, *Environmental health perspectives*, 118, 1189–1195, 2010.
- Appel, K. W., Napelenok, S. L., Foley, K. M., Pye, H. O., Hogrefe, C., Luecken, D. J., Bash, J. O., Roselle, S. J., Pleim, J. E., Foroutan, H., Hutzell, W. T., Pouliot, G. A., Sarwar, G., Fahey, K. M., Gantt, B., Gilliam, R. C., Heath, N. K., Kang, D., Mathur, R., Schwede, D. B., Spero, T. L., Wong, D. C., and Young, J. O.: Description and evaluation of the Community Multiscale Air Quality (CMAQ) modeling system version 5.1, *Geoscientific Model Development*, 10, 1703–1732, <https://doi.org/10.5194/gmd-10-1703-2017>, 2017.
- Barth, M. C.: The importance of cloud drop representation on cloud photochemistry, *Atmospheric Research*, 82, 294–309, <https://doi.org/https://doi.org/10.1016/j.atmosres.2005.10.008>, 2006a.
- Barth, M. C.: The importance of cloud drop representation on cloud photochemistry, *Atmospheric Research*, 82, 294–309, 2006b.
- Barth, M. C., Sillman, S., Hudman, R., Jacobson, M. Z., Kim, C. H., Monod, A., and Liang, J.: Summary of the cloud chemistry modeling intercomparison: Photochemical box model simulation, *Journal of Geophysical Research: Atmospheres*, 108, <https://doi.org/https://doi.org/10.1029/2002jd002673>, 2003.

- Bauer, S., Wright, D., Koch, D., Lewis, E., McGraw, R., Chang, L.-S., Schwartz, S., and Ruedy, R.: MATRIX (Multi-configuration Aerosol TRacker of mIXing state): an aerosol microphysical module for global atmospheric models, *Atmospheric Chemistry and Physics*, 8, 6003–6035, [https://doi.org/https://doi.org/10.5194/acp-8-6003-2008](https://doi.org/10.5194/acp-8-6003-2008), 2008.
- Bell, M. L., Dominici, F., Ebisu, K., Zeger, S. L., and Samet, J. M.: Spatial and temporal variation in PM_{2.5} chemical composition in the United States for health effects studies, *Environmental health perspectives*, 115, 989–995, 2007.
- Bellouin, N., Boucher, O., Haywood, J., and Reddy, M. S.: Global estimate of aerosol direct radiative forcing from satellite measurements, *Nature*, 438, 1138–1141, 2005.
- Bellouin, N., Quaas, J., Gryspeerdt, E., Kinne, S., Stier, P., Watson-Parris, D., Boucher, O., Carslaw, K. S., Christensen, M., Daniau, A.-L., et al.: Bounding global aerosol radiative forcing of climate change, *Reviews of Geophysics*, 58, e2019RG000660, 2020.
- Bhattu, D. and Tripathi, S. N.: CCN closure study: Effects of aerosol chemical composition and mixing state, *Journal of Geophysical Research: Atmospheres*, 120, 766–783, [https://doi.org/https://doi.org/10.1002/2014JD021978](https://doi.org/10.1002/2014JD021978), 2015.
- Binkowski, F. S. and Roselle, S. J.: Models-3 Community Multiscale Air Quality (CMAQ) model aerosol component 1. Model description, *Journal of geophysical research: Atmospheres*, 108, 2003.
- Binkowski, F. S., Arunachalam, S., Adelman, Z., and Pinto, J. P.: Examining photolysis rates with a prototype online photolysis module in CMAQ, *Journal of Applied Meteorology and Climatology*, 46, 1252–1256, <https://doi.org/10.1175/JAM2531.1>, 2007.
- Bond, T. C. and Bergstrom, R. W.: Light absorption by carbonaceous particles: An investigative review, *Aerosol Science and Technology*, 40, 27–67, <https://doi.org/10.1080/02786820500421521>, 2006.
- Bond, T. C., Habib, G., and Bergstrom, R. W.: Limitations in the enhancement of visible light absorption due to mixing state, *Journal of Geophysical Research Atmospheres*, 111, 1–13, <https://doi.org/10.1029/2006JD007315>, 2006.
- Bond, T. C., Bhardwaj, E., Dong, R., Jogani, R., Jung, S., Roden, C., Streets, D. G., and Trautmann, N. M.: Historical emissions of black and organic carbon aerosol from energy-related combustion, 1850–2000, *Global biogeochemical cycles*, 21, 2007.
- Bond, T. C., Doherty, S. J., Fahey, D. W., Forster, P. M., Berntsen, T., DeAngelo, B. J., Flanner, M. G., Ghan, S., Kärcher, B., Koch, D., et al.: Bounding the role of black carbon in the climate system: A scientific assessment, *Journal of geophysical research: Atmospheres*, 118, 5380–5552, 2013.
- Bondy, A. L., Bonanno, D., Moffet, R. C., Wang, B., Laskin, A., and Ault, A. P.: The diverse chemical mixing state of aerosol particles in the southeastern United States, *Atmospheric Chemistry and Physics*, 18, 12 595–12 612, [https://doi.org/https://doi.org/10.5194/acp-18-12595-2018](https://doi.org/10.5194/acp-18-12595-2018), 2018.
- Bott, A., Trautmann, T., and Zdunkowski, W.: A numerical model of the cloud-topped planetary boundary layer: Radiation, turbulence and spectral microphysics in marine stratus, *Quarterly Journal of the Royal Meteorological Society*, 122, 635–667, [https://doi.org/https://doi.org/10.1002/qj.49712253105](https://doi.org/10.1002/qj.49712253105), 1996.
- Boucher, O., Randall, D., Artaxo, P., Bretherton, C., Feingold, G., Forster, P., Kerminen, V.-M., Kondo, Y., Liao, H., Lohmann, U., Rasch, P., Satheesh, S., Sherwood, S., Stevens, B., and Zhang, X.: Clouds and Aerosols, book section 7, p. 571–658, Cambridge University Press, Cambridge, United Kingdom and New York, NY, USA, <https://doi.org/10.1017/CBO9781107415324.016>, URL www.climatechange2013.org, 2013.
- Bower, K., Jones, A., and Choularton, T.: A modelling study of aerosol processing by stratocumulus clouds and its impact on general circulation model parameterisations of cloud and aerosol, *Atmospheric research*, 50, 317–344, 1999.
- Brenguier, J.-L., Burnet, F., and Geoffroy, O.: Cloud optical thickness and liquid water path—does the k coefficient vary with droplet concentration?, *Atmospheric Chemistry and Physics*, 11, 9771–9786, 2011.

Broekhuizen, K., Chang, R.-W., Leaitch, W., Li, S.-M., and Abbatt, J.: Closure between measured and modeled cloud condensation nuclei (CCN) using size-resolved aerosol compositions in downtown Toronto, *Atmospheric Chemistry and Physics*, 6, 2513–2524, 2006a.

Broekhuizen, K., Chang, R. Y., Leaitch, W. R., Li, S., and Abbatt, J. P. D.: Closure between measured and modeled cloud condensation nuclei (CCN) using size-resolved aerosol compositions in downtown Toronto, *Atmospheric Chemistry and Physics*, 6, 2513–2524, [https://doi.org/https://doi.org/10.5194/acp-6-2513-2006](https://doi.org/10.5194/acp-6-2513-2006), 2006b.

Burgos, M., Andrews, E., Titos, G., Benedetti, A., Bian, H., Buchard, V., Curci, G., Kirkevåg, A., Kokkola, H., Laakso, A., Lund, M., Matsui, H., Myhre, G., Randles, C., Schulz, M., van Noije, T., Zhang, K., Alados-Arboledas, L., Baltensperger, U., Jefferson, A., Sherman, J., Sun, J., Weingartner, E., and Zieger, P.: A global model-measurement evaluation of particle light scattering coefficients at elevated relative humidity, *Atmospheric Chemistry and Physics Discussions*, pp. 1–30, <https://doi.org/10.5194/acp-2019-1190>, 2020.

Bzdek, B. R., Pennington, M. R., and Johnston, M. V.: Single particle chemical analysis of ambient ultrafine aerosol: A review, *Journal of Aerosol Science*, 52, 109–120, 2012.

Cappa, C. D., Zhang, X., Russell, L. M., Collier, S., Lee, A. K., Chen, C.-L., Betha, R., Chen, S., Liu, J., Price, D. J., et al.: Light absorption by ambient black and brown carbon and its dependence on black carbon coating state for two California, USA, cities in winter and summer, *Journal of Geophysical Research: Atmospheres*, 124, 1550–1577, 2019.

Charlson, R. J., Schwartz, S., Hales, J., Cess, R. D., Coakley, J. J., Hansen, J., and Hofmann, D.: Climate forcing by anthropogenic aerosols, *Science*, 255, 423–430, 1992.

Cheung, K., Ntziachristos, L., Tzamkiozis, T., Schauer, J., Samaras, Z., Moore, K., and Sioutas, C.: Emissions of particulate trace elements, metals and organic species from gasoline, diesel, and biodiesel passenger vehicles and their relation to oxidative potential, *Aerosol Science and Technology*, 44, 500–513, 2010.

Chin, M., Rood, R. B., Lin, S.-J., Müller, J.-F., and Thompson, A. M.: Atmospheric sulfur cycle simulated in the global model GOCART: Model description and global properties, *Journal of Geophysical Research: Atmospheres*, 105, 24 671–24 687, 2000.

China, S., Mazzoleni, C., Gorkowski, K., Aiken, A. C., and Dubey, M. K.: Morphology and mixing state of individual freshly emitted wildfire carbonaceous particles, *Nature communications*, 4, 1–7, 2013.

China, S., Scarnato, B., Owen, R. C., Zhang, B., Ampadu, M. T., Kumar, S., Dzepina, K., Dziobak, M. P., Fialho, P., Perlinger, J. A., et al.: Morphology and mixing state of aged soot particles at a remote marine free troposphere site: Implications for optical properties, *Geophysical Research Letters*, 42, 1243–1250, 2015.

Ching, J. and Kajino, M.: Aerosol Mixing State Matters for Particles Deposition in Human Respiratory System, *SCIENTIFIC REPORTS*, 8, 8864, [https://doi.org/https://doi.org/10.1038/s41598-018-27156-z](https://doi.org/10.1038/s41598-018-27156-z), 2018.

Ching, J., Riemer, N., and West, M.: Impacts of black carbon mixing state on black carbon nucleation scavenging: Insights from a particle-resolved model, *Journal of Geophysical Research: Atmospheres*, 117, 2012.

Ching, J., Riemer, N., and West, M.: Black carbon mixing state impacts on cloud microphysical properties: Effects of aerosol plume and environmental conditions, *Journal of Geophysical Research: Atmospheres*, pp. 5990–6013, [https://doi.org/https://doi.org/10.1002/2016JD024851](https://doi.org/10.1002/2016JD024851), 2016a.

Ching, J., Zaveri, R. A., Easter, R. C., Riemer, N., and Fast, J. D.: A three-dimensional sectional representation of aerosol mixing state for simulating optical properties and cloud condensation nuclei, *Journal of Geophysical Research: Atmospheres*, 121, 5912–5929, 2016b.

Ching, J., Fast, J., West, M., and Riemer, N.: Metrics to quantify the importance of mixing state for CCN activity, *Atmospheric Chemistry and Physics*, 17, 7445–7458, [https://doi.org/https://doi.org/10.5194/acp-17-7445-2017](https://doi.org/10.5194/acp-17-7445-2017), 2017.

Ching, J., Adachi, K., Zaizen, Y., Igarashi, Y., and Kajino, M.: Aerosol Mixing State Revealed by Transmission Electron Microscopy Pertaining to Cloud Formation and Human Airway Deposition, *npj Clim Atmos Sci*, 2, 22, [https://doi.org/https://doi.org/10.1038/s41612-019-0081-9](https://doi.org/10.1038/s41612-019-0081-9), 2019.

- Choularton, T., Bower, K., and Gallagher, M.: The effect of sulphur chemistry on the scattering properties of particles, *Philosophical Transactions of the Royal Society of London. Series B: Biological Sciences*, 352, 213–220, 1997.
- Christiansen, A. E., Carlton, A. G., and Henderson, B. H.: Differences in fine particle chemical composition on clear and cloudy days, *Atmospheric Chemistry and Physics*, 20, 11 607–11 624, <https://doi.org/10.5194/acp-20-11607-2020>, 2020.
- Chuang, P. Y., Charlson, R. J., and Seinfeld, J. H.: Kinetic limitations on droplet formation in clouds, *Nature*, 390, 594–596, [https://doi.org/https://doi.org/10.1038/37576](https://doi.org/10.1038/37576), 1997.
- Cohen, S. D., Hindmarsh, A. C., and Dubois, P. F.: CVODE, A Stiff/Nonstiff ODE Solver in C, *Computers in Physics*, 10, [https://doi.org/https://doi.org/doi:10.1063/1.4822377](https://doi.org/10.1063/1.4822377), 1996.
- Collett, J., Bator, A., Rao, X., and Demoz, B. B.: Acidity variations across the cloud drop size spectrum and their influence on rates of atmospheric sulfate production, *Geophysical Research Letters*, 21, 2393–2396, [https://doi.org/https://doi.org/10.1029/94GL02480](https://doi.org/10.1029/94GL02480), 1994.
- Cooper, W., Bruintjes, R., and Mather, G.: Calculations pertaining to hygroscopic seeding with flares, *Journal of Applied Meteorology*, 36, 1449–1469, 1997.
- Corbin, J. C., Pieber, S. M., Czech, H., Zanatta, M., Jakobi, G., Massabò, D., Orasche, J., El Haddad, I., Mensah, A. A., Stengel, B., et al.: Brown and black carbon emitted by a marine engine operated on heavy fuel oil and distillate fuels: Optical properties, size distributions, and emission factors, *Journal of Geophysical Research: Atmospheres*, 123, 6175–6195, 2018.
- Cotton, W. R., Bryan, G., and Van den Heever, S. C.: *Storm and cloud dynamics*, Academic press, 2010.
- Crooks, M., Connolly, P., and McFiggans, G.: A parameterisation for the co-condensation of semi-volatile organics into multiple aerosol particle modes, *Geoscientific Model Development*, 11, 3261–3278, 2018.
- Curci, G., Hogrefe, C., Bianconi, R., Im, U., Balzarini, A., Baró, R., Brunner, D., Forkel, R., Giordano, L., Hirtl, M., Honzak, L., Jiménez-Guerrero, P., Knote, C., Langer, M., Makar, P. A., Pirovano, G., Pérez, J. L., San José, R., Syrakov, D., Tuccella, P., Werhahn, J., Wolke, R., Žabkar, R., Zhang, J., and Galmarini, S.: Uncertainties of simulated aerosol optical properties induced by assumptions on aerosol physical and chemical properties: An AQMEII-2 perspective, *Atmospheric Environment*, 115, 541–552, <https://doi.org/10.1016/j.atmosenv.2014.09.009>, 2015.
- Curtis, D. B., Meland, B., Aycibin, M., Arnold, N. P., Grassian, V. H., Young, M. A., and Kleiber, P. D.: A laboratory investigation of light scattering from representative components of mineral dust aerosol at a wavelength of 550 nm, *Journal of Geophysical Research: Atmospheres*, 113, 2008.
- Curtis, J. H., Riemer, N., and West, M.: A single-column particle-resolved model for simulating the vertical distribution of aerosol mixing state: WRF-PartMC-MOSAIC-SCM v1. 0, *Geoscientific Model Development*, 10, 4057–4079, 2017.
- Deguillaume, L., Leriche, M., Monod, A., and Chaumerliac, N.: The role of transition metal ions on HO x radicals in clouds: a numerical evaluation of its impact on multiphase chemistry, *Atmospheric Chemistry and Physics*, 4, 95–110, 2004.
- Deguillaume, L., Leriche, M., Desboeufs, K., Mailhot, G., George, C., and Chaumerliac, N.: Transition Metals in Atmospheric Liquid Phases : Sources , Reactivity , and Sensitive Parameters, *Chemical Reviews*, pp. 3388–3431, [https://doi.org/https://doi.org/10.1021/cr040649c](https://doi.org/10.1021/cr040649c), 2005.
- Desboeufs, K., Sofikitis, A., Losno, R., Colin, J., and Ausset, P.: Dissolution and solubility of trace metals from natural and anthropogenic aerosol particulate matter, *Chemosphere*, 58, 195–203, 2005.
- Ditas, F., Shaw, R. A., Siebert, H., Simmel, M., Wehner, B., and Wiedensohler, A.: Aerosols-cloud microphysics-thermodynamics-turbulence: evaluating supersaturation in a marine stratocumulus cloud, *Atmospheric Chemistry and Physics*, 12, 2459–2468, 2012.

Dockery, D. W., Pope, C. A., Xu, X., Spengler, J. D., Ware, J. H., Fay, M. E., Ferris Jr, B. G., and Speizer, F. E.: An association between air pollution and mortality in six US cities, *New England journal of medicine*, 329, 1753–1759, 1993.

Ervens, B.: CAPRAM 2.4 (MODAC mechanism): An extended and condensed tropospheric aqueous phase mechanism and its application, *Journal of Geophysical Research: Atmospheres*, 108, 4426, <https://doi.org/https://doi.org/10.1029/2002JD002202>, 2003.

Ervens, B.: Modeling the processing of aerosol and trace Gases in clouds and fogs, *Chemical Reviews*, 115, 4157–4198, <https://doi.org/https://doi.org/10.1021/cr5005887>, 2015a.

Ervens, B.: Modeling the processing of aerosol and trace gases in clouds and fogs, *Chemical reviews*, 115, 4157–4198, 2015b.

Ervens, B., George, C., Williams, J., Buxton, G., Salmon, G., Bydder, M., Wilkinson, F., Dentener, F., Mirabel, P., Wolke, R., et al.: CAPRAM 2.4 (MODAC mechanism): An extended and condensed tropospheric aqueous phase mechanism and its application, *Journal of Geophysical Research: Atmospheres*, 108, 2003.

Ervens, B., Cubison, M., Andrews, E., Feingold, G., Ogren, J., Jimenez, J., Quinn, P., Bates, T., Wang, J., Zhang, Q., et al.: CCN predictions using simplified assumptions of organic aerosol composition and mixing state: a synthesis from six different locations, *Atmospheric Chemistry and Physics*, 10, 4795–4807, 2010.

Ervens, B., Turpin, B., and Weber, R.: Secondary organic aerosol formation in cloud droplets and aqueous particles (aqSOA): a review of laboratory, field and model studies, *Atmospheric Chemistry and Physics*, 11, 11 069–11 102, 2011.

Esteve, A. R., Highwood, E. J., Morgan, W. T., Allen, G., Coe, H., Grainger, R. G., Brown, P., and Szpek, K.: A study on the sensitivities of simulated aerosol optical properties to composition and size distribution using airborne measurements, *Atmospheric Environment*, 89, 517–524, <https://doi.org/10.1016/j.atmosenv.2014.02.063>, 2014. URL <http://dx.doi.org/10.1016/j.atmosenv.2014.02.063>, 2014.

Fahey, K. M., Carlton, A. G., Pye, H. O., Baek, J., Hutzell, W. T., Stanier, C. O., Baker, K. R., Appel, K. W., Jaoui, M., and Offenberg, J. H.: A framework for expanding aqueous chemistry in the Community Multiscale Air Quality (CMAQ) model version 5.1, *Geoscientific model development*, 10, 1587–1605, 2017a.

Fahey, K. M., Carlton, A. G., Pye, H. O., Baek, J., Hutzell, W. T., Stanier, C. O., Baker, K. R., Wyat Appel, K., Jaoui, M., and Offenberg, J. H.: A framework for expanding aqueous chemistry in the Community Multiscale Air Quality (CMAQ) model version 5.1, *Geoscientific Model Development*, 10, 1587–1605, <https://doi.org/https://doi.org/10.5194/gmd-10-1587-2017>, 2017b.

Fan, J., Wang, Y., Rosenfeld, D., and Liu, X.: Review of aerosol–cloud interactions: Mechanisms, significance, and challenges, *Journal of the Atmospheric Sciences*, 73, 4221–4252, 2016.

Fann, N., Lamson, A. D., Anenberg, S. C., Wesson, K., Risley, D., and Hubbell, B. J.: Estimating the national public health burden associated with exposure to ambient PM_{2.5} and ozone, *Risk Analysis: An International Journal*, 32, 81–95, 2012.

Farmer, D. K., Cappa, C. D., and Kreidenweis, S. M.: Atmospheric Processes and Their Controlling Influence on Cloud Condensation Nuclei Activity, *Chemical Reviews*, 115, 4199–4217, <https://doi.org/https://doi.org/10.1021/cr5006292>, 2015.

Fast, J. D., Gustafson Jr, W. I., Easter, R. C., Zaveri, R. A., Barnard, J. C., Chapman, E. G., Grell, G. A., and Peckham, S. E.: Evolution of ozone, particulates, and aerosol direct radiative forcing in the vicinity of Houston using a fully coupled meteorology-chemistry-aerosol model, *Journal of Geophysical Research: Atmospheres*, 111, 2006.

Fast, J. D., Berg, L. K., Feng, Z., Mei, F., Newsom, R., Sakaguchi, K., and Xiao, H.: The impact of variable land-atmosphere coupling on convective cloud populations observed during the 2016 HI-SCALE field campaign, *Journal of Advances in Modeling Earth Systems*, 11, 2629–2654, 2019.

- Feichter, J. and Leisner, T.: Climate engineering: a critical review of approaches to modify the global energy balance, *The European Physical Journal Special Topics*, 176, 81–92, 2009.
- Feingold, G. and Kreidenweis, S.: Does cloud processing of aerosol enhance droplet concentrations?, *Journal of Geophysical Research: Atmospheres*, 105, 24 351–24 361, 2000.
- Feingold, G., Kreidenweis, S. M., Stevens, B., and Cotton, W.: Numerical simulations of stratocumulus processing of cloud condensation nuclei through collision coalescence, *Journal of Geophysical Research: Atmospheres*, 101, 21 391–21 402, [https://doi.org/10.1016/0169-8095\(94\)90063-9](https://doi.org/10.1016/0169-8095(94)90063-9), 1996.
- Fierce, L., Riemer, N., and Bond, T. C.: Explaining variance in black carbon's aging timescale, *Atmospheric Chemistry and Physics*, 15, 3173–3191, 2015.
- Fierce, L., Bond, T. C., Bauer, S. E., Mena, F., and Riemer, N.: Black carbon absorption at the global scale is affected by particle-scale diversity in composition, *Nature Communications*, 7, 1–8, <https://doi.org/10.1038/ncomms12361>, 2016.
- Fierce, L., Riemer, N., and Bond, T. C.: Toward reduced representation of mixing state for simulating aerosol effects on climate, *Bulletin of the American Meteorological Society*, 98, 971–980, <https://doi.org/10.1175/BAMS-D-16-0028.1>, 2017.
- Fierce, L., Onasch, T. B., Cappa, C. D., Mazzoleni, C., China, S., Bhandari, J., Davidovits, P., Al Fischer, D., Helgestad, T., Lambe, A. T., Sedlacek, A. J., Smith, G. D., and Wolff, L.: Radiative absorption enhancements by black carbon controlled by particle-to-particle heterogeneity in composition, *Proceedings of the National Academy of Sciences*, 117, 5196–5203, <https://doi.org/10.1073/pnas.1919723117>, 2020.
- Flossmann, A.: A 2-D spectral model simulation of the scavenging of gaseous and particulate sulfate by warm marine clouds, *ATMOSPHERIC RESEARCH*, 32, 233–248, [https://doi.org/10.1016/0169-8095\(94\)90063-9](https://doi.org/10.1016/0169-8095(94)90063-9), 1994.
- Friedlander, S., Koch, W., and Main, H.: Scavenging of a coagulating fine aerosol by a coarse particle mode, *Journal of Aerosol Science*, 22, 1–8, 1991.
- Fu, H., Zhang, M., Li, W., Chen, J., Wang, L., Quan, X., and Wang, W.: Morphology, composition and mixing state of individual carbonaceous aerosol in urban Shanghai, *Atmospheric Chemistry and Physics*, 12, 693–707, 2012.
- Fushimi, A., Hasegawa, S., Takahashi, K., Fujitani, Y., Tanabe, K., and Kobayashi, S.: Atmospheric fate of nucleimode particles estimated from the number concentrations and chemical composition of particles measured at roadside and background sites, *Atmospheric Environment*, 42, 949–959, 2008.
- Gao, W., Fan, J., Easter, R., Yang, Q., Zhao, C., and Ghan, S. J.: Coupling spectral-bin cloud microphysics with the MOSAIC aerosol model in WRF-Chem: Methodology and results for marine stratocumulus clouds, *Journal of Advances in Modeling Earth Systems*, 8, 1289–1309, 2016.
- Gaur, A., Tripathi, S., Kanawade, V., Tare, V., and Shukla, S.: Four-year measurements of trace gases (SO₂, NO_x, CO, and O₃) at an urban location, Kanpur, in northern India, *Journal of Atmospheric Chemistry*, 71, 283–301, 2014.
- Ge, X., Zhang, Q., Sun, Y., Ruehl, C. R., and Setyan, A.: Effect of aqueous-phase processing on aerosol chemistry and size distributions in Fresno, California, during wintertime, *Environmental Chemistry*, 9, 221–235, 2012.
- Grabowski, W. W., Morrison, H., Shima, S.-I., Abade, G. C., Dziekan, P., and Pawlowska, H.: Modeling of cloud microphysics: Can we do better?, *Bulletin of the American Meteorological Society*, 100, 655–672, <https://doi.org/10.1175/BAMS-D-18-0005.1>, 2019.
- Greenhalgh, T., Jimenez, J. L., Prather, K. A., Tufekci, Z., Fisman, D., and Schooley, R.: Ten scientific reasons in support of airborne transmission of SARS-CoV-2, *The Lancet*, 397, 1603–1605, 2021.
- Griffin, R. J.: The sources and impacts of tropospheric particulate matter, *Nature Education Knowledge*, 4, 1, 2013.

- Gustafsson, Ö. and Ramanathan, V.: Convergence on climate warming by black carbon aerosols, *Proceedings of the National Academy of Sciences*, 113, 4243–4245, 2016.
- Hall, D. W.: A detailed microphysical model within a two-dimensional dynamic framework: model description and preliminary results, *Journal of the Atmospheric Sciences*, 37, 2486–2507, [https://doi.org/10.1175/1520-0469\(1980\)037<2486:ADMMWA>2.0.CO;2](https://doi.org/10.1175/1520-0469(1980)037<2486:ADMMWA>2.0.CO;2), 1980.
- Harris, E., Sinha, B., Hoppe, P., Crowley, J., Ono, S., and Foley, S.: Sulfur isotope fractionation during oxidation of sulfur dioxide: gas-phase oxidation by OH radicals and aqueous oxidation by H₂O₂, O₃ and iron catalysis, *Atmospheric Chemistry and Physics*, 12, 407–423, 2012.
- Harris, E., Sinha, B., Pinxteren, D. V., Tilgner, A., Fomba, K. W., Schneider, J., Roth, A., Gnauk, T., Fahlbusch, B., Mertes, S., Lee, T., Collett, J., Foley, S., Borrmann, S., Hoppe, P., and Herrmann, H.: Enhanced role of transition metal oxidation of SO₂, *Science*, 340, 727–730, <https://doi.org/10.1126/science.1230911>, 2013a.
- Harris, E., Sinha, B., Van Pinxteren, D., Tilgner, A., Fomba, K. W., Schneider, J., Roth, A., Gnauk, T., Fahlbusch, B., Mertes, S., et al.: Enhanced role of transition metal ion catalysis during in-cloud oxidation of SO₂, *Science*, 340, 727–730, 2013b.
- Harris, E., Sinha, B., Van Pinxteren, D., Schneider, J., Poulain, L., Collett, J., D'Anna, B., Fahlbusch, B., Foley, S., Fomba, K. W., George, C., Gnauk, T., Henning, S., Lee, T., Mertes, S., Roth, A., Stratmann, F., Borrmann, S., Hoppe, P., and Herrmann, H.: In-cloud sulfate addition to single particles resolved with sulfur isotope analysis during HCCT-2010, *Atmospheric Chemistry and Physics*, 14, 4219–4235, <https://doi.org/10.5194/acp-14-4219-2014>, 2014.
- Hatch, L. E., Creamean, J. M., Ault, A. P., Surratt, J. D., Chan, M. N., Seinfeld, J. H., Edgerton, E. S., Su, Y., and Prather, K. A.: Measurements of isoprene-derived organosulfates in ambient aerosols by aerosol time-of-flight mass spectrometry-Part 1: Single particle atmospheric observations in Atlanta, *Environmental Science & Technology*, 45, 5105–5111, 2011.
- Healy, R., Riemer, N., Wenger, J., Murphy, M., West, M., Poulain, L., Wiedensohler, A., O'Connor, I., McGillicuddy, E., Sodeau, J., and Evens, G.: Single particle diversity and mixing state measurements, *Atmospheric Chemistry and Physics*, 14, 6289–6299, <https://doi.org/10.5194/acp-14-6289-2014>, 2014.
- Hegg, D. A. and Larson, T. V.: The effects of microphysical parameterization on model predictions of sulfate production in clouds, *Tellus B*, 42, 272–284, <https://doi.org/10.3402/tellusb.v42i3.15220>, 1990.
- Henning, S., Dieckmann, K., Ignatius, K., Schäfer, M., Zedler, P., Harris, E., Sinha, B., Van Pinxteren, D., Mertes, S., Birmili, W., Merkel, M., Wu, Z., Wiedensohler, A., Wex, H., Herrmann, H., and Stratmann, F.: Influence of cloud processing on CCN activation behaviour in the Thuringian Forest, Germany during HCCT-2010, *Atmospheric Chemistry and Physics*, 14, 7859–7868, <https://doi.org/10.5194/acp-14-7859-2014>, 2014.
- Herrmann, H., Ervens, B., Nowacki, P., Wolke, R., and Zellner, R.: A chemical aqueous phase radical mechanism for tropospheric chemistry, *Chemosphere*, 38, 1223–1232, [https://doi.org/10.1016/S0045-6535\(98\)00520-7](https://doi.org/10.1016/S0045-6535(98)00520-7), 1999.
- Hindmarsh, A. C., Brown, P. N., Grant, K. E., Lee, S. L., Serban, R., Shumaker, D. A. N. E., and Woodward, C. S.: SUNDIALS : Suite of Nonlinear and Differential / Algebraic Equation Solvers, *ACM Transactions on Mathematical Software*, 31, 363–396, <https://doi.org/10.1145/1089014.1089020>, 2005.
- Hoag, K. J., Collett Jr, J. L., and Pandis, S. N.: The influence of drop size-dependent fog chemistry on aerosol processing by San Joaquin Valley fogs, *Atmospheric Environment*, 33, 4817–4832, [https://doi.org/10.1016/S1352-2310\(99\)00268-X](https://doi.org/10.1016/S1352-2310(99)00268-X), 1999.
- Hoose, C., Lohmann, U., Bennartz, R., Croft, B., and Lesins, G.: Global simulations of aerosol processing in clouds, *Atmospheric Chemistry and Physics*, 8, 6939–6963, <https://doi.org/10.5194/acp-8-6939-2008>, 2008.

- Hoppel, W., Frick, G., and Larson, R.: Effect of nonprecipitating clouds on the aerosol size distribution in the marine boundary layer, *Geophysical Research Letters*, 13, 125–128, <https://doi.org/https://doi.org/10.1029/GL013i002p00125>, 1986.
- Hua, W., Chen, Z., Jie, C., Kondo, Y., Hofzumahaus, A., Takegawa, N., Chang, C., Lu, K., Miyazaki, Y., Kita, K., et al.: Atmospheric hydrogen peroxide and organic hydroperoxides during PRIDE-PRD'06, China: their concentration, formation mechanism and contribution to secondary aerosols, *Atmospheric chemistry and physics*, 8, 6755–6773, 2008.
- Hudson, J. G., Noble, S., and Tabor, S.: Cloud supersaturations from CCN spectra Hoppel minima, *Journal of Geophysical Research: Atmospheres*, 120, 3436–3452, 2015.
- Hughes, M., Kodros, J. K., Pierce, J. R., West, M., and Riemer, N.: Machine learning to predict the global distribution of aerosol mixing state metrics, *Atmosphere*, 9, 15, 2018.
- Ivanova, I. T. and Leighton, H. G.: Aerosol–cloud interactions in a mesoscale model. Part II: Sensitivity to aqueous-phase chemistry, *Journal of Atmospheric Sciences*, 65, 309–330, 2008.
- Jacobson, M. Z.: Strong radiative heating due to the mixing state of black carbon in atmospheric aerosols, *Nature*, 409, 695–697, <https://doi.org/https://doi.org/10.1038/35055518>, 2001.
- Jacobson, M. Z.: Fundamentals of atmospheric modeling, Cambridge University Press, 2005.
- Jacobson, M. Z. and Seinfeld, J. H.: Evolution of nanoparticle size and mixing state near the point of emission, *Atmospheric Environment*, 38, 1839–1850, 2004.
- Jaeglé, L., Quinn, P., Bates, T., Alexander, B., and Lin, J.-T.: Global distribution of sea salt aerosols: new constraints from in situ and remote sensing observations, *Atmospheric Chemistry and Physics*, 11, 3137–3157, 2011.
- Jaruga, A. and Pawlowska, H.: libcloudph++2.0: aqueous-phase chemistry extension of the particle-based cloud microphysics scheme, *Geoscientific Model Development*, 11, 3623–3645, <https://doi.org/https://doi.org/10.5194/gmd-11-3623-2018>, 2018.
- Jia, H., Ma, X., Yu, F., Liu, Y., and Yin, Y.: Distinct impacts of increased aerosols on cloud droplet number concentration of stratus/stratocumulus and cumulus, *Geophysical Research Letters*, 46, 13 517–13 525, 2019.
- Jimenez, J. L., Canagaratna, M., Donahue, N., Prevot, A., Zhang, Q., Kroll, J. H., DeCarlo, P. F., Allan, J. D., Coe, H., Ng, N., et al.: Evolution of organic aerosols in the atmosphere, *Science*, 326, 1525–1529, 2009.
- Kaufman, Y. J., Koren, I., Remer, L. A., Rosenfeld, D., and Rudich, Y.: The effect of smoke, dust, and pollution aerosol on shallow cloud development over the Atlantic Ocean, *Proceedings of the National Academy of Sciences*, 102, 11 207–11 212, 2005.
- Kirpes, R. M., Bondy, A. L., Bonanno, D., Moffet, R. C., Wang, B., Laskin, A., Ault, A. P., and Pratt, K. A.: Secondary sulfate is internally mixed with sea spray aerosol and organic aerosol in the winter Arctic, *Atmospheric Chemistry and Physics*, 18, 3937–3949, 2018.
- Kleinman, L. I., Daum, P. H., Lee, Y.-N., Lewis, E. R., Sedlacek III, A., Sennum, G., Springston, S., Wang, J., Hubbe, J., Jayne, J., et al.: Aerosol concentration and size distribution measured below, in, and above cloud from the DOE G-1 during VOCALS-REx, *Atmospheric Chemistry and Physics*, 12, 207–223, 2012.
- Knopf, D. A., Alpert, P. A., and Wang, B.: The role of organic aerosol in atmospheric ice nucleation: A review, *ACS Earth Space Chem.*, 2, 168–202, <https://doi.org/https://doi.org/10.1021/acsearthspacechem.7b00120>, 2018.
- Kodros, J. K., Hanna, S. J., Bertram, A. K., Leaitch, W. R., Schulz, H., Herber, A. B., Zanatta, M., Burkart, J., Willis, M. D., Abbatt, J. P., et al.: Size-resolved mixing state of black carbon in the Canadian high Arctic and implications for simulated direct radiative effect, *Atmospheric Chemistry and Physics*, 18, 11 345–11 361, 2018.

- Koike, M., Moteki, N., Khatri, P., Takamura, T., Takegawa, N., Kondo, Y., Hashioka, H., Matsui, H., Shimizu, A., and Sugimoto, N.: Case study of absorption aerosol optical depth closure of black carbon over the East China Sea, *Journal of Geophysical Research: Atmospheres*, 119, 122–136, 2014.
- Kreidenweis, S., Walcek, C., Feingold, G., Gong, W., Jacobson, M., Kim, C.-H., Liu, X., Penner, J., Nenes, A., and Seinfeld, J.: Modification of aerosol mass and size distribution due to aqueous phase SO₂ oxidation in clouds: Comparisons of several models, *Journal of Geophysical Research: Atmospheres*, 108, 8630, <https://doi.org/https://doi.org/10.1029/2002JD002697>, 2003a.
- Kreidenweis, S. M., Walcek, C. J., Feingold, G., Gong, W., Jacobson, M. Z., Kim, C.-H., Liu, X., Penner, J. E., Nenes, A., and Seinfeld, J. H.: Modification of aerosol mass and size distribution due to aqueous-phase SO₂ oxidation in clouds: Comparisons of several models, *Journal of Geophysical Research: Atmospheres*, 108, 2003b.
- Lance, S., Barth, M., and Carlton, A.: Multiphase chemistry: Experimental design for coordinated measurement and modeling studies of cloud processing at a mountaintop, *Bulletin of the American Meteorological Society*, 98, ES163–ES167, <https://doi.org/https://doi.org/10.1175/BAMS-D-17-0015.1>, 2017.
- Lanz, V., Prévôt, A., Alfarra, M., Weimer, S., Mohr, C., DeCarlo, P., Gianini, M., Hueglin, C., Schneider, J., Favez, O., et al.: Characterization of aerosol chemical composition with aerosol mass spectrometry in Central Europe: an overview, *Atmospheric Chemistry and Physics*, 10, 10 453–10 471, 2010.
- Laskin, A., Cowin, J., and Iedema, M.: Analysis of individual environmental particles using modern methods of electron microscopy and X-ray microanalysis, *Journal of Electron Spectroscopy and Related Phenomena*, 150, 260–274, <https://doi.org/https://doi.org/10.1016/j.elspec.2005.06.008>, *science and Spectroscopy of Environmentally Important Interfaces*, 2006.
- Laskin, A., Moffet, R. C., and Gilles, M. K.: Chemical imaging of atmospheric particles, *Accounts of chemical research*, 52, 3419–3431, 2019.
- Lauer, A., Hendricks, J., Ackermann, I., Schell, B., Hass, H., and Metzger, S.: Simulating aerosol microphysics with the ECHAM/MADE GCM—Part I: Model description and comparison with observations, *Atmospheric Chemistry and Physics*, 5, 3251–3276, 2005.
- Lee, S.-R. and Wu, C.-Y.: Size distribution evolution of fine aerosols due to intercoagulation with coarse aerosols, *Aerosol science and technology*, 39, 358–370, 2005.
- Lesins, G., Chylek, P., and Lohmann, U.: A Study of Internal and External Mixing Scenarios and Its Effect on Aerosol Optical Properties and Direct Radiative Forcing, *Journal of Geophysical Research: Atmospheres*, 107, AAC 5–1–AAC 5–12, <https://doi.org/https://doi.org/10.1029/2001JD000973>, 2002.
- Levy, R. C., Remer, L. A., and Dubovik, O.: Global aerosol optical properties and application to Moderate Resolution Imaging Spectroradiometer aerosol retrieval over land, *Journal of Geophysical Research: Atmospheres*, 112, 2007.
- Li, W., Li, P., Sun, G., Zhou, S., Yuan, Q., and Wang, W.: Cloud residues and interstitial aerosols from non-precipitating clouds over an industrial and urban area in northern China, *Atmospheric Environment*, 45, 2488–2495, <https://doi.org/https://doi.org/10.1016/j.atmosenv.2011.02.044>, 2011.
- Lian, X., Ou, J., Zhang, G., Li, M., Tang, M., Zhou, Z., Fu, Y., Peng, P., Sheng, G., Miller, M., Yang, Y., Wang, X., Bi, X., Peng, L., Lin, Q., and Chen, D.: In-cloud formation of secondary species in iron-containing particles, *Atmospheric Chemistry and Physics*, 19, 1195–1206, <https://doi.org/https://doi.org/10.5194/acp-19-1195-2019>, 2019.
- Liggio, J., Gordon, M., Smallwood, G., Li, S.-M., Stroud, C., Staebler, R., Lu, G., Lee, P., Taylor, B., and Brook, J. R.: Are emissions of black carbon from gasoline vehicles underestimated? Insights from near and on-road measurements, *Environmental science & technology*, 46, 4819–4828, 2012.
- Lim, Y., Tan, Y., Perri, M., Seitzinger, S., and Turpin, B.: Aqueous chemistry and its role in secondary organic aerosol (SOA) formation, *Atmospheric Chemistry and Physics*, 10, 10 521–10 539, 2010.

Lin, Q., Zhang, G., Peng, L., Bi, X., Wang, X., Brechtel, F. J., Li, M., Chen, D., Peng, P., Sheng, G., et al.: In situ chemical composition measurement of individual cloud residue particles at a mountain site, southern China, *Atmospheric Chemistry and Physics*, 17, 8473–8488, 2017.

Liu, D., Allan, J., Whitehead, J., Young, D., Flynn, M., Coe, H., McFiggans, G., Fleming, Z. L., and Bandy, B.: Ambient black carbon particle hygroscopic properties controlled by mixing state and composition, *Atmospheric Chemistry and Physics*, 13, 2015–2029, <https://doi.org/10.5194/acp-13-2015-2013>, 2013.

Liu, D., Whitehead, J., Alfara, M. R., Reyes-Villegas, E., Spracklen, D. V., Reddington, C. L., Kong, S., Williams, P. I., Ting, Y. C., Haslett, S., Taylor, J. W., Flynn, M. J., Morgan, W. T., McFiggans, G., Coe, H., and Allan, J. D.: Black-carbon absorption enhancement in the atmosphere determined by particle mixing state, *Nature Geoscience*, 10, 184–188, <https://doi.org/10.1038/ngeo2901>, 2017.

Liu, D., He, C., Schwarz, J. P., and Wang, X.: Lifecycle of light-absorbing carbonaceous aerosols in the atmosphere, *npj Climate and Atmospheric Science*, 3, 1–18, 2020.

Liu, J., Horowitz, L. W., Fan, S., Carlton, A. G., and Levy, H.: Global in-cloud production of secondary organic aerosols: Implementation of a detailed chemical mechanism in the GFDL atmospheric model AM3, *Journal of Geophysical Research: Atmospheres*, 117, 2012a.

Liu, X., Easter, R. C., Ghan, S. J., Zaveri, R., Rasch, P., Shi, X., Lamarque, J. F., Gettelman, A., Morrison, H., Vitt, F., Conley, A., Park, S., Neale, R., Hannay, C., Ekman, A. M., Hess, P., Mahowald, N., Collins, W., Iacono, M. J., Bretherton, C. S., Flanner, M. G., and Mitchell, D.: Toward a minimal representation of aerosols in climate models: Description and evaluation in the Community Atmosphere Model CAM5, *Geoscientific Model Development*, 5, 709–739, <https://doi.org/10.5194/gmd-5-709-2012>, 2012b.

Liu, X., Easter, R. C., Ghan, S. J., Zaveri, R., Rasch, P., Shi, X., Lamarque, J.-F., Gettelman, A., Morrison, H., Vitt, F., et al.: Toward a minimal representation of aerosols in climate models: Description and evaluation in the Community Atmosphere Model CAM5, *Geoscientific Model Development*, 5, 709–739, 2012c.

Loeb, N. G. and Su, W.: Direct aerosol radiative forcing uncertainty based on a radiative perturbation analysis, *Journal of Climate*, 23, 5288–5293, 2010.

Luo, J., Zhang, Q., Luo, J., Liu, J., Huo, Y., and Zhang, Y.: Optical modeling of black carbon with different coating materials: The effect of coating configurations, *Journal of Geophysical Research: Atmospheres*, 124, 13 230–13 253, 2019.

Ma, X., Yu, F., and Luo, G.: Aerosol direct radiative forcing based on GEOS-Chem-APM and uncertainties, *Atmospheric Chemistry and Physics*, 12, 5563–5581, 2012.

Majdi, M., Kim, Y., Turquety, S., and Sartelet, K.: Impact of mixing state on aerosol optical properties during severe wildfires over the Euro-Mediterranean region, *Atmospheric Environment*, 220, 117 042, <https://doi.org/10.1016/j.atmosenv.2019.117042>, URL <https://doi.org/10.1016/j.atmosenv.2019.117042>, 2020.

Majeed, M. A. and Wexler, A. S.: Microphysics of aqueous droplets in clouds and fogs as applied to PM-fine modeling, *Atmospheric Environment*, 35, 1639–1653, 2001.

Mayol-Bracero, O. L., Gabriel, R., Andreae, M. O., Kirchstetter, T. W., Novakov, T., Ogren, J., Sheridan, P., and Streets, D. G.: Carbonaceous aerosols over the Indian Ocean during the Indian Ocean Experiment (INDOEX): Chemical characterization, optical properties, and probable sources, *Journal of Geophysical Research: Atmospheres*, 107, <https://doi.org/10.1029/2000JD000039>, 2002.

McComiskey, A., Schwartz, S. E., Schmid, B., Guan, H., Lewis, E. R., Ricchiazzi, P., and Ogren, J. A.: Direct aerosol forcing: Calculation from observables and sensitivities to inputs, *Journal of Geophysical Research: Atmospheres*, 113, 2008.

McKay, M. D., Beckman, R. J., and Conover, W. J.: A comparison of three methods for selecting values of input variables in the analysis of output from a computer code, *Technometrics*, 42, 55–61, 2000.

McMurtry, P.: AEROSOLS | Observations and Measurements, in: Encyclopedia of Atmospheric Sciences, edited by Holton, J. R., pp. 20–34, Academic Press, Oxford, 2003.

McNeill, V. F.: Aqueous organic chemistry in the atmosphere: Sources and chemical processing of organic aerosols, Environmental Science and Technology, 49, 1237–1244, [https://doi.org/https://doi.org/10.1021/es5043707](https://doi.org/10.1021/es5043707), 2015a.

McNeill, V. F.: Aqueous organic chemistry in the atmosphere: Sources and chemical processing of organic aerosols, 2015b.

Michel Flores, J., Bar-Or, R. Z., Bluvshtein, N., Abo-Riziq, A., Kostinski, A., Borrmann, S., Koren, I., Koren, I., and Rudich, Y.: Absorbing aerosols at high relative humidity: Linking hygroscopic growth to optical properties, Atmospheric Chemistry and Physics, 12, 5511–5521, <https://doi.org/10.5194/acp-12-5511-2012>, 2012.

Miller, S. L., Nazaroff, W. W., Jimenez, J. L., Boerstra, A., Buonanno, G., Dancer, S. J., Kurnitski, J., Marr, L. C., Morawska, L., and Noakes, C.: Transmission of SARS-CoV-2 by inhalation of respiratory aerosol in the Skagit Valley Chorale superspreading event, Indoor air, 31, 314–323, 2021.

Mitchell Jr, J. M.: The effect of atmospheric aerosols on climate with special reference to temperature near the earth's surface, Journal of Applied Meteorology and Climatology, 10, 703–714, 1971.

Moffet, R. C. and Prather, K. A.: In-situ measurements of the mixing state and optical properties of soot with implications for radiative forcing estimates, Proceedings of the National Academy of Sciences of the United States of America, 106, 11 872–11 877, <https://doi.org/10.1073/pnas.0900040106>, 2009.

Monahan, E. C., Spiel, D. E., and Davidson, K. L.: A model of marine aerosol generation via whitecaps and wave disruption, in: Oceanic whitecaps, pp. 167–174, Springer, 1986.

Moore, R., Cerully, K., Bahreini, R., Brock, C., Middlebrook, A., and Nenes, A.: Hygroscopicity and composition of California CCN during summer 2010, Journal of Geophysical Research: Atmospheres, 117, 2012.

Myhre, G., Shindell, D., Collins, W., Fuglestvedt, J., Huang, J., Koch, D., Lamarque, J.-F., Lee, D., Mendoza, B., Nakajima, T., Robock, A., Stephens, G., Takemura, T., and Zhang, H.: Anthropogenic and Natural Radiative Forcing, book section 8, p. 659–740, Cambridge University Press, Cambridge, United Kingdom and New York, NY, USA, <https://doi.org/10.1017/CBO9781107415324.018>, URL www.climatechange2013.org, 2013.

Nam, E.: Analysis of particulate matter emissions from light-duty gasoline vehicles in Kansas City, US Environmental Protection Agency, 2008.

Nandy, L., Yao, Y., Zheng, Z., and Riemer, N.: Water uptake and optical properties of mixed organic-inorganic particles, Aerosol Science and Technology, pp. 1–16, 2021.

Nenes, A., Ghan, S., Abdul-Razzak, H., Chuang, P. Y., and Seinfeld, J. H.: Kinetic limitations on cloud droplet formation and impact on cloud albedo, Tellus B: Chemical and Physical Meteorology, 53, 133–149, [https://doi.org/https://doi.org/10.3402/tellusb.v53i2.16569](https://doi.org/10.3402/tellusb.v53i2.16569), 2001.

Noble, S. R. and Hudson, J. G.: Effects of continental clouds on surface Aitken and accumulation modes, Journal of Geophysical Research: Atmospheres, 124, 5479–5502, [https://doi.org/https://doi.org/10.1029/2019JD030297](https://doi.org/10.1029/2019JD030297), 2019.

Nowak, J., Neuman, J., Bahreini, R., Brock, C., Middlebrook, A., Wollny, A., Holloway, J., Peischl, J., Ryerson, T., and Fehsenfeld, F.: Airborne observations of ammonia and ammonium nitrate formation over Houston, Texas, Journal of Geophysical Research: Atmospheres, 115, 2010.

O'Brien, R. E., Wang, B., Laskin, A., Riemer, N., West, M., Zhang, Q., Sun, Y., Yu, X.-Y., Alpert, P., Knopf, D. A., et al.: Chemical imaging of ambient aerosol particles: Observational constraints on mixing state parameterization, Journal of Geophysical Research: Atmospheres, 120, 9591–9605, 2015.

Oikawa, E., Nakajima, T., Inoue, T., and Winker, D.: A study of the shortwave direct aerosol forcing using ESSP/CALIPSO observation and GCM simulation, Journal of Geophysical Research: Atmospheres, 118, 3687–3708, 2013.

- Oshima, N., Koike, M., Zhang, Y., Kondo, Y., Moteki, N., Takegawa, N., and Miyazaki, Y.: Aging of black carbon in outflow from anthropogenic sources using a mixing state resolved model: Model development and evaluation, *Journal of Geophysical Research: Atmospheres*, 114, 2009.
- Ovchinnikov, M. and Easter, R.: Modeling aerosol growth by aqueous chemistry in a nonprecipitating cloud, *Journal of Geophysical Research: Atmospheres*, 115, D14 210, [https://doi.org/https://doi.org/10.1029/2009JD012816](https://doi.org/10.1029/2009JD012816), 2010.
- Park, R. J., Jacob, D. J., Field, B. D., Yantosca, R. M., and Chin, M.: Natural and transboundary pollution influences on sulfate-nitrate-ammonium aerosols in the United States: Implications for policy, *Journal of Geophysical Research: Atmospheres*, 109, 2004.
- Peng, Y., Lohmann, U., and Leaitch, R.: Importance of vertical velocity variations in the cloud droplet nucleation process of marine stratus clouds, *Journal of Geophysical Research: Atmospheres*, 110, 2005.
- Petters, M. D. and Kreidenweis, S. M.: A single parameter representation of hygroscopic growth and cloud condensation nucleus activity, *Atmospheric Chemistry and Physics*, 7, 1961–1971, [https://doi.org/https://doi.org/10.5194/acp-7-1961-2007](https://doi.org/10.5194/acp-7-1961-2007), 2007.
- Phan, N.-T., Kim, K.-H., Shon, Z.-H., Jeon, E.-C., Jung, K., and Kim, N.-J.: Analysis of ammonia variation in the urban atmosphere, *Atmospheric Environment*, 65, 177–185, 2013.
- Philip, S., Martin, R. V., Van Donkelaar, A., Lo, J. W. H., Wang, Y., Chen, D., Zhang, L., Kasibhatla, P. S., Wang, S., Zhang, Q., Lu, Z., Streets, D. G., Bittman, S., and Macdonald, D. J.: Global chemical composition of ambient fine particulate matter for exposure assessment, *Environmental Science and Technology*, 48, 13 060–13 068, [https://doi.org/http://doi.org/10.1021/es502965b](https://doi.org/10.1021/es502965b), 2014.
- Pierce, J., Evans, M., Scott, C., D'Andrea, S., Farmer, D., Swietlicki, E., and Spracklen, D.: Weak global sensitivity of cloud condensation nuclei and the aerosol indirect effect to Criegee+ SO₂ chemistry, *Atmospheric Chemistry and Physics*, 13, 3163–3176, 2013.
- Pierce, J., Croft, B., Kodros, J., D'Andrea, S., and Martin, R.: The importance of interstitial particle scavenging by cloud droplets in shaping the remote aerosol size distribution and global aerosol-climate effects, *Atmospheric Chemistry and Physics*, 15, 6147–6158, 2015a.
- Pierce, J. R., Croft, B., Kodros, J. K., D'Andrea, S. D., and Martin, R. V.: The importance of interstitial particle scavenging by cloud droplets in shaping the remote aerosol size distribution and global aerosol-climate effects, *Atmospheric Chemistry and Physics*, 15, 6147–6158, [https://doi.org/https://doi.org/10.5194/acp-15-6147-2015](https://doi.org/10.5194/acp-15-6147-2015), 2015b.
- Prather, K. A., Wang, C. C., and Schooley, R. T.: Reducing transmission of SARS-CoV-2, *Science*, 368, 1422–1424, 2020.
- Pruppacher, H. R. and Klett, J. D.: *Microphysics of Clouds and Precipitation*: Reprinted 1980, Springer Science & Business Media, 2012.
- Pye, H. O., Nenes, A., Alexander, B., Ault, A. P., Barth, M. C., Clegg, S. L., Collett Jr, J. L., Fahey, K. M., Hennigan, C. J., Herrmann, H., et al.: The acidity of atmospheric particles and clouds, *Atmospheric Chemistry and Physics*, 20, 4809–4888, [https://doi.org/https://doi.org/10.5194/acp-20-4809-2020](https://doi.org/10.5194/acp-20-4809-2020), 2020.
- Rasch, P. J., Barth, M. C., Kiehl, J. T., Schwartz, S. E., and Benkovitz, C. M.: A description of the global sulfur cycle and its controlling processes in the National Center for Atmospheric Research Community Climate Model, Version 3, *Journal of Geophysical Research: Atmospheres*, 105, 1367–1385, 2000.
- Riemer, N. and West, M.: Quantifying aerosol mixing state with entropy and diversity measures, *Atmospheric Chemistry and Physics*, 13, 11 423–11 439, [https://doi.org/https://doi.org/10.5194/acp-13-11423-2013](https://doi.org/10.5194/acp-13-11423-2013), 2013.
- Riemer, N., Vogel, H., Vogel, B., and Fiedler, F.: Modeling aerosols on the mesoscale- γ : Treatment of soot aerosol and its radiative effects, *Journal of Geophysical Research: Atmospheres*, 108, [https://doi.org/https://doi.org/10.1029/2003JD003448](https://doi.org/10.1029/2003JD003448), 2003.

Riemer, N., West, M., Zaveri, R. A., and Easter, R. C.: Simulating the evolution of soot mixing state with a particle-resolved aerosol model, *Journal of Geophysical Research: Atmospheres*, 114, 1–22, <https://doi.org/10.1029/2008JD011073>, 2009.

Riemer, N., West, M., Zaveri, R., and Easter, R.: Estimating black carbon aging time-scales with a particle-resolved aerosol model, *Journal of Aerosol Science*, 41, 143–158, <https://doi.org/10.1016/j.jaerosci.2009.08.009>, 2010.

Riemer, N., Ault, A. P., West, M., Craig, R. L., and Curtis, J. H.: Aerosol mixing state: measurements, modeling, and impacts, *Reviews of Geophysics*, 57, 187–249, <https://doi.org/10.1029/2018RG000615>, 2019.

Rissler, J., Nordin, E. Z., Eriksson, A. C., Nilsson, P. T., Frosch, M., Sporre, M. K., Wierzbicka, A., Svenningsson, B., Löndahl, J., Messing, M. E., Sjogren, S., Hemmingsen, J. G., Loft, S., Pagels, J. H., and Swietlicki, E.: Effective density and mixing state of aerosol particles in a near-traffic urban environment, *Environmental Science and Technology*, 48, 6300–6308, <https://doi.org/10.1021/es5000353>, 2014.

Roelofs, G., Stier, P., Feichter, J., Vignati, E., and Wilson, J.: Aerosol activation and cloud processing in the global aerosol-climate model ECHAM5-HAM, *Atmospheric Chemistry and Physics*, 6, 2389–2399, 2006.

Romakkaniemi, S., Kokkola, H., Lehtinen, K., and Laaksonen, A.: The influence of nitric acid on the cloud processing of aerosol particles, *Atmospheric Chemistry and Physics*, 6, 1627–1634, 2006.

Roth, A., Schneider, J., Klimach, T., Mertes, S., Van Pinxteren, D., Herrmann, H., and Borrmann, S.: Aerosol properties, source identification, and cloud processing in orographic clouds measured by single particle mass spectrometry on a central European mountain site during HCCT-2010, *Atmospheric Chemistry and Physics*, 16, 505–524, <https://doi.org/10.5194/acp-16-505-2016>, 2016.

Rothenberg, D. and Wang, C.: Metamodeling of droplet activation for global climate models, *Journal of the Atmospheric Sciences*, 73, 1255–1272, 2016.

Saliba, G., Chen, C. L., Lewis, S., Russell, L. M., Quinn, P. K., Bates, T. S., Bell, T. G., Lawler, M. J., Saltzman, E. S., Sanchez, K. J., Moore, R., Shook, M., Rivellini, L. H., Lee, A., Baetge, N., Carlson, C. A., and Behrenfeld, M. J.: Seasonal Differences and Variability of Concentrations, Chemical Composition, and Cloud Condensation Nuclei of Marine Aerosol Over the North Atlantic, *Journal of Geophysical Research: Atmospheres*, 125, 1–24, <https://doi.org/10.1029/2020JD033145>, 2020.

Scarnato, B., Vahidinia, S., Richard, D., and Kirchstetter, T.: Effects of internal mixing and aggregate morphology on optical properties of black carbon using a discrete dipole approximation model, *Atmospheric Chemistry and Physics*, 13, 5089–5101, 2013.

Schell, B., Ackermann, I. J., Hass, H., Binkowski, F. S., and Ebel, A.: Modeling the formation of secondary organic aerosol within a comprehensive air quality model system, *Journal of Geophysical Research: Atmospheres*, 106, 28 275–28 293, <https://doi.org/10.1029/2001JD000384>, 2001a.

Schell, B., Ackermann, I. J., Hass, H., Binkowski, F. S., and Ebel, A.: Modeling the formation of secondary organic aerosol within a comprehensive air quality model system, *Journal of Geophysical Research: Atmospheres*, 106, 28 275–28 293, 2001b.

Seinfeld, J. H. and Pandis, S. N.: ATMOSPHERIC From Air Pollution to Climate Change SECOND EDITION, John Wiley & Sons, Inc., 2006.

Seinfeld, J. H., Bretherton, C., Carslaw, K. S., Coe, H., DeMott, P. J., Dunlea, E. J., Feingold, G., Ghan, S., Guenther, A. B., Kahn, R., and Wood, R.: Improving our fundamental understanding of the role of aerosol- cloud interactions in the climate system, *Proceedings of the National Academy of Sciences*, 113, 5781–5790, <https://doi.org/10.1073/pnas.1514043113>, 2016a.

Seinfeld, J. H., Bretherton, C., Carslaw, K. S., Coe, H., DeMott, P. J., Dunlea, E. J., Feingold, G., Ghan, S., Guenther, A. B., Kahn, R., et al.: Improving our fundamental understanding of the role of aerosol- cloud interactions in the climate system, *Proceedings of the National Academy of Sciences*, 113, 5781–5790, 2016b.

Shao, J., Chen, Q., Wang, Y., Lu, X., He, P., Sun, Y., Shah, V., Martin, R. V., Philip, S., Song, S., Zhao, Y., Xie, Z., Zhang, L., and Alexander, B.: Heterogeneous sulfate aerosol formation mechanisms during wintertime Chinese haze events: air quality model assessment using observations of sulfate oxygen isotopes in Beijing, *Atmospheric Chemistry and Physics*, 19, 6107–6123, <https://doi.org/10.5194/acp-19-6107-2019>, 2019a.

Shao, J., Chen, Q., Wang, Y., Lu, X., He, P., Sun, Y., Shah, V., Martin, R. V., Philip, S., Song, S., et al.: Heterogeneous sulfate aerosol formation mechanisms during wintertime Chinese haze events: air quality model assessment using observations of sulfate oxygen isotopes in Beijing, *Atmospheric Chemistry and Physics*, 19, 6107–6123, 2019b.

Shao, Y.: A model for mineral dust emission, *Journal of Geophysical Research: Atmospheres*, 106, 20 239–20 254, 2001.

Shima, S., Kusano, K., Kawano, A., Sugiyama, T., and Kawahara, S.: The super-droplet method for the numerical simulation of clouds and precipitation: a particle-based and probabilistic microphysics model coupled with a non-hydrostatic model, *Quarterly Journal of the Royal Meteorological Society: A journal of the atmospheric sciences, applied meteorology and physical oceanography*, 135, 1307–1320, [https://doi.org/https://doi.org/10.1002/qj.441](https://doi.org/10.1002/qj.441), 2009.

Sipilä, M., Berndt, T., Petäjä, T., Brus, D., Vanhanen, J., Stratmann, F., Patokoski, J., Mauldin, R. L., Hyvärinen, A.-P., Lihavainen, H., et al.: The role of sulfuric acid in atmospheric nucleation, *Science*, 327, 1243–1246, 2010.

Smith, J. D., Sio, V., Yu, L., Zhang, Q., and Anastasio, C.: Secondary organic aerosol production from aqueous reactions of atmospheric phenols with an organic triplet excited state, *Environmental Science and Technology*, 48, 1049–1057, <https://doi.org/https://doi.org/10.1021/es4045715>, 2014a.

Smith, J. D., Sio, V., Yu, L., Zhang, Q., and Anastasio, C.: Secondary organic aerosol production from aqueous reactions of atmospheric phenols with an organic triplet excited state, *Environmental science & technology*, 48, 1049–1057, 2014b.

Sölich, I. and Kärcher, B.: A large-eddy model for cirrus clouds with explicit aerosol and ice microphysics and Lagrangian ice particle tracking, *Quarterly Journal of the Royal Meteorological Society*, 136, 2074–2093, <https://doi.org/https://doi.org/10.1002/qj.689>, 2010.

Somers, J.: Mobile source black carbon emissions, in: Black carbon emissions and climate change: A technical workshop, 2004.

Spracklen, D., Pringle, K., Carslaw, K., Chipperfield, M., and Mann, G.: A global off-line model of size-resolved aerosol microphysics: I. Model development and prediction of aerosol properties, *Atmospheric Chemistry and Physics*, 5, 2227–2252, 2005.

Stevens, B. and Feingold, G.: Untangling aerosol effects on clouds and precipitation in a buffered system, *Nature*, 461, 607–613, 2009.

Stier, P., Feichter, J., Kinne, S., Kloster, S., Vignati, E., Wilson, J., Ganzeveld, L., Tegen, I., Werner, M., Balkanski, Y., and Petzold, A.: The aerosol-climate model ECHAM5-HAM, *Atmospheric Chemistry and Physics*, 5, 1125–1156, <https://doi.org/https://doi.org/10.5194/acp-5-1125-2005>, 2005.

Stier, P., Seinfeld, J. H., Kinne, S., and Boucher, O.: Aerosol absorption and radiative forcing, *Atmospheric Chemistry and Physics*, 7, 5237–5261, 2007.

Stokes, R. and Robinson, R.: Interactions in aqueous nonelectrolyte solutions. I. Solute-solvent equilibria, *The Journal of Physical Chemistry*, 70, 2126–2131, 1966.

Stubenrauch, C. J., Rossow, W. B., Kinne, S., Ackerman, S., Cesana, G., Chepfer, H., Di Girolamo, L., Getzewich, B., Guignard, A., Heidinger, A., et al.: Assessment of global cloud datasets from satellites: Project and database initiated by the GEWEX radiation panel, *Bulletin of the American Meteorological Society*, 94, 1031–1049, 2013.

Subba, T., Gogoi, M. M., Pathak, B., Bhuyan, P. K., and Babu, S. S.: Recent trend in the global distribution of aerosol direct radiative forcing from satellite measurements, *Atmospheric Science Letters*, 21, e975, 2020.

- Tian, J., Riemer, N., West, M., Pfaffenberger, L., Schlager, H., and Petzold, A.: Modeling the evolution of aerosol particles in a ship plume using PartMC-MOSAIC, *Atmospheric chemistry and physics*, 14, 5327–5347, 2014.
- Tilgner, A., Majdik, Z., Sehili, A. M., Simmel, M., Wolke, R., and Herrmann, H.: SPACCIM: Simulations of the multiphase chemistry occurring in the FEBUKO hill cap cloud experiments, *Atmospheric Environment*, 39, 4389–4401, [https://doi.org/https://doi.org/10.1016/j.atmosenv.2005.02.028](https://doi.org/10.1016/j.atmosenv.2005.02.028), 2005.
- Titos, G., Jefferson, A., Sheridan, P. J., Andrews, E., Lyamani, H., Alados-Arboledas, L., and Ogren, J. A.: Aerosol light-scattering enhancement due to water uptake during the TCAP campaign, *Atmospheric Chemistry and Physics*, 14, 7031–7043, <https://doi.org/10.5194/acp-14-7031-2014>, 2014.
- Titos, G., Cazorla, A., Zieger, P., Andrews, E., Lyamani, H., Granados-Muñoz, M. J., Olmo, F. J., and Alados-Arboledas, L.: Effect of hygroscopic growth on the aerosol light-scattering coefficient: A review of measurements, techniques and error sources, *Atmospheric Environment*, 141, 494–507, <https://doi.org/10.1016/j.atmosenv.2016.07.021>, 2016.
- Tolocka, M. P., Jang, M., Ginter, J. M., Cox, F. J., Kamens, R. M., and Johnston, M. V.: Formation of oligomers in secondary organic aerosol, *Environmental Science & Technology*, 38, 1428–1434, 2004.
- Twomey, S.: The influence of pollution on the shortwave albedo of clouds, *Journal of the atmospheric sciences*, 34, 1149–1152, 1977.
- Unterstrasser, S. and Söhlch, I.: Optimisation of simulation particle number in a Lagrangian ice microphysical model, *Geoscientific Model Development*, 7, 695–709, <https://doi.org/https://doi.org/10.5194/gmd-7-695-2014>, 2014.
- Van Der Does, M., Knippertz, P., Zschenderlein, P., Harrison, R. G., and Stuut, J.-B. W.: The mysterious long-range transport of giant mineral dust particles, *Science advances*, 4, eaau2768, 2018.
- Vignati, E., Karl, M., Krol, M., Wilson, J., Stier, P., and Cavalli, F.: Sources of uncertainties in modelling black carbon at the global scale, *Atmospheric chemistry and physics*, 10, 2595–2611, 2010.
- Wagner, N. L., Brock, C. A., Angevine, W. M., Beyersdorf, A., Campuzano-Jost, P., Day, D., De Gouw, J. A., Diskin, G. S., Gordon, T., Graus, M. G., et al.: In situ vertical profiles of aerosol extinction, mass, and composition over the southeast United States during SENEX and SEAC4RS: observations of a modest aerosol enhancement aloft, *Atmospheric Chemistry and Physics*, 15, 7085–7102, 2015.
- Wang, Y., Ying, Q., Hu, J., and Zhang, H.: Spatial and temporal variations of six criteria air pollutants in 31 provincial capital cities in China during 2013–2014, *Environment international*, 73, 413–422, 2014.
- WHO et al.: Air pollution and child health: prescribing clean air: summary, Tech. rep., World Health Organization, 2018.
- Winker, D., Pelon, J., Coakley Jr, J., Ackerman, S., Charlson, R., Colarco, P., Flamant, P., Fu, Q., Hoff, R., Kittaka, C., et al.: The CALIPSO mission: A global 3D view of aerosols and clouds, *Bulletin of the American Meteorological Society*, 91, 1211–1230, 2010.
- Winkler, P.: The Growth of Atmospheric Aerosol Particles as a Function of the Relative Humidity—II. An Improved Concept of Mixed Nuclei, *JOURNAL OF AEROSOL SCIENCE*, 4, 373–387, [https://doi.org/https://doi.org/10.1016/0021-8502\(73\)90027-X](https://doi.org/https://doi.org/10.1016/0021-8502(73)90027-X), 1973a.
- Winkler, P.: The growth of atmospheric aerosol particles as a function of the relative humidity—II. An improved concept of mixed nuclei, *Journal of Aerosol Science*, 4, 373–387, 1973b.
- Wolke, R., Sehili, A., Simmel, M., Knoth, O., Tilgner, A., and Herrmann, H.: SPACCIM: A parcel model with detailed microphysics and complex multiphase chemistry, *Atmospheric Environment*, 39, 4375–4388, 2005a.
- Wolke, R., Sehili, A. M., Simmel, M., Knoth, O., Tilgner, A., and Herrmann, H.: SPACCIM: A parcel model with detailed microphysics and complex multiphase chemistry, *Atmospheric Environment*, 39, 4375–4388, <https://doi.org/10.1016/j.atmosenv.2005.02.038>, 2005b.

- Wonaschuetz, A., Sorooshian, A., Ervens, B., Chuang, P. Y., Feingold, G., Murphy, S. M., De Gouw, J., Warneke, C., and Jonsson, H. H.: Aerosol and gas re-distribution by shallow cumulus clouds: An investigation using airborne measurements, *Journal of Geophysical Research: Atmospheres*, 117, 2012.
- Wu, Y., Cheng, T., and Zheng, L.: Light absorption of black carbon aerosols strongly influenced by particle morphology distribution, *Environmental Research Letters*, 15, 094 051, 2020.
- Ye, Q., Gu, P., Li, H. Z., Robinson, E. S., Lipsky, E., Kaltsonoudis, C., Lee, A. K., Apte, J. S., Robison, A. L., Sullivan, R. C., Presto, A. A., and Donahue, N. M.: Spatial variability of sources and mixing state of atmospheric particles in a metropolitan area, *ENVIRON SCI TECHNOL*, 52, 6807–6815, [https://doi.org/https://doi.org/10.1021/acs.est8b01011](https://doi.org/10.1021/acs.est8b01011), 2018.
- Yu, H., Kaufman, Y., Chin, M., Feingold, G., Remer, L., Anderson, T., Balkanski, Y., Bellouin, N., Boucher, O., Christopher, S., et al.: A review of measurement-based assessments of the aerosol direct radiative effect and forcing, *Atmospheric Chemistry and Physics*, 6, 613–666, 2006.
- Yu, H., Tan, Q., Zhou, L., Zhou, Y., Bian, H., Chin, M., Ryder, C. L., Levy, R. C., Pradhan, Y., Shi, Y., et al.: Observation and modeling of a historic African dust intrusion into the Caribbean Basin and the southern US in June 2020, *Atmospheric Chemistry and Physics Discussions*, pp. 1–40, 2021.
- Yuskiewicz, B. A., Stratmann, F., Birmili, W., Wiedensohler, A., Swietlicki, E., Berg, O., and Zhou, J.: The effects of in-cloud mass production on atmospheric light scatter, *Atmospheric research*, 50, 265–288, 1999.
- Zaveri, R. A.: A new lumped structure photochemical mechanism for large-scale applications, *Journal of Geophysical Research: Atmospheres*, 104, 30 387–30 415, <https://doi.org/https://doi.org/10.1029/1999JD900876>, 1999.
- Zaveri, R. A. and Peters, L. K.: A new lumped structure photochemical mechanism for large-scale applications, *Journal of Geophysical Research: Atmospheres*, 104, 30 387–30 415, 1999.
- Zaveri, R. A., Easter, R. C., and Peters, L. K.: A computationally efficient Multicomponent Equilibrium Solver for Aerosols (MESA), *Journal of Geophysical Research: Atmospheres*, 110, 1–22, <https://doi.org/https://doi.org/10.1029/2004JD005618>, 2005a.
- Zaveri, R. A., Easter, R. C., and Peters, L. K.: A computationally efficient multicomponent equilibrium solver for aerosols (MESA), *Journal of Geophysical Research: Atmospheres*, 110, 2005b.
- Zaveri, R. A., Easter, R. C., and Wexler, A. S.: A new method for multicomponent activity coefficients of electrolytes in aqueous atmospheric aerosols, *Journal of Geophysical Research: Atmospheres*, 110, 1–23, <https://doi.org/https://doi.org/10.1029/2004JD004681>, 2005c.
- Zaveri, R. A., Easter, R. C., Fast, J. D., and Peters, L. K.: Model for simulating aerosol interactions and chemistry (MOSAIC), *Journal of Geophysical Research: Atmospheres*, 113, 1–29, <https://doi.org/https://doi.org/10.1029/2007JD008782>, 2008a.
- Zaveri, R. A., Easter, R. C., Fast, J. D., and Peters, L. K.: Model for simulating aerosol interactions and chemistry (MOSAIC), *Journal of Geophysical Research: Atmospheres*, 113, 2008b.
- Zaveri, R. A., Barnard, J. C., Easter, R. C., Riemer, N., and West, M.: Particle-resolved simulation of aerosol size, composition, mixing state, and the associated optical and cloud condensation nuclei activation properties in an evolving urban plume, *Journal of Geophysical Research: Atmospheres*, 115, 1–19, <https://doi.org/https://doi.org/10.1029/2009JD013616>, 2010.
- Zdanovskii, A.: New methods for calculating solubilities of electrolytes in multicomponent systems, *Zh. Fiz. Khim.*, 22, 1475–1485, 1948.
- Zhang, Q., Canagaratna, M. R., Jayne, J. T., Worsnop, D. R., and Jimenez, J.-L.: Time-and size-resolved chemical composition of submicron particles in Pittsburgh: Implications for aerosol sources and processes, *Journal of Geophysical Research: Atmospheres*, 110, 2005.

- Zhang, Q., Jimenez, J. L., Canagaratna, M., Allan, J. D., Coe, H., Ulbrich, I., Alfarra, M., Takami, A., Middlebrook, A., Sun, Y., et al.: Ubiquity and dominance of oxygenated species in organic aerosols in anthropogenically-influenced Northern Hemisphere midlatitudes, *Geophysical research letters*, 34, 2007.
- Zhang, R., Li, Y., Zhang, A. L., Wang, Y., and Molina, M. J.: Identifying airborne transmission as the dominant route for the spread of COVID-19, *Proceedings of the National Academy of Sciences*, 117, 14 857–14 863, 2020.
- Zheng, G., Su, H., Wang, S., Andreae, M. O., Pöschl, U., and Cheng, Y.: Multiphase buffer theory explains contrasts in atmospheric aerosol acidity, *Science*, 369, 1374–1377, 2020.
- Zheng, Z., Curtis, J. H., Yao, Y., Gasparik, J. T., Anantharaj, V. G., Zhao, L., West, M., and Riemer, N.: Estimating submicron aerosol mixing state at the global scale with machine learning and earth system modeling, *Earth and Space Science*, 8, [https://doi.org/https://doi.org/10.1029/2020ea001500](https://doi.org/10.1029/2020ea001500), 2021a.
- Zheng, Z., Curtis, J. H., Yao, Y., Gasparik, J. T., Anantharaj, V. G., Zhao, L., West, M., and Riemer, N.: Estimating submicron aerosol mixing state at the global scale with machine learning and Earth system modeling, *Earth and Space Science*, 8, e2020EA001 500, 2021b.
- Zhu, J., Penner, J. E., Lin, G., Zhou, C., Xu, L., and Zhuang, B.: Mechanism of SOA formation determines magnitude of radiative effects, *Proceedings of the National Academy of Sciences*, 114, 12 685–12 690, 2017.
- Zhuang, H., Chan, C. K., Fang, M., and Wexler, A. S.: Size distributions of particulate sulfate, nitrate, and ammonium at a coastal site in Hong Kong, *Atmospheric Environment*, 33, 843–853, 1999.
- Zieger, P., Fierz-Schmidhauser, R., Weingartner, E., and Baltensperger, U.: Effects of relative humidity on aerosol light scattering: Results from different European sites, *Atmospheric Chemistry and Physics*, 13, 10 609–10 631, <https://doi.org/10.5194/acp-13-10609-2013>, 2013.